

ANALYSIS AND DESIGN OF ELECTRODES
AND CIRCUITS FOR TRANSFER
IMPEDANCE MEASUREMENTS
IN BIOLOGICAL MEDIA

By
ALLEN HARRIS FLASTERSTEIN

A DISSERTATION PRESENTED TO THE GRADUATE COUNCIL OF
THE UNIVERSITY OF FLORIDA
IN PARTIAL FULFILLMENT OF THE REQUIREMENTS FOR THE
DEGREE OF DOCTOR OF PHILOSOPHY

UNIVERSITY OF FLORIDA
1968

Copyright by
Allen Harris Flasterstein
1968

To

Eric, Ian and Grandma Ess

ACKNOWLEDGEMENTS

The author wishes to express his appreciation to Doctor Jack R. Smith for sponsoring and directing his research activities; and to Doctor Arnold H. Nevis who has contributed much toward the author's development in the biological impedance field.

The author also wishes to acknowledge Doctors Melvin J. Fregly, Earnest B. Wright, Charles V. Shaffer and Theodore S. George who, as members of his supervisory committee, have offered helpful suggestions and have been especially patient in awaiting the conclusion of this work.

Finally, special appreciation is due William K. Converse, whose laboratory skills and other assistance have been of special value; and Barbara Rucker for doing such a fine job in typing the final manuscript.

This investigation was supported by Public Health Service Fellowship No. 4-F1-GM-25, 522-04, from the National Institute of General Medical Sciences.

TABLE OF CONTENTS

	PAGE
ACKNOWLEDGEMENTS	iv
LIST OF TABLES	viii
LIST OF FIGURES	x
ABSTRACT	xiii
 CHAPTER	
1 INTRODUCTION	
Problems and Contributions.	1
Network Classification.	2
Complex Impedance	3
Tissue Impedance.	6
Literature Review	14
Two-Electrode Measurements.	15
Three-Electrode Measurements.	20
Four-Electrode Measurements	22
Summary	36
2 MATRIX AND NETWORK DESCRIPTION OF FOUR-ELECTRODE SYSTEMS	
Voltage and Current Conventions	39
The Impedance Parameter Matrix.	40
Analysis of the m Parameters.	42
The Effective Interface Impedances.	45
The h Coefficients.	48
The Equivalent Network.	55
Examples of Impedance Parameter Matrices.	58
Concluding Remarks.	63
3 ERRORS IN THE IDENTIFICATION OF TRANSFER IMPEDANCE BY THE CLASSICAL METHOD	
Introduction.	64
Loading Error	65
Errors Due to Admittance Classes 1, 2, and 3.	68
Errors Due to Ground Admittance	84
Common Mode Rejection Error	87
Current Control Error	90
Noise in the Classical System	97
Instrumentation Noise	98

TABLE OF CONTENTS (Continued)

	PAGE
Environmental Noise	99
Electrode-Tissue Noise.	102
 4 THE VIRTUAL-GROUND CONFIGURATION	
Introduction.	105
Common Mode Rejection Error	108
Single-Ended Operation.	108
Differential Operation.	111
Loading Error	113
Cable and Amplifier Input Admittance.	113
Ground Admittance	118
Current Control Error	119
Stability Considerations.	121
Stabilization Techniques.	125
Noise in the Virtual-Ground System.	133
Instrumentation Noise	133
Environmental Noise	135
Electrode-Tissue Noise.	137
The Negative-Feedback Filter Loop	137
 5 AN EXPERIMENTAL SYSTEM BASED ON THE VIRTUAL-GROUND CONFIGURATION	
Introduction.	147
The Physical Layout	148
Connection to the Electrode-Tissue System	148
Ground Connection	152
Output Connection	152
Input Connection.	153
Circuit Details	153
The Response Amplifier.	153
The Virtual-Ground Amplifier.	155
The Feedback Filter	156
The Current Control Circuit	157
Experimental Studies.	161
Performance Tests	162
Four-Electrode Impedance Measurements	173
 RECOMMENDATIONS FOR FUTURE STUDY.	185
Electrode Systems	185
The Virtual-Ground System	185
Information Retrieval	186
Biological Studies.	186

APPENDICES

1	Reciprocity Relations of the Impedance Parameter Matrix.	188
---	---	-----

TABLE OF CONTENTS (Continued)

	PAGE
2 The Voltage Follower Amplifier.	190
3 The Voltage Inverter Amplifier.	192
4 Principles of the Lock-in Amplifier	193
REFERENCES	196

LIST OF TABLES

Table	Page
2.1 Definitions of the m Parameters.	41
2.2 Approximate Values of \bar{X} and ψ for Stainless Steel Electrodes in Isotonic Saline.	59
2.3 Matrix Elements for Example 1.	61
2.4 Matrix Elements for Example 2.	62
3.1 Sign of Magnitude and Phase Errors in \hat{m}_{11}	74
3.2 Limits of Class 1, 2, and 3 Conductance for the Examples of Chapter 2.	78
3.3 Limits of Class 1, 2, and 3 Susceptance and Capacitance for the Examples of Chapter 2.	82
3.4 Limits of Ground Admittance for the Examples of Chapter 2. .	86
3.5 Minimum Values of Common Mode Rejection Ratio for the Examples of Chapter 2.	90
3.6 Minimum Values of Current Source Resistance for the Examples of Chapter 2.	95
4.1 Values of β_v for the Examples of Chapter 2	116
4.2 Limits of Cable and Amplifier Input Admittance for the Examples of Chapter 2.	117
4.3 Limits of Ground Admittance for the Examples of Chapter 2. .	119
4.4 Minimum Values of Current Source Resistance for the Examples of Chapter 2.	121
4.5 Limits of ξ for Given Values of ϕ_p	131
5.1 Frequency Response Errors.	166
5.2 Common Mode Rejection Errors	169
5.3 Current Control Test Results	172

Table	Page
5.4 Test Results of an Electrode Assembly in Isotonic Saline . .	177
5.5 Specific Impedance of Rat Cerebral Cortex.	182

LIST OF FIGURES

Figure	Page
1.1 Frequency Dispersion in Tissues	8
1.2 Four-Electrode Bridge	23
1.3 Voltage Clamp Scheme.	27
1.4 Four-Electrode Comparison Scheme.	30
2.1 Voltage and Current Conventions for the Electrode-Tissue System.	39
2.2 Electrode-Tissue Interface in an Arbitrary Current Field. .	43
2.3 Parallel Wire Four-Electrode System	46
2.4 Electrode-Tissue System Showing the Effective Interface Impedances.	48
2.5 Electrode Current Density in the System of Figure 2.3 . . .	51
2.6 Frequency Dispersion of the Geometrical Factor for the System of Figure 2.3.	52
2.7 Equivalent Network for the Hypothetical System.	55
2.8 Complete Equivalent Network of the Electrode-Tissue System.	58
2.9 Four-Electrode System with Hemispherical Electrodes	60
3.1 Basic Block Diagram for Impedance Measurements.	65
3.2 Schematic Diagram of the Electrode-Tissue and Loading Admittance Systems.	67
3.3 Equivalent Network for Loading Admittance Classes 1, 2, and 3	69
3.4 Phasor Relations of α_L in the Complex Plane	74
3.5 Input Circuit of a Differential Amplifier	83

LIST OF FIGURES (Continued)

Figure	Page
3.6 Approximation of a Current Source	91
3.7 Phasor Relations of α_Q in the Complex Plane	94
3.8 Noise Sources in the Classical Method	98
4.1 Basic Connections of the Virtual-Ground Configuration . . .	106
4.2 Nominal Gain and Phase Shift Characteristics of Operational Amplifiers.	107
4.3 Virtual-Ground System Showing Loading Admittances and Noise Sources	109
4.4 Simplified Equivalent Circuit for the Virtual-Ground Amplifier Feedback Loop	124
4.5 Stabilization Techniques for the Virtual-Ground Amplifier Feedback Network.	126
4.6 Typical Magnitude and Phase Characteristics of a Lag Network	129
4.7 Electrode-Tissue System with Stabilizing Resistors.	133
4.8 Virtual-Ground System with Negative-Feedback Filter Loop. .	138
4.9 Simple Low-Pass Filter.	142
4.10 Simple High-Pass Filter	143
4.11 Overall Transfer Function Characteristics Using Several Methods of Noise Filtering.	145
5.1 Close-up Photograph of the Experimental Virtual-Ground System.	149
5.2 Complete View of the Experimental Arrangement	150
5.3 The Response Amplifier Circuit.	154
5.4 Principles of Current Control	158
5.5 The Current Control Circuit	159
5.6 Block Diagram for Experimental Studies.	163

LIST OF FIGURES (Continued)

Figure		Page
5.7	Attenuator Circuit for Frequency Response Test.	165
5.8	Circuit for Common Mode Rejection Test.	167
5.9	Circuit for Current Control Test.	171
5.10	Electrode Assembly for <u>In Situ</u> Impedance Measurements . . .	175
5.11	Impedance of Rat Cerebral Cortex <u>In Situ</u>	179
5.12	Polar Plot of the Impedance of Rat Cortex	183
A1	Voltage and Current Conventions for Reciprocity Relations .	188
A2	Voltage Follower Amplifier.	190
A3	Voltage Inverter Amplifier.	192
A4	Block Diagram of the Lock-in Amplifier.	194

Abstract of Dissertation Presented to the Graduate Council
in Partial Fulfillment of the Requirements for the
Degree of Doctor of Philosophy

ANALYSIS AND DESIGN OF ELECTRODES AND CIRCUITS FOR
TRANSFER IMPEDANCE MEASUREMENTS IN BIOLOGICAL MEDIA

By

Allen Harris Flasterstein

August, 1968

Chairman: Dr. J. R. Smith
Co-chairman: Dr. T. S. George
Major Department: Electrical Engineering

Attempts by many investigators to measure the electrical impedance properties of animal tissues in situ at frequencies of physiological interest (0 to 200 kHz) have met with only moderate success. The effects of electrode polarization have been reduced or eliminated by using separate voltage pickup and current electrode pairs. However, the practical limitations of this method have not been clearly defined, nor have appropriate analytical techniques been applied to the analysis and design of the electrode and instrumentation systems. These deficiencies and the inadequacy of existing instrumentation techniques have hindered progress in the impedance art.

In the dissertation abstracted here, the ensemble consisting of four electrodes in an electrolytic medium (or biological tissue) is depicted as a linear four terminal device and described by means of a 3×3 matrix of complex impedance parameters. The matrix elements are dissected into electrolyte and interface components which are defined in terms of the field geometry, and the impedance characteristics of the electrolyte and the electrode-electrolyte interfaces.

Although the matrix description is more direct and often simpler to use, an equivalent network has also been evolved. The matrix elements of two different electrode configurations are calculated and used to illustrate major analytical results.

The immediate objective of most four-electrode impedance measurements is to identify what has been defined as the first element in the impedance parameter matrix. This element is estimated experimentally by determining the ratio of an arbitrary measure of the nominal voltage response to an arbitrary measure of the nominal exciting current under the assumption that the current in the voltage-response electrodes is zero. The parameters defined in the impedance matrix permit a comprehensive analysis to be made of the errors involved in this determination. On the basis of such an analysis, the classical method of grounding one current electrode and recording differentially from the potential electrodes has been found to be impractical for small electrode systems at low and high frequencies.

To overcome many of the limitations of the classical method, a new technique, called the virtual-ground system, has been developed. In this system, one potential electrode is maintained close to ground potential by means of negative feedback. Three classes of error--loading, common mode rejection, and current control--are analyzed for the classical and virtual-ground systems. In addition, several types of noise and methods of noise filtering are considered in each system. The results of the error and noise analyses demonstrate the advantages of the virtual-ground system and provide a set of design formulae. To complement the virtual-ground system, a current control circuit has

been adopted from the literature and analyzed for application to broad band impedance measurements.

A successfully operating system using the virtual-ground system and the adopted current control circuit has been built at modest cost and is described in the dissertation. It has been tested with small electrode assemblies in saline and with similar assemblies implanted in the cerebral cortex of live rats. Several experiments are reported to verify system performance and indicate the quality of results already obtained.

CHAPTER 1

INTRODUCTION

Problems and Contributions

Attempts by many investigators to measure the electrical impedance properties of animal tissues in situ at frequencies of physiological interest (0 to 200 kHz) have met with only moderate success. The effects of electrode polarization have been reduced or eliminated by using separate voltage pickup and current electrode pairs. However, the practical limitations of this method have not been clearly defined, nor have appropriate analytical techniques been applied to the analysis and design of the electrode and instrumentation systems. These deficiencies and the inadequacy of existing instrumentation techniques have hindered progress in the impedance art.

In the present chapter, definitions and assumptions are explained which are basic to the study of biological impedance phenomena; the nature of tissue impedance is reviewed according to current knowledge; and a review of selected literature is presented, which reveals various measurement techniques and common sources of error. The material in Chapters 2, 3, 4 and 5 represents an original application of engineering principles toward the general fulfillment of the needs expressed in the opening paragraph. In Chapter 2,

special parameters are defined which lead to an unprecedented understanding of the electrode-tissue system and provide an appropriate basis for the analysis and design discussions that follow. In Chapter 3, the classical method for transfer impedance measurements is thoroughly investigated, resulting in useful design criteria and sophistication in understanding the major types of measurement error. In Chapter 4, a new instrumentation technique is proposed and analyzed in depth. The new technique is shown to offer major advantages over existing methods. An experimental system which incorporates this technique and several other special advances is described in Chapter 5 along with pertinent experimental results.

Network Classification

To make impedance measurements more intelligible at the present state of the art, one usually invokes the restrictions of time invariance and linearity on the medium of interest.

Time invariance implies that the impedance properties of the medium do not vary during the critical period of measurement. The critical period may just include one to several repetitions of the applied signal waveform or, for example, it may include a whole sequence of separate measurements at different sinusoidal frequencies. Time invariance does not exclude the measurement of impedance changes provided that the changes are slow compared to the time required for a single measurement. Certain impedance characteristics of tissues in situ are known to vary spontaneously and under various stimuli in periods ranging from many hours to several seconds.

A system is linear if the response to a forcing function comprised of several components is equal to the sum of the responses which would be obtained from each component acting alone (Dern and Walsh, 1963). Further, if the amplitude of a given forcing function is doubled, then the amplitude of the response function should also double while the waveform remains the same. This restriction appears to be satisfied in practice if the charge and current density in the tissue are kept sufficiently low. Hence, currents and voltages are typically measured in microamperes and microvolts. At these levels, several different sources of noise may be significant. This topic is considered later in the work.

When the linearity condition is satisfied, it is almost certain that the medium will also be bilateral and passive. A system is bilateral if the negative of the response to a given forcing function is the response to the negative of that forcing function. Most tissues are not strictly passive in the network sense (Raisbeck, 1954) because they contain electrochemical sources of energy. In the linear range, however, the electrical activity of these sources appears to be independent of the applied signal. Since measurement techniques attempt to weed out the effects of background noise, the final results ideally correspond to those of a passive medium.

Complex Impedance

If a sinusoidal forcing function is applied to a time invariant linear bilateral network, every waveform in the network will also be sinusoidal with the same frequency once the initial transients die

out, i.e., when the steady state is reached. Only the phase and amplitude may differ from place to place. This convenient property leads to the definition of complex impedance,

$$Z \equiv \frac{|V|}{|I|} e^{j\theta} \quad (1.1)$$

where $|V|$ and $|I|$ are the peak amplitudes of an arbitrary steady state voltage-current pair and θ is the algebraic phase difference between them, measured with respect to the voltage waveform.

The factor $e^{j\theta}$ is known as the polar form of the complex number given by

$$e^{j\theta} = \cos \theta + j \sin \theta \quad (1.2)$$

where e is the natural logarithm base and j is the imaginary operator $\sqrt{-1}$. The cosine and sine terms are known as the real and imaginary parts of the complex number, respectively.

If V and I occur at the same terminal pair, Z is called a driving point impedance. When they occur at different terminal pairs, Z is known as a transfer impedance. In either case, it is an inherent physical parameter of the network. Sometimes, it is more convenient to use the reciprocal of the complex impedance called the complex admittance. For the same quantities as before, the complex admittance is defined as

$$Y \equiv \frac{|I|}{|V|} e^{-j\theta} \quad (1.3)$$

The concepts of complex impedance and complex admittance will be used frequently in the present work. In addition, all voltage and current signals in the electrode-tissue system will be written in complex form. The complex form of the signal

$$v(t) = |V| \cos(\omega t + \theta) \quad (1.4)$$

is defined as

$$v \equiv |V| e^{j\theta} \quad (1.5)$$

Explanations of the use of complex notation may be found in basic texts in electrical engineering (e.g., Van Valkenburg, 1955).

The theory of linear time invariant systems shows that if the sinusoidal steady state response of a system is known at a sufficient number of frequencies, the response to other waveforms, periodic or transient, can be determined analytically and vice versa. This equivalency is especially welcomed when spectral information is desired and the time for measurements is limited. Although useful results have been obtained from nonsinusoidal methods (Smith, 1967), much of the available information is lost due to inadequate resolution and bandwidth in the measuring system. Improved data processing techniques using digital computation are certain to overcome some of the difficulty. The remaining problem lies in the extraction and amplification of the raw analog data which is a major theme in the present work.

Tissue Impedance

Animal tissues fall into four major classifications: epithelial, connective, muscular and nervous (Ham, 1965); and each of these may be further divided into a number of specific subclasses. The constitution and structure of tissues, even within the same classification, may vary markedly. Furthermore, the electrical properties of relatively few tissue types, such as muscular and nervous, have been studied in detail. The following discussion presents a brief synopsis of the highlights of tissue impedance studies. It pertains most directly to muscular and nervous tissues but is also applicable, with some modifications, to other tissues.

In tissue, the applied current may travel between cells in the extracellular fluid and across cell membranes into the intracellular fluid and subcellular structures. At frequencies of the order of 200 kHz and below, the electrical properties of the fluids are, for all practical purposes, independent of frequency and are characterized by resistivity values of 100 to 200 ohm-cm (Schwan, 1963). However, membranes (cellular and subcellular) which are less than 200 Angstroms thick are associated with relatively high transverse resistance (1 to 1000 ohm-cm²) and high transverse capacitance (~ 1 uf/cm²).

The charging and discharging of adjacent membrane-fluid interfaces (similar to plates of a fixed capacitor) is one of several mechanisms which impart frequency dependent characteristics to the overall tissue impedance. The characteristics due to this specific mechanism in tissue have been termed β dispersion by Schwan (Schwan, 1957, 1959, 1963; Schwan and Cole, 1960). The membranous nature of tissue is also

responsible, in less evident ways, for other dispersion phenomena at lower frequencies than the β dispersion. These phenomena have been termed α dispersion (in tissues) by Schwan and have been associated with several different mechanisms which are still under debate. Further discussions of α and β dispersion are given in later paragraphs.

In addition to microscopic heterogeneities measured in Angstroms and microns, tissue properties may vary grossly in distances ranging from one to many millimeters. Many tissues are also anisotropic (Rush et al, 1963; Nicholson, 1965; Ranck and Be Ment, 1965). These characteristics and the close boundaries of some tissues in situ may be expected to influence the impedance determined with different electrode configurations in complex ways. Hence, the concept of specific impedance, defined for a one-centimeter cube of tissue in a uniform field, is an idealization which requires special qualification in each case. To be sure, data obtained with different electrode configurations in the same tissue may not simply differ by a constant geometrical factor and a comparison of results is at best approximate. In practice, one tries to use an electrode system which measures average properties of a large population of cells, but avoids the effects of gross inhomogeneities. There are, however, applications in which careful localization is not an important factor.

For an arbitrary electrode system, let the measured complex impedance be written

$$Z = R(f) + jX(f) \quad (1.6)$$

where R and X designate resistance and reactance, respectively, and both are functions of frequency. It has been reasonably well established that two fairly distinct frequency dispersions occur in many, if not all, tissues in the 0 to 200 kHz frequency band (Schwan, 1957; Fatt, 1963; Ranck, 1963a). Using Schwan's terminology, the α and β dispersions are characterized approximately by circular arcs in the complex impedance plane as indicated in Figure 1.1. The arcs usually overlap

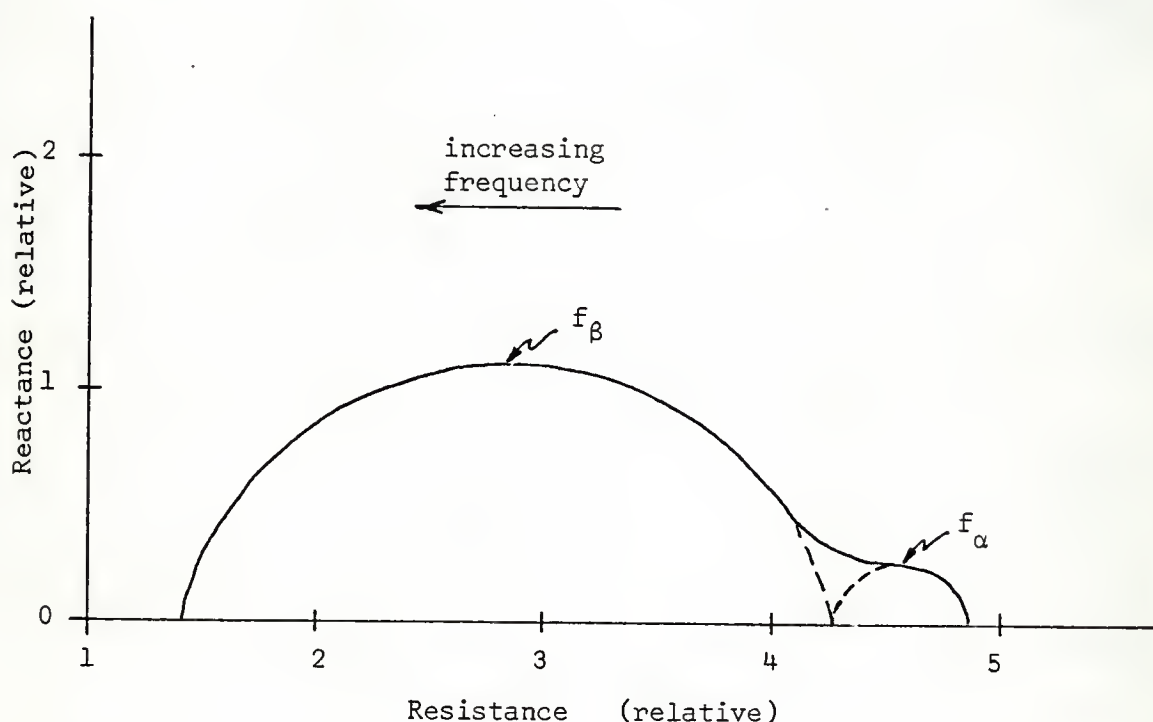


Figure 1.1. Frequency Dispersion in Tissues

and have centers below the R axis. In results so far reported, the overlap region generally occurs at frequencies below 2 kHz. The low frequency for maximum reactance, f_α , may vary from several hundred Hz to below 20 Hz depending on tissue and experimental conditions.

Likewise, the high frequency for maximum reactance, f_{β} , may vary from roughly 1 kHz to well above 200 kHz.

Scales have been provided in Figure 1.1 to illustrate relative features of the dispersion phenomena. It is evident that a high degree of measurement accuracy is required to resolve points on the α dispersion arc. On this arc, the reactance is usually less than one fifth as large as the resistance with corresponding phase angles of less than 12 degrees. In addition, the resistance usually changes by less than 20 percent over the arc. The accuracy required to measure α dispersion is difficult to achieve in vitro, but it is especially difficult to achieve in situ.

In vitro, the α and β dispersions are both sensitive to age and environmental factors. The α dispersion appears to be more closely related to in vivo properties of the tissue and breaks down rapidly after excision. The β dispersion may not change significantly for many hours after excision. It disappears only after cellular structure completely deteriorates. A detailed discussion of α and β dispersion is beyond the scope of the present work. However, a brief introduction to the mechanisms which underlie these phenomena is of interest and is given in the following sections.

β dispersion

The explanation of β dispersion follows from principles of classical electric field theory first presented by Maxwell in 1873. The theory has been applied to suspensions of conducting spherical, ellipsoidal and cylindrical particles surrounded by poorly conducting

shells (membranes) to simulate various biological materials. In brief, β dispersion is a structural phenomenon depending on the distribution of the membranes and conducting fluids, the resistivity of the fluids, and the dielectric properties of the membrane material.

At frequencies just above the β arc, the membrane impedance is negligible in comparison to the effective resistance of the cell interior, and the tissue behaves like a suspension of conducting bodies in a similar conducting medium. As the β arc is entered, the membrane impedance grows comparable to the effective resistance of the cell interior. Toward the low frequency end of the arc, the membrane impedance has grown much larger than the effective resistance of the cell interior and the tissue begins to approach (but does not necessarily attain) a condition in which the cells appear like empty holes in the extracellular fluid.

While β dispersion is primarily associated with the cell membrane proper, the membraneous structures within the cell may also contribute to the dispersion phenomena by a similar mechanism. However, these effects are smaller and tend to occur at higher frequencies (1 MHz to 10 MHz). Dispersions due to proteins and other macromolecular matter in the fluids also occur in the MHz range, but these mechanisms are distinctly different from that of the β dispersion.

α dispersion

The additional resistance rise associated with α dispersion originates from one or more mechanisms which cannot follow the rapid electrical changes that occur at frequencies above the α dispersion

range. Hence, this dispersion, as β dispersion, is characterized by capacitive properties (negative reactance). But, contrary to β dispersion, the underlying phenomenon does not necessarily involve the charge and discharge of adjacent faces of a dielectric material. At least five different mechanisms have been proposed to explain α dispersion (Schwan, 1957; Schwan and Cole, 1960; Fatt, 1963; Ranck, 1963b). These are summarized in the following paragraphs.

Membrane permeability.--The term permeability refers to the physical transport of ions through the cell membrane and is envisioned to occur at specific sites in the membrane. If the net ion current is regulated by the cell such that it is related to the membrane voltage through a differential equation in time, then the permeability is electrically equivalent to an impedance characterized by resistive and capacitive elements, even though no physical capacitance exists. Inductive elements are also possible. Evidence for the permeability mechanism is based mainly on studies of large nerve axons (Cole, 1955; Schmitt, 1955).

Membrane structure.--The membrane is envisioned as a double layered structure of electrically different materials (lipid and protein). This structure results in a frequency dispersion of the total membrane impedance, which is characterized by a bounded increase in the effective parallel resistance and capacitance of the membrane as the frequency is decreased. Schwan (1957) has predicted that this dispersion should occur in the frequency range of 10 Hz to 1 kHz, which is in agreement with the typical range for α dispersion.

Intracellular channels.--Fatt (1963) has developed a theory of dispersion based on the structural organization of the muscle fibre. He considers two parallel current paths. One is formed by the bulk impedance of the cell membrane in series with the bulk intracellular fluid and is primarily responsible for β dispersion. The other path originates at specific sites (pores) in the cell membrane and continues through a system of intracellular channels (the sarcotubular system of the endoplasmic reticulum). It is primarily responsible for α dispersion. For convenience, let the parallel paths be designated by α and β corresponding to their respective dispersion phenomena.

Each path is represented by a resistor in series with a capacitor. Since the channels making up the α path collectively occupy a minute cross section of the membrane surface and cell interior, the effective resistance of the α path is much higher (order of 100 times) than that of the β path. On the other hand, a special mechanism is postulated for the channel entrance which permits the effective capacitance of the α path to be much larger (order of 25 times) than that of the β path. Hence, at high frequencies, the α path appears as a high resistance across the β path and has little effect on the β dispersion. At low frequencies, the β path appears as a large reactance across the α path and has little effect on the α dispersion. The α dispersion is much smaller than the β dispersion because the effective impedance of the extracellular fluid that shunts the cell remains constant, while the α path phenomenon occurs at a much higher impedance level than that of the β path.

With a constant resistor and capacitor representing the two

paths, the α and β arcs are centered on the real axis, corresponding to one time constant each. In practice, the arcs are centered below the axis, corresponding to a distribution of time constants. To account for this fact, Fatt postulates and investigates the existence of distributed electrical coupling between the channel system and the bulk intracellular fluid.

Cable properties.--Ranck (1963b) has developed a theory of α dispersion based on the cable-like properties of cell processes in cortical tissue. He postulates that at low frequencies (below 5 kHz), the signal current is constrained by the cell membranes to flow primarily along the cell processes (axons and dendrites). The tissue then appears as a system of cables consisting of intracellular and extracellular fluid conductors separated by a leaky dielectric material (the cell membrane). Using the cable equation and certain assumptions to account for geometrical and material aspects of the tissue, Ranck shows, in quantitative terms, that the cable mechanism may well give rise to the experimentally observed α dispersion (Ranck, 1963a).

At higher frequencies (above 5 kHz), the membrane impedance has dropped sufficiently so that the signal current is no longer constrained to paths along the cell processes. The current then flows primarily in directions transverse to the cell membranes. The mechanism for β dispersion occurs according to the principles of Maxwell as previously discussed.

Relaxation of ionic atmospheres.--This mechanism, suggested by Schwan, is based on impedance studies of suspensions of small non-conducting particles (polystyrene, glass, kaolin, etc.) in electrolytic

media. These suspensions give rise to low and high frequency dispersion phenomena which are similar to the α and β dispersion of tissue. At low frequencies, the particles are perfectly insulating. Hence, the low frequency dispersion can only arise through a variation in the effective impedance of the current paths between the particles. The mechanism lies in the displacement from equilibrium position of the ionic layers which are known to collect around particles in electrolyte suspension. The displacement is accompanied by a change in the stored electrostatic energy of the layers and a perturbation of the field around the particle. These phenomena are frequency dependent and are reflected as reactive and resistive components in the suspension impedance.

Many biologically significant phenomena have been reported to influence the impedance properties of certain tissues in vivo. In view of these findings and the possible mechanisms that underlie impedance phenomena, the measurement and analysis of tissue impedance have become an important research tool (e.g., Adey et al, 1962; Aladjalova, 1964; Cole, 1962; Geddes and Baker, 1967; Nevis and Collins, 1967; Shalit and Mahler, 1966; Van Harreveld, 1966). Impedance measurements are also of potential interest in clinical applications. Unfortunately, inadequacies and uncertainties in experimental technique have hindered their development for widespread use. Some of the problems are resolved in the present work.

Literature Review

Three principal classes of electrode systems have evolved to

meet the varied demands of biological impedance studies. In each case, two or more electrodes (the current electrodes) are required to supply signal current to the tissue under study. The classes are distinguished according to the method of observing the voltage signal. Thus, in two-electrode systems, the voltage is observed directly at the current electrodes; in three-electrode systems, the voltage is observed between a potential electrode and one of the current electrodes; in four-electrode systems, the voltage is observed between two potential electrodes.

The major reason for using three-electrode and four-electrode systems is that the potential electrodes nominally do not draw current so that the observed voltage response is not influenced by interface impedance. Higher order systems also permit greater freedom in selecting the current field configuration, which sometimes leads to more versatile experiments and better anatomical localization of observed impedance phenomena. Furthermore, they facilitate control of the signal current level and are especially convenient for monitoring ongoing biological activity during the impedance measurement.

To provide further insight into the nature and limitations of biological impedance measurements, some of the major works in this field are reviewed in the following sections. An effort is made to indicate historical background and reveal common relationships between the three classes of electrode systems.

Two-Electrode Measurements

Early studies of the conductivity of biological materials may

be traced as far back as the nineteenth century. However, the earliest major work to influence modern tissue impedance research was that of Fricke and Morse (1925), who first applied field theory to the interpretation of experimental impedance data. Thus, from measurements of suspensions of red blood cells, the authors were able to estimate the resistive and capacitive properties of the cell membranes. The suspensions were contained in an electrolytic cell and measured by means of a wheatstone bridge. The electrolytic cell was shaped like an hourglass with large platinized platinum electrodes sealed into either end. Although this design was selected to minimize electrode polarization effects, the authors were well aware that the low frequency utility of the cell was still quite limited. The wheatstone bridge was operable from 800 Hz to 4.5 MHz, but no results were reported for frequencies below 3600 Hz.

A large body of impedance work has been done on excised tissues as well as cell suspensions, using methods similar to that of Fricke and Morse. Various improvements have appeared with respect to the bridge system (Cole and Curtis, 1937; Schwan and Sittel, 1953). In addition, a number of techniques have evolved for extending the low frequency capability of the electrolytic cell (Schwan, 1963). The three principal methods are summarized below.

Distance variation method.--In the distance variation method (Fricke and Curtis, 1937), measurements are made at two different electrode separations. By subtracting the smaller from the larger result, polarization effects are eliminated and the impedance of the difference volume is obtained.

Substitution method.--In the substitution method (Cole and Curtis, 1937), the sample with unknown impedance properties is replaced by a sample with known impedance properties. The electrode polarization impedance is then calculated from measurements on the known sample and subtracted from measurements on the unknown sample to give the desired impedance. Unfortunately, the method is not completely straightforward because polarization impedance is influenced by the presence of cells in the sample (Schwan, 1963). One way to avoid this discrepancy is to connect the electrodes indirectly to the sample through a fixed intermediate electrolyte (Schwan, 1954; and Fatt, 1963).

Frequency variation method.--Theoretical (e.g., Fricke, 1932) and experimental (e.g., Smith, et al., 1967) studies have shown that electrode polarization impedance may be approximated as a negative power function of frequency with a constant phase angle, i.e., $Z = Mf^{-\alpha}e^{-j\theta}$, where M , α , and θ are real positive constants and $\alpha < 1$, $\theta < 90$ degrees. Several schemes based on this fact have been given to distinguish between electrode polarization and tissue impedance (Schwan, 1963; Smith, et al., 1967). In essence, the polarization impedance is first measured at low frequencies where the sample impedance is negligible. These data are used to estimate the polarization impedance at higher frequencies so that it may be discounted from the sample measurements.

In all of the techniques for eliminating the effects of electrode polarization, the sample impedance is estimated as the difference between two quantities which are assumed to share a common polarization impedance. As the frequency is decreased, the common polarization impedance increases with respect to the sample impedance. Hence, a

small relative error in the quantities to be differenced leads to an increasingly larger error in the result. In practice, a satisfactory degree of accuracy can only be achieved at frequencies where the common impedance is less than the impedance to be estimated.

In 1950, the status of in situ impedance measurements was reviewed (Benjamin, et al., 1950) and many of the technical difficulties involved in such measurements were discussed. The authors concluded that reliable in situ data were not yet available at physiological frequencies and called for greater effort in that direction. For obvious reasons, methods of correcting for electrode polarization are more difficult to implement in situ than in vitro. Few, if any, two-electrode studies in situ are beyond serious criticism.

The earliest of the more precise in situ studies was reported by Schwan and Kay (1956, 1957). They measured resistive and capacitive properties of various thoracic tissues in anesthetized dogs. The electrode system consisted of a cylindrical probe with one electrode forming the tip and one electrode forming part of the shank. The electrode material was platinized platinum and the surface area of each electrode was 0.3 cm^2 . Measurements were performed with a wheatstone bridge at frequencies from 10 Hz to 10 kHz.

To correct for electrode polarization, the polarization impedance was measured as a function of frequency in isotonic saline. These results were modified by a masking factor to estimate the polarization impedance in the tissue at each frequency. The masking factor was assumed to be independent of frequency and was determined by comparing the in-saline and in-tissue polarization impedances at 10 Hz. Special

precautions were necessary to assure that the fragile electrode surfaces were not altered between saline and tissue measurements. The accuracy of the series polarization resistance and capacitance calculated for in-tissue conditions was stated as about ± 10 percent. The error in the result for tissue capacitance was given as ± 10 percent at 100 Hz and ± 100 percent at 10 Hz. In other words, the reactive part of the polarization impedance was equal to that of the tissue at 100 Hz and was ten times that of the tissue at 10 Hz. For the tissue resistance, the error was given as ± 3 percent at 10 Hz. The higher accuracy reflects the fact that at 10 Hz the tissue resistance is much larger (more than 30 times) than the tissue reactance.

Schwan and Kay reported that the resistance of certain tissues rises about 20 percent beginning at a frequency below 1 kHz and continuing more sharply toward lower frequencies. This finding and certain of the values found for tissue resistance have since been disputed by others (Burger and van Dongen, 1960-61; Rush, et al, 1963), who, on the basis of four-electrode measurements, claimed the resistivity to be independent of frequency in this range. Several reasons were proposed by Rush et al. for the discrepancy. Important among these were erroneous assumptions in the correction for polarization impedance. Further evidence (Schwan, 1963, Figure 10; Smith et al., 1967) indicates that contrary to what was assumed, the masking factor may well have been dependent on frequency, especially below 500 Hz. If this is true, then the anomalous change in slope of the capacitance curve (Schwan and Kay, 1957, Figure 1) at frequencies below 500 Hz is also in question. It has been reasonably well established that a small variation in resistivity

does occur in many tissues at low frequencies (α dispersion). Therefore, in view of the many uncertain factors, it is suspected that none of the conflicting reports are completely reliable.

The work of Schwan and Kay illustrates some of the problems and uncertainties encountered in two-electrode measurements in situ. It probably also demonstrates the best accuracy that can be achieved under such conditions--at least in the light of current knowledge. Many experiments (especially chronic ones) require smaller electrodes and the error due to polarization is correspondingly larger. In any case, manual and computational correction procedures are time consuming and difficult to carry out with the degree of caution necessary. Furthermore, the validity of the key assumptions on which the accuracy of two-electrode results depend *is* difficult, if not impossible, to verify in specific experiments.

Three-Electrode Measurements

Three-electrode systems are useful where there is extreme asymmetry in the current electrode configuration. They have been used primarily to study the membrane properties of individual cells in situ and in vitro. The current is applied between a microelectrode (0.5 to 5 micron tip) in the cell body and a large reference electrode in the external medium. It passes across the membrane of the cell body and in the case of neurons, also through the dendritic branches (Rall, 1959). Almost all of the potential difference between the interior of the cell body and the reference electrode occurs across the cell membrane.

The reference electrode can usually be designed to produce a

negligible polarization component in the observed voltage. However, the impedance of the microelectrode is quite large (megohms) and cannot be neglected. To overcome this problem, a second microelectrode may be added in the cell body to record potential (Fessard and Tauc, 1956; Combs et. al., 1955, 1959). The high impedance of the intracellular electrodes makes such systems especially sensitive to parasitic coupling between electrodes. Fessard and Tauc used completely separate micropipettes to minimize this hazard. For smaller cells, the double-barrelled micropipette of Combs et. al. is more convenient, but the problem of parasitic coupling is intensified.

The foregoing methods have been used only with pulse waveforms to determine membrane time constants and for stimulating and observing active responses of neurons. A systematic application of sinusoidal techniques would be desirable both from the standpoint of defining measurement errors and obtaining more precise information about the electrical properties of the cell membrane.

Three-electrode systems have also been used with a distance variation technique to study tissue impedance in anesthetized animals. (Van Harreveld, et. al., 1963; Nicholson, 1965). The current field is set up by means of a fixed pair of current electrodes and the voltage is measured with respect to one current electrode as a function of potential electrode position. Regardless of the particular procedure and field configuration used, the calculation of specific impedance requires the evaluation of the voltage difference between probe positions. Hence this method is subject to similar limitations with respect to the ratio of common to difference voltage as were discussed

earlier for two-electrode systems. Another limitation of this technique is that the measurements at each electrode position are made at different time intervals.

Four-Electrode Measurements

It is convenient to classify four-electrode measurements according to the manner in which the potential electrodes are used. In this section, a method is labeled continuous if the potential electrodes take part in the impedance measurement simultaneously and discontinuous if separate measurements are required at each electrode.

Discontinuous methods

The only method of current interest which deals separately with each potential electrode is a bridge balancing scheme. The basic technique was originally described by Shedlovsky (1930a, b) for measuring conductance in nonbiological electrolytes. Recently it was applied to biological media (Songster, 1967; Hill, unpublished) and modified to include capacitive components and a broader frequency range (5 Hz to 200 kHz). The main features are illustrated in Figure 1.2. The electrode-tissue system is represented by the simplified equivalent network, Z_a , Z_b , and Z_c (see Figure 2.8 for the complete equivalent network). The current electrode interface impedances are included in Z_a and Z_c . Z_b represents the tissue impedance to be determined. The bridge balances are achieved by means of Z_1 and Z_2 , and the detector may be switched from position 1 to position 2 as needed.

The measurement procedure begins with Z_2 set at zero and proceeds in two successive steps.

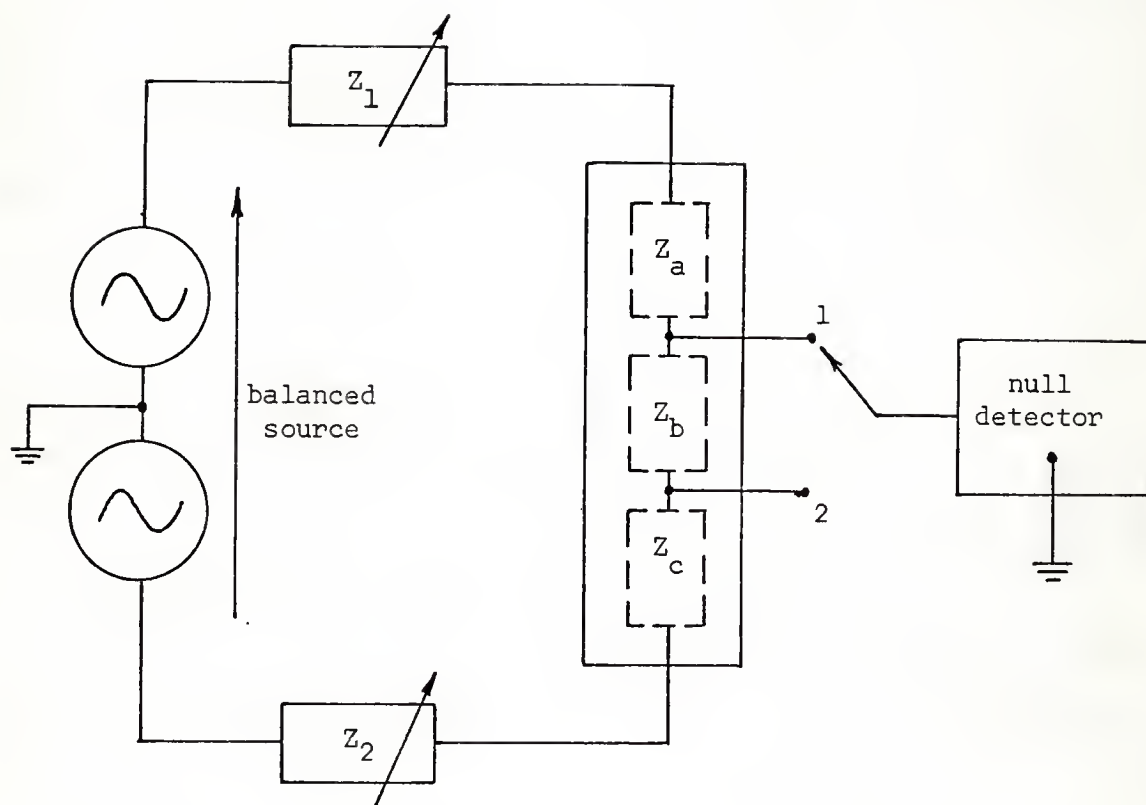


Figure 1.2. Four-Electrode Bridge

Step 1: Adjust Z_1 to null point 1.

Step 2: Adjust Z_2 to null point 2.

If t_1 and t_2 denote the times at which step 1 and step 2 are performed, then the balance conditions may be written

$$\text{at } t_1: \quad Z_1 \pm \epsilon_1 + Z_a(t_1) = Z_b(t_1) + Z_c(t_1)$$

$$\text{at } t_2: \quad Z_2 \pm \epsilon_2 + Z_c(t_2) = Z_b(t_2) + Z_a(t_2) + Z_1$$

where the ϵ are uncertainties in the adjustment of Z_1 and Z_2 . Note that each condition actually represents two equations, one for the resistive parts and one for the reactive parts of the impedances.

The balance equations may be added and the result arranged to give

$$Z_b(t_1) + Z_b(t_2) = Z_2 + (\Delta Z_c - \Delta Z_a) \pm (\epsilon_1 \pm \epsilon_2)$$

where ΔZ_c and ΔZ_a are the changes in Z_c and Z_a , if any, that occur from time t_1 to time t_2 . Ideally, ΔZ_c , ΔZ_a , ϵ_1 and ϵ_2 should be zero so that $Z_2/2$ is equal to Z_b (or its average value if it varies). In practice, these deviations are finite and must fall within limits much smaller than Z_b if the method is to be successful.

At least two factors are of major concern in evaluating the suitability of the bridge method for a particular biological study: bridge resolution and constancy of Z_a , Z_b and Z_c with time. At frequencies below 100 Hz (sometimes higher), Z_a and Z_c may be of the same order as or very much larger than Z_b , depending primarily on the electrode design. For example, with large platinized platinum electrodes in vitro, these impedances will usually be on the same order as or smaller than Z_b . They will also tend to remain constant in the $t_1 t_2$ interval. However, with small stainless steel electrodes, in situ, Z_a and Z_c may well be 1000 or more times as large as Z_b and are likely to vary during the measurement interval. The first example is easily within bridge capabilities, but the electrode system requires careful preparation. In the second case, very high bridge resolutions (greater than 1 part in 10^5) would be required to make the ϵ much smaller than Z_b .

Even then, the slightest variations in Z_a and Z_c with time could produce errors greater than 100 percent. The problem is compounded by the fact that as the frequency is decreased, it usually takes longer to achieve a bridge balance.

Clearly, there is a whole range of experiments with relative impedance values lying between the extremes discussed above. For many of these, the bridge method is not suitable on the basis of resolution and constancy arguments alone. On-line bridge methods are also limiting in that only one frequency at a time may be measured and each measurement takes several or more minutes to perform. Hence, impedance cannot be monitored continuously, nor can the instantaneous impedance spectrum be determined.

An advantage of the bridge method is that at balance, the potential electrode in use is approximately at ground potential. Hence, the input impedance of the null amplifier need not be especially large. This feature is shared with the method presented in Chapters 4 and 5 of the present work.

Continuous methods

The use of a four-electrode method in biological impedance measurements was first reported by Burger and van Milaan (1943). They measured various segments of the human body and used the results to estimate the specific resistance of certain body tissues. The current was supplied in manually switched d.c. pulses from a battery in series with a large fixed resistor. To find the transfer resistance of the electrode-tissue system, the voltage between potential electrodes was compared to the voltage across a known resistor connected in series

with the current electrodes. The voltages were amplified by means of a single-ended amplifier and read on a galvanometer. Since the current source and the electrode-tissue system were not independently grounded, the amplifier could be switched at will to the terminal pairs of interest.

Rush et. al. (1963) used a method similar to that of Burger and van Milaan to generate the current waveform. However, the voltage response was sensed by means of a differential amplifier. The amplifier common (ground) was connected to a remote point on the animal. The common mode signal of this configuration was of the same order of magnitude as the differential signal. Hence, the requirements on the input impedance and common mode rejection ratio of the amplifier were not difficult to satisfy.

For reasons of convenience, reliability and accuracy, it is usually desirable to use ground as a common reference for the current electrode and potential electrode circuits. This is especially true when sophisticated measurement techniques are employed and battery operation becomes impractical. The methods discussed in the remainder of this section use electronic current generators and common ground connections.

Among the earliest applications of four-electrode methods were the now famous voltage clamp experiments of Hodgkin, Huxley, and Cole. In the original experiments (Cole, 1949; Marmont, 1949), the membrane voltage was sensed with the same pair of electrodes that were used to provide the membrane current (a two-electrode method). Later, Hodgkin, Huxley, and Katz (1952) eliminated the error introduced by the current

electrode polarization voltages and some of the intervening medium by adding a second pair of electrodes to measure the membrane voltage (a four-electrode method).

The basic voltage clamp scheme has been carried out in various ways. One of the later arrangements used by Moore and Cole (1963) is depicted in simplified form in Figure 1.3. The potential amplifier

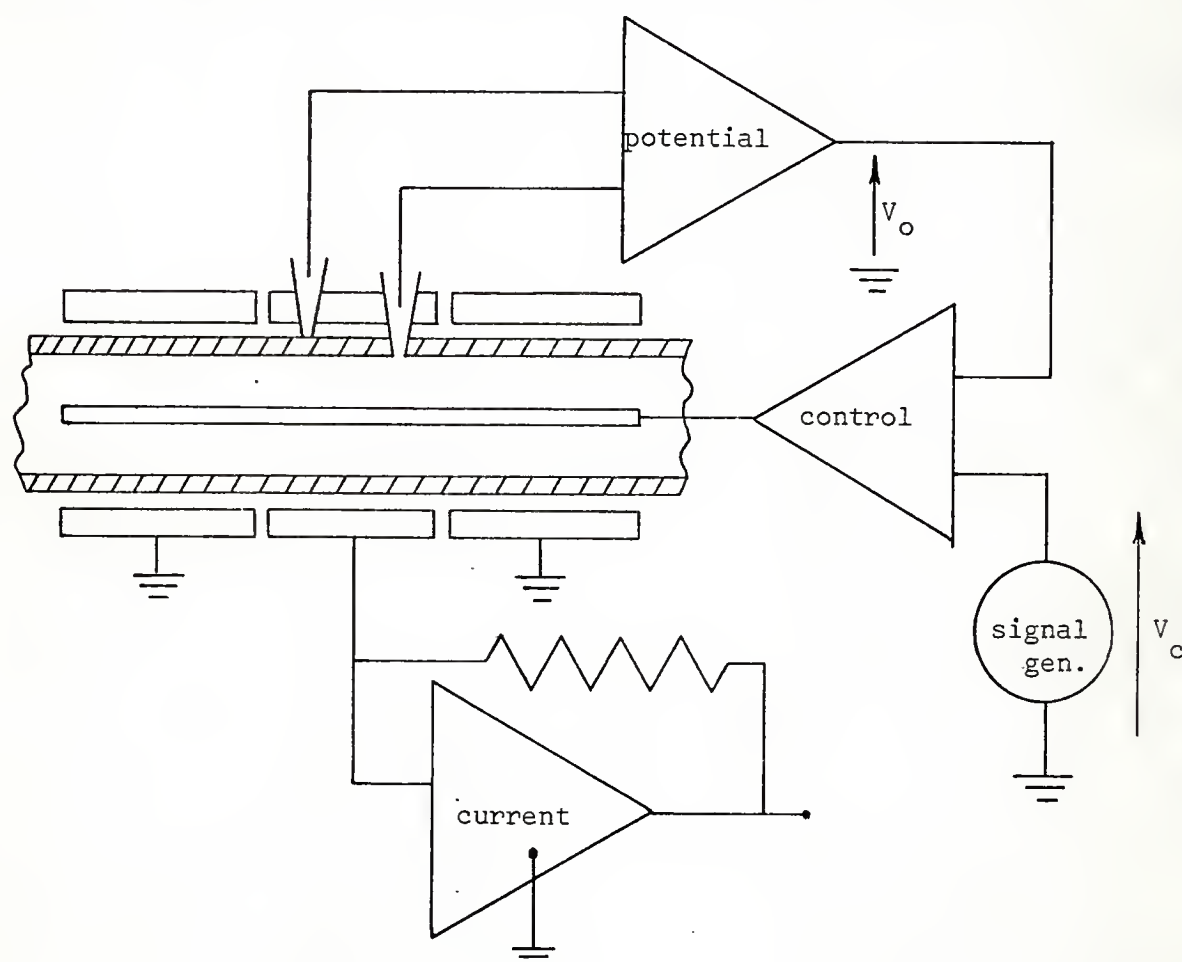


Figure 1.3. Voltage Clamp Scheme

senses the membrane voltage differentially by means of two micropipette electrodes. The output, V_o , is compared to the control signal, V_c , in the control amplifier which adjusts the current of the internal current electrode to maintain $V_o = V_c$. The external current electrode

consists of three separate cylindrical pieces. Current is measured only in the center piece where the field is uniform and calculable. The input of the current sensing circuit is essentially at ground potential. The external current electrodes in this system have a relatively large area and are usually platinized platinum (sometimes Ag-AgCl).

The common mode signal to the potential amplifier is the voltage occurring between the external potential electrode and ground. The differential signal is essentially the membrane voltage. The highest ratio of common mode to differential signal occurs at the peak of the membrane current. A typical ratio is 20 mv/60 mv or 1/3 (Moore and Cole, 1963, Figure 10). Hence, for a 1 percent common mode error, the rejection ratio of the potential amplifier need only be about 33, which is not difficult to achieve. The low common mode signal found here is in contrast to the relatively high ratios that occur in a large number of four-electrode applications, especially those concerned with in situ tissues. Higher common mode to differential ratios not only require higher common mode rejection ratios, but also higher input impedances in the amplifiers. These topics are discussed in detail along with other problems in chapters to follow.

In 1955, Freygang and Landau reported a clever four-electrode scheme to measure the specific resistance of the cerebral cortex in anesthetized animals. One current electrode was placed in a well of physiological fluid overlying an exposed section of cerebral cortex. The other electrode was placed in the pharynx. In this way, a fairly uniform current density was established in the cortex under the well.

The current electrodes were made of platinized platinum and had fairly large contact areas to minimize polarization impedance. The voltage across the cortex was sensed by means of two micropipette electrodes which were connected to a differential amplifier. The applied current was a square wave derived from a phase splitter with an output impedance greater than 20 kilohms. Pulse durations of 0.3 ms to 0.7 ms were used.

In a typical run, the cortical voltage was 20 mv or less, while the voltage between current electrodes was about 1.8 volts. The common mode rejection ratio of the differential amplifier was given as 2,000. Although the current was derived from a balanced source, the common mode signal to the amplifier was not necessarily inconsequential because of probable differences in the impedance of the current paths above and below the region of the potential electrodes. To illustrate this point, suppose the common mode signal was one fourth the voltage between current electrodes or approximately 0.45 volts. Then the common mode rejection error would be somewhat greater than one percent of the cortical voltage. The fundamental frequencies of the applied square waves were greater than 700 Hz. On the basis of amplifier rejection ratio alone, it is unlikely that reliable measurements could have been made at much lower or much higher frequencies with the system described.

Most of the four-electrode studies published to date have occurred since 1960. In the first of these works, Burger and van Dongen (1960-1961) modified the original four-electrode method of Burger and van Milaan (1943) to include sinusoidal frequencies from 20 Hz to 5 kHz. The basic scheme is shown in Figure 1.4, where the rectangle with four

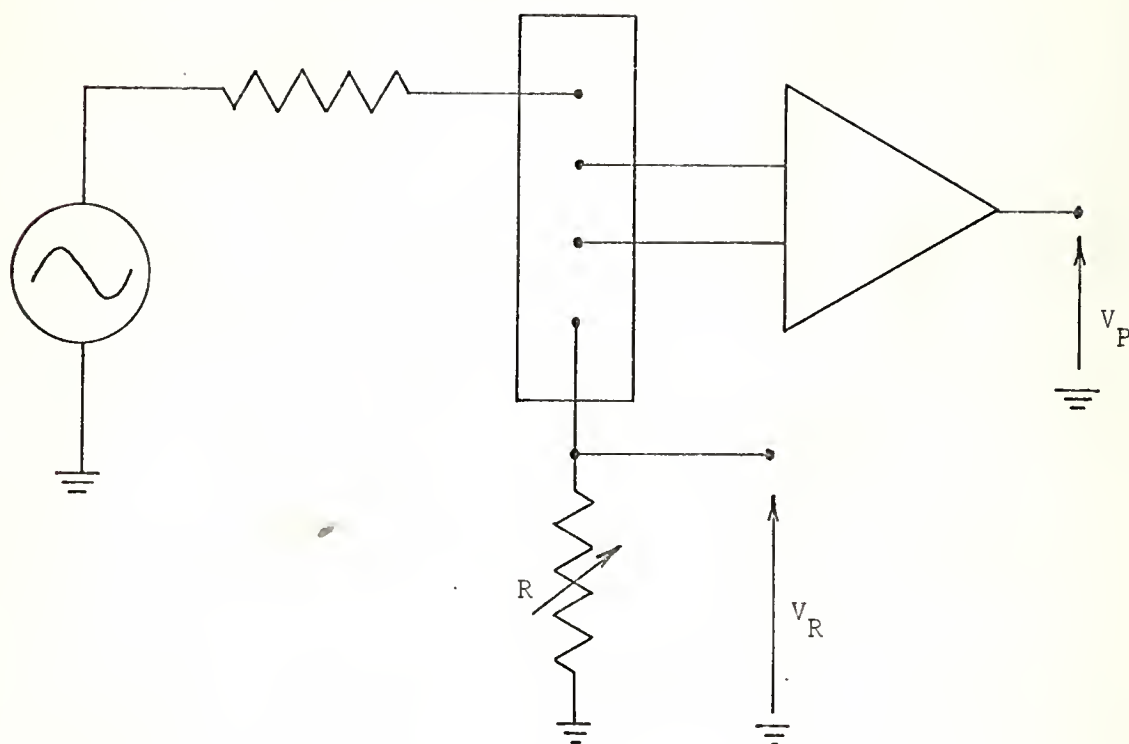


Figure 1.4. Four-Electrode Comparison Scheme

terminals represents the electrode-tissue system. The procedure was to adjust R until the amplitude of V_R was equal to that of V_P . Then the magnitude of the transfer impedance of the four-electrode system would be approximately R divided by the gain of the differential amplifier. The common mode signal to the amplifier includes one current interface voltage as well as V_R and some contribution from the tissue. This signal is likely to have been much greater than the differential signal in some of the experiments reported. The authors make almost no mention of system performance or measurement difficulties encountered. Also no technical data on the apparatus were given. This omission is unfortunate in view of the significant differences noted

between their results and those of Schwan and Kay (1956) which this investigation was meant to clarify.

Ranck (1963a) used an arrangement similar to that shown in Figure 1.4 to measure transfer impedance in rabbit cerebral cortex in acute experiments. The voltage and current signals were connected to the vertical and horizontal sweeps of an oscilloscope, respectively. The magnitude and phase of the impedance were determined from the parameters of the resulting elliptical pattern observed on the oscilloscope screen. The electrode system included three small platinum electrodes (20 to 40 micron diameter) arranged in a linear array on the exposed cortical surface. These correspond, in order, to the upper three electrodes of Figure 1.4. The fourth electrode was located remotely on the animal. The cortical electrodes were spaced at least 300 microns apart, but the array never exceeded 1.3 mm in length.

Ranck's highly assymmetrical electrode system is reminiscent of the arrangements used for three-electrode measurements on individual cells and possesses similar advantages. The polarization impedance of the remote electrode can easily be made negligible, and the voltage gradient decreases rapidly away from the cortical array. Hence, the common mode signal to the differential amplifier is of the same order as the differential signal. The common mode rejection ratio of the amplifier was given as at least 1,000, which in this case appears quite satisfactory. Requirements on amplifier input impedance were also not too difficult to meet.

The most informative discussssion of errors in a four-electrode impedance investigation was given by Ranck in a later paper (Ranck,

1966). This paper also was first to report the application of four-electrode technique to chronic impedance studies in unrestrained animals. The basic signal-sensing scheme was as shown in Figure 1.4, except that the current monitoring resistor was replaced by an operational amplifier circuit with negligible input impedance (similar to that shown in Figure 1.3). As before, the voltage and current signals were displayed as a Lissajous pattern on an oscilloscope. In addition, they were connected to a special instrument, the JB-5 lock-in amplifier, which, with auxiliary circuits, was calibrated to display the in-phase and quadrature components of the tissue voltage response with respect to the applied current.

The lock-in-amplifier uses tuned circuits and special averaging techniques which greatly increase the signal-to-noise ratio of the displayed signal. Hence, Ranck was able to measure voltage responses of the order of 20 microvolts in the presence of EEG activity of the order of 300 microvolts. This is not feasible with the Lissajous pattern method unless the signal frequency is far removed from the noise frequencies and a noise filter is used. Low current densities in the tissue (hence small voltage responses) are desirable to minimize the possible influence of the test current on the tissue impedance. This effect has yet to be ascertained.

The main electrode assembly was chronically implanted in selected sites of the rat brain. The submerged part consisted of four parallel wires (75 micron) spaced uniformly in a linear array 1 to 1.5 mm across. Each wire was roughly 1 mm long and was insulated to within about 100 microns of the tip. The wires were made of platinum and the

tips were platinized to reduce polarization impedance. Two field configurations were used. In the linear configuration, the brain electrodes were connected in the order shown in Figure 1.4. In the radial configuration, a remote electrode was used as the current return in place of an end head electrode. The latter configuration did not possess the advantage of a modest common mode signal as found in the radial configuration. Ranck made reference to this fact and noted greater difficulties and poorer results with the linear configuration.

Ranck's discussion of errors has been a source of inspiration for some of the more general treatments given in the present work. In particular, he called attention to the errors caused by parasitic resistance (leakage) and capacitance which provide undesirable coupling between the current and potential electrode conductors. In the linear configuration, Ranck found, for example, that at frequencies below 100 Hz, the parasitic resistance had to be greater than 10^8 ohms to realize a voltage sensing error of less than 1 percent. For frequencies below about 10 Hz, the requirement became greater than 10^{10} ohms. He noted the difficulty of maintaining resistances of this magnitude on the head of animals in chronic experiments. These requirements also came uncomfortably close to the nominal input resistance of the response amplifier, which was given as greater than 10^9 ohms.

Ranck neglected the phase angle of the electrode polarization impedance in his error analysis. But, he did make use of this phenomenon in testing the electrode assemblies before implantation. Hence, each assembly was checked for leakage in 0.2 percent saline at 1.5 Hz and the phase angle of the voltage response was taken as the

most sensitive indicator of error. The phase angle, if any, was due to the effect of electrode polarization capacitance. The reliability of the results obtained with this method of electrode testing is questionable for reasons explained in the following paragraphs.

As Ranck indicated, the error due to a given amount of leakage between a current electrode and a potential electrode is proportional to the product of the electrode impedances divided by the transfer impedance to be measured. Mathematically

$$|\epsilon| \propto \frac{|Z_Q|}{|Z_T|} |Z_P|$$

where Z_Q , Z_P and Z_T designate the current electrode, potential electrode, and transfer impedances, respectively. At the test frequency of 1.5 Hz, Z_Q and Z_P were largely determined by interface impedance. The interface impedance is not a sensitive function of saline concentration, since it depends mainly on a hydrogen transfer mechanism with the water. Therefore, $|Z_Q|$ and $|Z_P|$ would be expected to have much higher values in the tissue than in the saline test solution due to the masking effect of cellular components (Schwan, 1963).

The 0.2 percent saline used for the electrode tests produced approximately the same $|Z_T|$ as was found in the tissue. However, since $|Z_Q|$ and $|Z_P|$ were probably much lower in the saline than in the tissue, the simulated error would likewise be expected to be much smaller, but by the same factor squared. Suppose that isotonic saline (0.9 percent) were used for the electrode tests. Then, the ratio of $|Z_Q|$ to $|Z_T|$ in the saline would more closely simulate that found in the

tissue (assuming the cell masking factor was roughly proportional to the ratio of tissue to tissue fluid impedance). In this case, the simulated error would still be too low, but only by the factor in $|Z_p|$ to the first power. The foregoing considerations are rather significant because they imply that electrode test results obtained in pure saline do not provide a reliable indication of leakage errors.

The choice of test solution is also important with respect to errors caused by imperfect common mode rejection in the differential amplifier. The ratio of common mode signal to differential signal is approximately given by the ratio of $|Z_Q|$ to $|Z_T|$. As previously indicated, the ratio found in tissues is more closely simulated in isotonic saline than in 0.2 percent saline. In the latter case, the ratio would be too low to give a reliable indication of the common mode rejection error.

The phase angle of the voltage response was also the most sensitive indicator of error at higher frequencies where polarization impedance was negligible and electrode impedance was essentially resistive. Here, the phase angle, if any, was due entirely to capacitive coupling between the current and potential electrode conductors. The input capacitance of the response amplifier was given as 30 picofarads which is equivalent to about 5 megohms at 1 kHz. This reactance significantly loaded the potential electrodes and, in the radial configuration, caused a phase error in the apparent response of approximately 9 degrees, while the magnitude error was less than 2 percent.

The effects of parasitic resistance and capacitance were greatly magnified in the linear configuration by the high ratio of common mode

signal to differential signal which varied from approximately 40 at 1 kHz to 600 at 1.5 Hz. This high ratio was also troublesome with respect to the common mode rejection capability of the amplifier. To obtain common mode error signals of less than 1 percent, the common mode rejection ratio would have had to exceed limits ranging from 4,000 at 1 kHz to 60,000 at 1.5 Hz. The common mode rejection ratio of the system used was given as only better than 1,000. On the basis of the foregoing discussion and in concurrence with some of Ranck's remarks, it may be concluded that the results obtained with the linear configuration were unreliable at nearly all frequencies. Much of this problem lay in the extreme demands that this configuration made on the instrumentation components. Better performance could have been achieved with the instrumentation technique described in Chapters 4 and 5 of the present work.

Summary

In a broad sense, electrode polarization leads to a similar problem in every type of electrode system, which becomes worse as the electrode dimensions are reduced and the frequency is lowered. Briefly stated, the problem is to find an unknown quantity, the tissue impedance, within arbitrary accuracy limits, by taking the difference between two quantities which may become nearly equal at low frequencies. The differencing process may be done by manual and computational means (as in two-electrode and three-electrode systems) or continuously and automatically by electronic means (as in four-electrode systems). The experimental evidence indicates that the former methods are not

reliable unless the common quantity is significantly smaller than the difference quantity. In contrast, the four-electrode electronic methods are reliable and capable of high accuracy even when the common quantity is much larger than the difference quantity. This subject is considered in detail in Chapters 3 and 4 under the title of common mode rejection.

The advantages of the four-electrode method are obtained at the cost of increased complexity and additional sources of error. However, a properly designed and well-understood four-electrode experiment can be no more difficult to perform than a two-electrode experiment, all factors considered. The basis for this statement may be found in the remaining chapters of this report, which are summarized in the following paragraphs.

Chapter 2.--Chapter 2 is concerned with basic analytical techniques for describing, analyzing and designing the electrode-tissue system. Special matrix parameters are defined for the system, and the concept of interface impedance is clarified. Certain boundary effects caused by interface impedance are explained and techniques for correcting them are suggested. Further insight is provided by means of a convenient equivalent network, which is derived in terms of the matrix parameters of the system. To conclude the chapter, the matrix parameters are derived from field theory for two different electrode arrangements and illustrated numerically.

Chapter 3.--Chapter 3 is concerned with the most common method for amplifying the signal of the potential electrodes. Four major

types of measurement error are defined and analyzed. Limit expressions are derived for the parameters of the instrumentation system and associated paraphernalia. The results are illustrated numerically, using the examples of Chapter 2. Besides being of value in itself, Chapter 3 provides important definitions and background for Chapter 4.

Chapter 4.--In Chapter 4, a new instrumentation technique--the virtual-ground system--for extracting the signal of the potential electrodes is introduced. The four major types of measurement error defined in Chapter 3 are analyzed for the new system. Limit expressions are derived for the system parameters and numerical results are illustrated using the examples of Chapter 2. These results are compared with those of the common method of Chapter 3. Two additional topics are treated: the stabilization of the virtual-ground system for broad band measurements and the operation of the negative feedback filter loop for noise reduction.

Chapter 5.--In this chapter, an experimental system using the virtual-ground configuration is described. The system includes a current control scheme which was taken from the literature and adapted for broadband impedance measurements. Several experiments are reported to verify system performance and indicate the quality of results already obtained in investigations on live animals.

CHAPTER 2

MATRIX AND NETWORK DESCRIPTION OF FOUR-ELECTRODE SYSTEMS

Voltage and Current Conventions

It is convenient to assign the symbols Q_1 , P_1 , P_2 , and Q_2 to the terminals of a four-electrode system, where Q designates the current or excitation electrodes and P designates the potential or response electrodes. Let the complex terminal voltages and currents describing the state of the system be as defined in Figure 2.1.

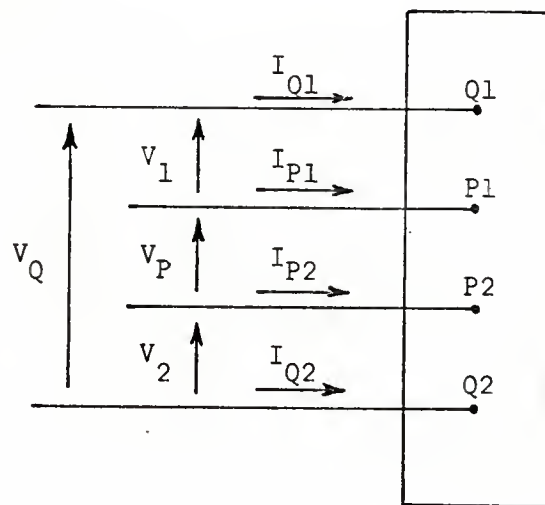


Figure 2.1. Voltage and Current Conventions for the Electrode-Tissue System

According to the laws of network theory

$$V_2 + V_P + V_1 - V_Q = 0 \quad (2.1)$$

and

$$I_{Q1} + I_{Q2} + I_{P1} + I_{P2} = 0 \quad (2.2)$$

which shows that only three voltages and three currents may be defined independently. Note that the V and I quantities usually possess in-phase and quadrature components which vary with frequency. Equations (2.1) and (2.2) each imply two equations, one for the in-phase and one for the quadrature components, with all quantities being evaluated at the same frequency.

The Impedance Parameter Matrix

In a linear system with sinusoidal excitation, the complex voltages and currents are related by a set of linear simultaneous equations with complex coefficients. It follows from Equations (2.1) and (2.2) that three independent equations are sufficient to describe the four-electrode system. Using vector and matrix notation with $V_P(f)$, $V_Q(f)$, $I_{Q1}(f)$, $I_{P1}(f)$, and $I_{P2}(f)$ as the working variables, the system equations may be written

$$\begin{bmatrix} V_P \\ V_Q \\ V_1 \end{bmatrix} \equiv \begin{bmatrix} m_{11} & m_{12} & -m_{13} \\ m_{21} & m_{22} & m_{23} \\ m_{31} & -m_{32} & -m_{33} \end{bmatrix} \begin{bmatrix} I_{Q1} \\ I_{P1} \\ I_{P2} \end{bmatrix} \quad (2.3)$$

where the m coefficients are, by definition, parameters of the electrode-tissue system and have the dimensions of complex impedance. This particular matrix form was chosen to facilitate the inclusion of interface effects and to simplify the analysis of errors given in later chapters. The minus signs are included so that the real part of each parameter will be positive in a passive system. For example, in a purely resistive system, all the parameters would be real and positive.

The m parameters of a given system may be determined experimentally or estimated, a priori, from known properties of the tissue and electrodes. In either case, one refers to the basic definitions listed in Table 2.1, which may be obtained by inspection from Equation (2.3).

TABLE 2.1
DEFINITIONS OF THE m PARAMETERS

Constraint	$I_{P1} = I_{P2} = 0$	$I_{Q1} = I_{P2} = 0$	$I_{Q1} = I_{P1} = 0$
Excitation	Q1-Q2	P1-Q2	P2-Q2
	$m_{11} \equiv \frac{V_P}{I_{Q1}}$	$m_{12} \equiv \frac{V_P}{I_{P1}}$	$m_{13} \equiv \frac{-V_P}{I_{P2}}$
	$m_{21} \equiv \frac{V_Q}{I_{Q1}}$	$m_{22} \equiv \frac{V_Q}{I_{P1}}$	$m_{23} \equiv \frac{V_Q}{I_{P2}}$
	$m_{31} \equiv \frac{V_1}{I_{Q1}}$	$m_{32} \equiv \frac{-V_1}{I_{P1}}$	$m_{33} \equiv \frac{-V_1}{I_{P2}}$

The immediate objective of most impedance measurements is to

identify the transfer impedance, m_{11} . This parameter is estimated by determining the ratio of an arbitrary measure of V_p (the nominal voltage response) to an arbitrary measure of I_{Q1} (the nominal exciting current) under the assumption that I_{p1} and I_{p2} are zero. As shown in later chapters, the other m parameters may play a significant role in determining the accuracy of the result.

In a system composed of bilateral elements, the Reciprocity Theorem from network theory shows that only six of the nine m parameters are independent. Three of them may be eliminated by means of the following relations (Appendix 1).

$$m_{22} = m_{23} + m_{11} \quad (2.4)$$

$$m_{32} = m_{12} + m_{33} - m_{11} \quad (2.5)$$

$$m_{21} = m_{31} + m_{23} + m_{11} \quad (2.6)$$

The m parameters are determined by the impedance characteristics of the tissue and the electrode-tissue interfaces and by the system geometry. These factors are considered in the remainder of the chapter.

Analysis of the m Parameters

The significance of the m parameters may be determined from a study of the general field relationships that exist within the electrode-tissue system. Consider a metal electrode in an electrolytic medium in the presence of an arbitrary current density field as shown in Figure 2.2. Let s denote an imaginary surface which surrounds, and is arbitrarily close to, the electrode such that it includes essentially only that part of the tissue which is involved in interfacial

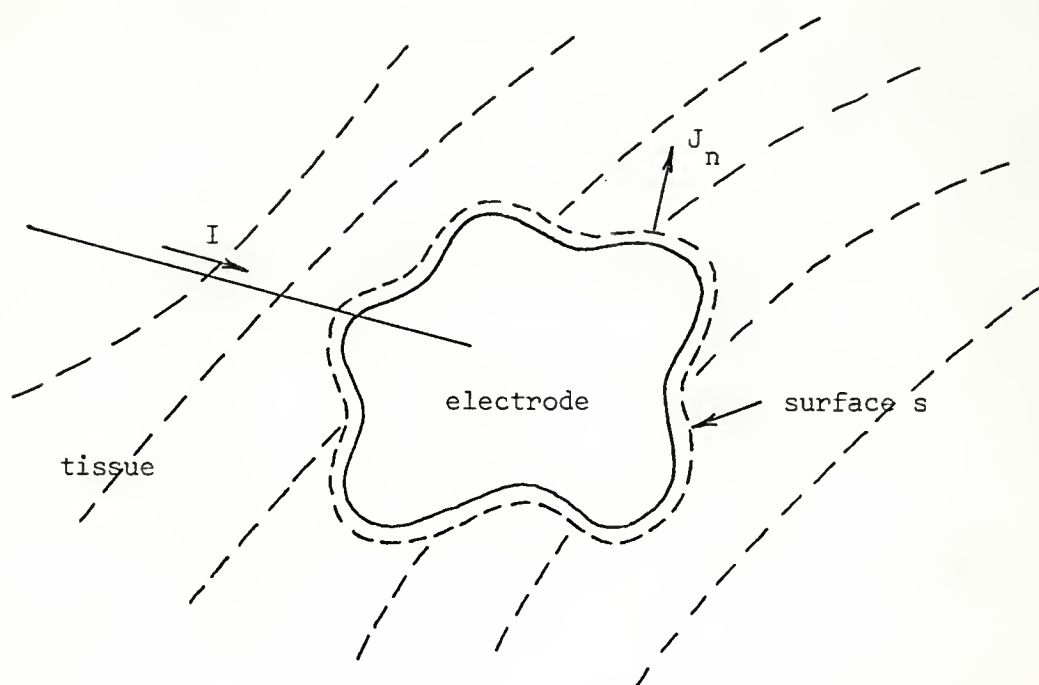


Figure 2.2. Electrode-Tissue Interface in an Arbitrary Current Field

phenomena. Then, the potential of the electrode with respect to an arbitrary point of reference in the tissue mass may be written

$$V = \bar{U} - \bar{E} \quad (2.7)$$

where \bar{E} is the average potential on s with respect to the reference point and \bar{U} is the average potential difference across the interface. It is apparent that \bar{E} is a function of the current density field and the tissue impedance, while \bar{U} is a function of the normal current density on s and the interface impedance.

At any position on s , the potential difference across the interface may, in principle, be written as the product of the complex impedance per unit area, $\chi(s)$, and the normal component of the current density, $J_n(s)$, at that point. Then the average potential difference

is given by

$$\bar{U} = \frac{1}{A} \int_s \chi J_n ds \quad (2.8)$$

where the integral is taken over all of s , A is the total surface area of s and J_n is taken as positive out of s .

A more convenient form of Equation (2.8) is obtained if the following substitutions are made

$$\chi = \bar{\chi} + \eta(s) \quad (2.9)$$

$$J_n = \bar{J}_n + v(s) \quad (2.10)$$

where $\bar{\chi}$ and \bar{J}_n are the average values of interface impedance and normal current density on s , and $\eta(s)$ and $v(s)$ are deviations from the averages, respectively. Note that by definition

$$\int_s \eta(s) ds = 0 \quad (2.11)$$

and

$$\int_s v(s) ds = 0 \quad (2.12)$$

If I designates the total electrode current in the external circuit, then from Equations (2.10) and (2.12)

$$\bar{J}_n = \frac{I}{A} \quad (2.13)$$

With Equations (2.9) through (2.13), Equation (2.8) may be rewritten

$$\bar{U} = \frac{\bar{\chi}}{A} I + \frac{1}{A} \int_s \eta v ds \quad (2.14)$$

The first term on the right in Equation (2.14) expresses the average potential difference across the interface due to current flowing through the electrode and the external circuit. The second term expresses the average potential difference across the interface due to non-uniformity in the interface impedance. For example, if the interface impedance were truly uniform, the integral would be zero because $\eta(s)$ would be zero over all of s . In most cases, the major determining factor in $\eta(s)$ is the inherent inhomogeneity of the electrode surface (Flasterstein, 1966b).

The relative importance of the terms in Equation (2.14) depends on how the electrode is used. For the current electrodes of a four-electrode system, the second term is undoubtedly negligible compared to the first. However, for the potential electrodes, where I is nominally zero, the second term may be significant (Schwan, 1963). In cases where there is a choice of position, the potential electrodes should be placed where the current density intercepted by the electrodes will be low (in a region of low potential gradient) and the voltage between the electrodes is high. In this way, v is kept to a minimum and the inhomogeneity term in Equation (2.14) is more likely to be negligible in comparison to the response voltage. For example, in the parallel wire configuration shown in Figure 2.3, the potential electrodes are placed outside rather than between the current electrodes, where the same potential difference may be recorded and the current density is smaller.

The Effective Interface Impedances

In a system of four electrodes, Equation (2.7) holds for each

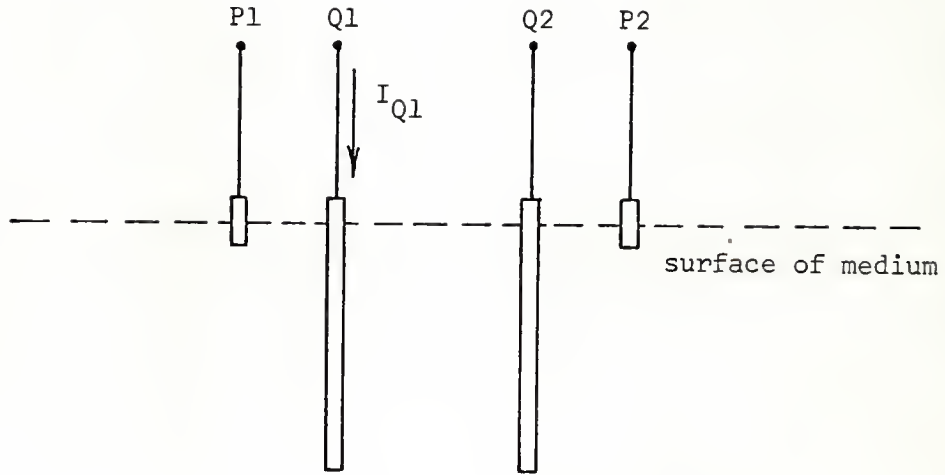


Figure 2.3. Parallel Wire Four-Electrode System

electrode. Using the appropriate subscripts and summing the electrode potentials according to Kirchhoff's Voltage Law and Figure 2.1, the vector equivalent of Equation (2.7) is found to be

$$\begin{bmatrix} V_P \\ V_Q \\ V_1 \end{bmatrix} = \begin{bmatrix} (\bar{U}_{P1} - \bar{U}_{P2}) \\ (\bar{U}_{Q1} - \bar{U}_{Q2}) \\ (\bar{U}_{Q1} - \bar{U}_{P1}) \end{bmatrix} + \begin{bmatrix} \bar{E}_P \\ \bar{E}_Q \\ \bar{E}_1 \end{bmatrix} \quad (2.15)$$

where \bar{E}_P , \bar{E}_Q , and \bar{E}_1 are the average potential differences between the surfaces of electrode pairs P1-P2, Q1-Q2, and Q1-P1, respectively.

The present investigation is primarily concerned with the effects of the first term on the right in Equation (2.14). To simplify the presentation, the term due to inhomogeneity will be neglected from this

point on. With this omission and adding the appropriate subscripts in Equation (2.14), the average interfacial potential differences of the system in Figure 2.1 become

$$\bar{U}_{Q1} = \frac{\bar{X}_{Q1}}{A_{Q1}} I_{Q1} \equiv Z_{Q1} I_{Q1} \quad (2.16)$$

$$\bar{U}_{P1} = \frac{\bar{X}_{P1}}{A_{P1}} I_{P1} \equiv Z_{P1} I_{P1} \quad (2.17)$$

$$\bar{U}_{P2} = \frac{\bar{X}_{P2}}{A_{P2}} I_{P2} \equiv Z_{P2} I_{P2} \quad (2.18)$$

$$\bar{U}_{Q2} = \frac{\bar{X}_{Q2}}{A_{Q2}} I_{Q2} \equiv Z_{Q2} I_{Q2} \quad (2.19)$$

where, for brevity, the ratio $\frac{\bar{X}}{A}$ is replaced by Z for each interface. Henceforth, Z_{Q1} , Z_{P1} , Z_{P2} , and Z_{Q2} are referred to as the effective interface impedances.

Using Equations (2.16) through (2.19), Equation (2.15) may be written

$$\begin{bmatrix} V_P \\ V_Q \\ V_1 \end{bmatrix} = \begin{bmatrix} 0 & Z_{P1} & -Z_{P2} \\ Z_{Q1}+Z_{Q2} & Z_{Q2} & Z_{Q2} \\ Z_{Q1} & -Z_{P1} & 0 \end{bmatrix} \begin{bmatrix} I_{Q1} \\ I_{P1} \\ I_{P2} \end{bmatrix} + \begin{bmatrix} E_P \\ E_Q \\ E_1 \end{bmatrix} \quad (2.20)$$

where I_{Q2} has been eliminated by means of Equation (2.2). Through the effective interface impedances, Equation (2.20) gives explicit representation to the interface potential differences and is shown diagrammatically in Figure 2.4.

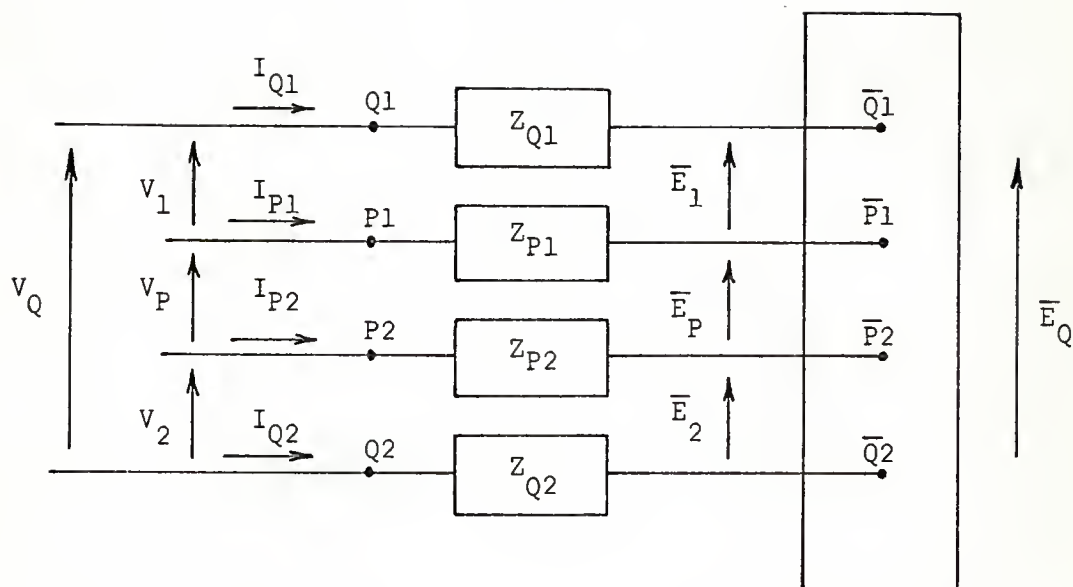


Figure 2.4. Electrode-Tissue System Showing the Effective Interface Impedances

The h Coefficients

In Figure 2.4, $\bar{Q1}$, $\bar{P1}$, $\bar{P2}$ and $\bar{Q2}$ may be viewed as the terminals of a hypothetical electrode-tissue system whose terminal voltages are equal to the average surface voltages of the real system. These voltages may be related to the electrode currents by means of a matrix equation as follows:

$$\begin{bmatrix} \bar{E}_P \\ \bar{E}_Q \\ \bar{E}_1 \end{bmatrix} \equiv \begin{bmatrix} h_{11} & h_{12} & -h_{13} \\ h_{21} & h_{22} & h_{23} \\ h_{31} & -h_{32} & -h_{33} \end{bmatrix} \begin{bmatrix} I_{Q1} \\ I_{P1} \\ I_{P2} \end{bmatrix} \quad (2.21)$$

where the definitions of the h coefficients follow from those given for the m parameters in Table 2.1 with the appropriate substitutions.

From Equations (2.20) and (2.21), it is evident that the impedance parameter matrix in Equation (2.3) is given by

$$\begin{bmatrix} m_{11} & m_{12} & -m_{13} \\ m_{21} & m_{22} & m_{23} \\ m_{31} & -m_{32} & -m_{33} \end{bmatrix} = \begin{bmatrix} 0 & Z_{P1} & -Z_{P2} \\ Z_{Q1}+Z_{Q2} & Z_{Q2} & Z_{Q2} \\ Z_{Q1} & -Z_{P1} & 0 \end{bmatrix} + \begin{bmatrix} h_{11} & h_{12} & -h_{13} \\ h_{21} & h_{22} & h_{23} \\ h_{31} & -h_{32} & -h_{33} \end{bmatrix} \quad (2.22)$$

Note that for all frequencies

$$m_{11} = h_{11} \quad (2.23)$$

and

$$m_{33} = h_{33} \quad (2.24)$$

At low frequencies (e.g., below 100 Hz), the elements in the interface impedance matrix are much larger than those in the h matrix in all except the 11 and 33 positions. At high frequencies (e.g., above

100 kHz), the elements in the interface impedance matrix tend to become small compared to those in the h matrix. However, in many cases, the interface impedances may not become negligible before the errors of measurement exceed permissible limits. This possibility is embodied in the results of succeeding chapters.

It may appear that interface effects are expressed entirely by the interface impedance matrix. This statement is only approximately true. The geometry of the current field is determined mainly by the electrode configuration. However, it is also influenced in varying degree by the frequency-dependent boundary conditions imposed by the impedance of the electrode-tissue interfaces. This factor is not likely to be important except with respect to its direct effect on h_{11} . For the sake of completeness and to demonstrate the complexity of the four-electrode field problem, a brief discussion of possible boundary effects is in order. The examples that follow are of a hypothetical nature and have not been studied in experimental or analytical detail. The existence of boundary condition effects is evidenced by certain anomalous behavior of electrodes in saline which is difficult to explain in terms of other sources of error.

Examples of boundary condition effects

To indicate how interfacial boundary conditions may affect h_{11} , consider again the electrode configuration of Figure 2.3. The exposed tips of the potential probes are located near the surface of the tissue mass where the current density field is fairly planar. Assume that a sinusoidal current of constant amplitude, I_{Q1} , excites the system. At high frequencies, where the interface impedance is small, the current

density distribution along Q1 and Q2 is determined primarily by the configuration of the metallic boundaries and is indicated qualitatively in Figure 2.5 (high). The rise toward the electrode tips is due to

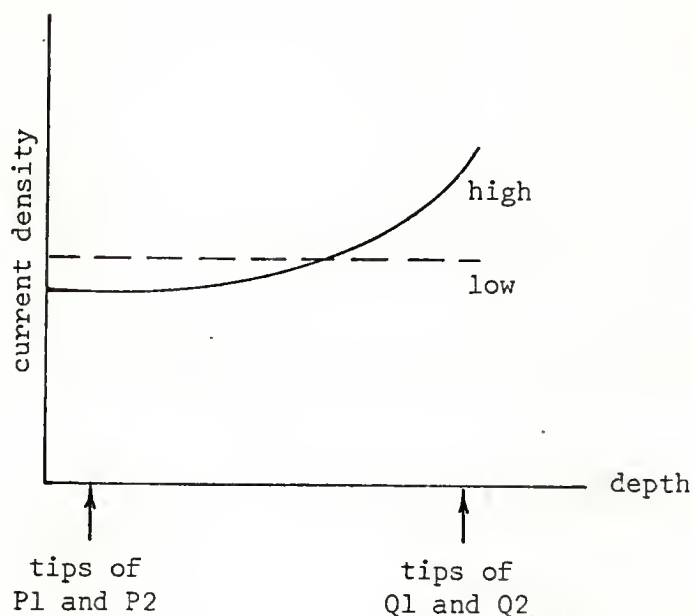


Figure 2.5. Electrode Current Density in the System of Figure 2.3

fringing into the tissue mass. At low frequencies, the interface impedances of Q1 and Q2 are large compared to the tissue impedance, and they tend to smooth the current density distribution, as shown in the same figure (low). Since the total current is constant, the areas between the low and high frequency graphs are equal, and there is more current at low frequencies in the field of P1 and P2 than at high frequencies. The importance of this effect should depend on the relative dimensions of the current electrodes and become smaller as the electrode length is increased.

A useful expression for h_{11} is

$$h_{11} = \Gamma\psi \quad (2.25)$$

where Γ is a geometrical factor and ψ is the specific impedance of the tissue. Since Γ reflects the current density distribution, it varies with frequency and for the configuration of Figure 2.3 takes the general form shown in Figure 2.6. At low frequencies, where the effect

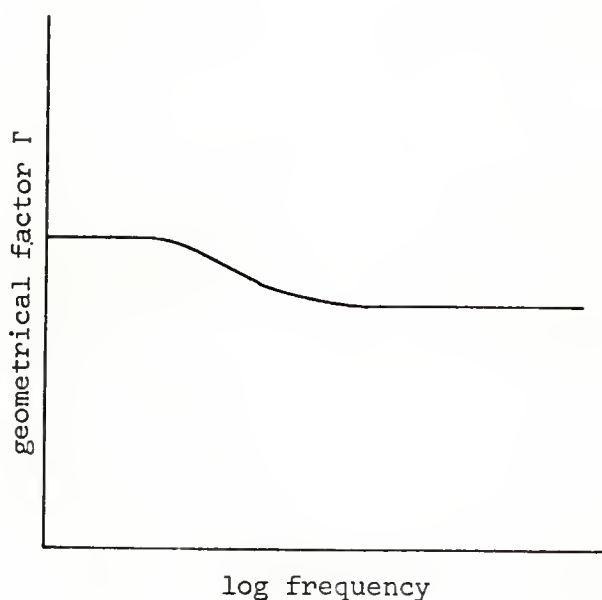


Figure 2.6. Frequency Dispersion of the Geometrical Factor for the System of Figure 2.3

of interface impedance is much greater than that of the tissue impedance, the graph is flat. When the impedances are comparable, Γ decreases with frequency and asymptotically approaches a value corresponding to zero interface impedance.

Since the electrode-tissue system is assumed to be linear and passive, it should obey the phase-magnitude relationships of network

theory (Bode, 1945). Hence, the magnitude of h_{11} cannot vary with frequency without a concomitant change in its phase angle as well. This implies that there can be no frequency dependence of $|\Gamma|$ unless Γ is a complex number. Indeed, careful consideration of the phenomenon illustrated by Figure 2.5 indicates that the phase angle of the current density may vary along the electrode length even though the phase of the total current is fixed. The phase of the current toward the tips of Q1 and Q2 would tend to be positive, while that toward the tips of P1 and P2 would tend to be negative, with respect to the phase of the total current. Hence, in agreement with network theory, a decrease in $|h_{11}|$ (or $|\Gamma|$) with frequency would be accompanied by a negative phase angle in h_{11} (or Γ). In view of these considerations, the ordinates in Figures 2.5 and 2.6 should be interpreted as the magnitude of the quantities indicated. Further, the areas between the high and low curves in Figure 2.5 are not equal since phase angles must be taken into account.

Experimentally, Γ is often estimated by testing the electrode system in saline of known specific resistance. The frequency dependence of Γ may be expected to vary with the ratio of interface impedance to saline impedance. For example, as saline concentration is increased, this ratio increases, and the dispersion in Γ may be expected to occur at higher frequencies. If the frequency dependence of Γ is significant in a given system, it becomes necessary to use a saline concentration which produces a similar ratio of interface impedance to specific impedance as occurs in the tissue to be measured. This problem is complicated by the masking effect of cells in the tissue on the interface impedance. Hence, rather than use saline of approximately the

same specific impedance as the tissue, the saline impedance should be like that of the extracellular fluid which is much lower.

Another possible boundary condition effect on h_{11} is due to non-uniformity of the interface impedance along the electrode surface. Non-uniformity at the potential electrode interfaces has already been discussed in connection with Equation (2.14). When it occurs at the current electrode interfaces, it may alter the current distribution in varying and indeterminate ways. For example, the low frequency plot in Figure 2.5 might actually have an irregular shape which varies spontaneously with time. Further, if the phase angle of the interface impedance varies over the electrode surface, Γ may become a complex number introducing an erroneous phase angle in h_{11} .

The guard electrode principle.--In the system of Figure 2.3, the constancy and definition of the current field in the potential electrode region may be improved by using two electrically separate sections for one of the current electrodes. The two sections should appear continuous except for a minute break occurring at an arbitrary point below the potential electrode tips. The controlled exciting current is caused to flow through the upper section, while the potential of the lower section is made to follow the potential developed by the upper section by means of external circuitry. From the field viewpoint, the two sections appear as a single electrode, but with the current in the region of interest under direct control. The guard electrode principle, as it is commonly called, may be applied in many different configurations (see, for example, Van Harreveld, et al., 1963; Graham, 1965b).

The Equivalent Network

The significance of interface impedance and geometrical factors is enhanced if the four electrode system is viewed in terms of an equivalent network. Consider the hypothetical system described by Equation (2.21). As indicated earlier for the m parameters, in a system obeying reciprocity, only six of the nine h coefficients are independent. Such a system may be represented by a network with six independent impedance elements. A convenient form for this network is shown in Figure 2.7 where W denotes complex impedance. This

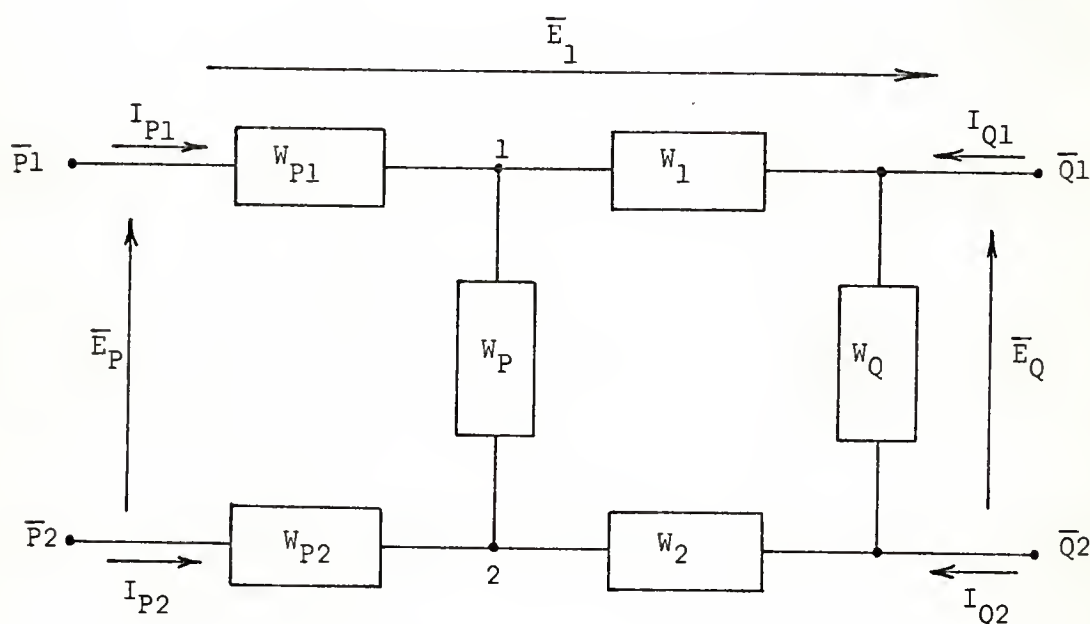


Figure 2.7. Equivalent Network for the Hypothetical System

configuration was chosen because it places in evidence certain implicit properties of the electrode-tissue system. For example, W_{P1} and W_{P2} may be interpreted as electrode impedances which characterize the effect

of drawing current through the potential probes. The remaining four elements split the exciting current into two parts: one passing through W_1 , W_P , and W_2 , which generates the response voltage between points 1 and 2, and one passing through W_Q , which, in a sense, is wasted. In many geometries, the effect of W_Q is negligible, and the network simplifies to a double tee form.

The matrix equation governing the network of Figure 2.7 is

$$\begin{bmatrix} \bar{E}_P \\ \bar{E}_Q \\ \bar{E}_1 \end{bmatrix} = \begin{bmatrix} \gamma W_P & (\gamma W_P + \frac{W_1}{D} W_P + W_{P1}) & -(W_{P2} + \frac{W_2}{D} W_P) \\ \gamma(W_1 + W_2 + W_P) & \gamma(W_2 + W_P) & \gamma W_2 \\ \gamma W_1 & -(\frac{W_1}{D} W_2 + \frac{W_1}{D} W_P + W_{P1}) & -\frac{W_1}{D} W_2 \end{bmatrix} \begin{bmatrix} I_{Q1} \\ I_{P1} \\ I_{P2} \end{bmatrix} \quad (2.26)$$

where

$$\gamma \equiv \frac{W_Q}{W_1 + W_2 + W_P + W_Q} \quad (2.27)$$

and

$$D \equiv W_1 + W_2 + W_P + W_Q = \frac{W_1 + W_2 + W_P}{1 - \gamma} \quad (2.28)$$

Setting the matrices of Equations (2.21) and (2.26) equal, the following expressions are found for the network elements

$$W_{P1} = h_{12} - h_{11} \left(1 + \frac{h_{33}}{h_{23}}\right) \quad (2.29)$$

$$W_{P2} = h_{13} - h_{11} \frac{h_{33}}{h_{31}} \quad (2.30)$$

$$W_P = \frac{1}{\gamma} h_{11} \quad (2.31)$$

$$W_1 = \frac{1}{\gamma} h_{31} \quad (2.32)$$

$$W_2 = \frac{1}{\gamma} h_{23} \quad (2.33)$$

$$W_Q = \frac{1}{\gamma} \frac{h_{23}h_{31}}{h_{33}} \quad (2.34)$$

and

$$\frac{1}{\gamma} = 1 + \frac{h_{33}h_{21}}{h_{23}h_{31}} \quad (2.35)$$

In general, the network elements are frequency dependent through the tissue impedance and the interfacial boundary conditions.

As noted earlier, the immediate objective of four-electrode measurements is to identify h_{11} . In terms of the equivalent network

$$h_{11} = \gamma W_P \quad (2.36)$$

where γ , as defined in Equation (2.27), is the fraction of I_{Q1} which flows through W_P when I_{P1} and I_{P2} are zero. As shown in the examples at the end of the chapter, the value of γ depends on the electrode configuration, but it may not be greater than unity.

To complete the equivalent network, the effective interface impedances are added as indicated in Figure 2.8. At low frequencies (e.g., below 100 Hz), Z_{P1} and Z_{P2} are much larger than W_{P1} and W_{P2} , respectively. At high frequencies, the interface impedances should become negligible in the limit. However, as indicated for the matrix

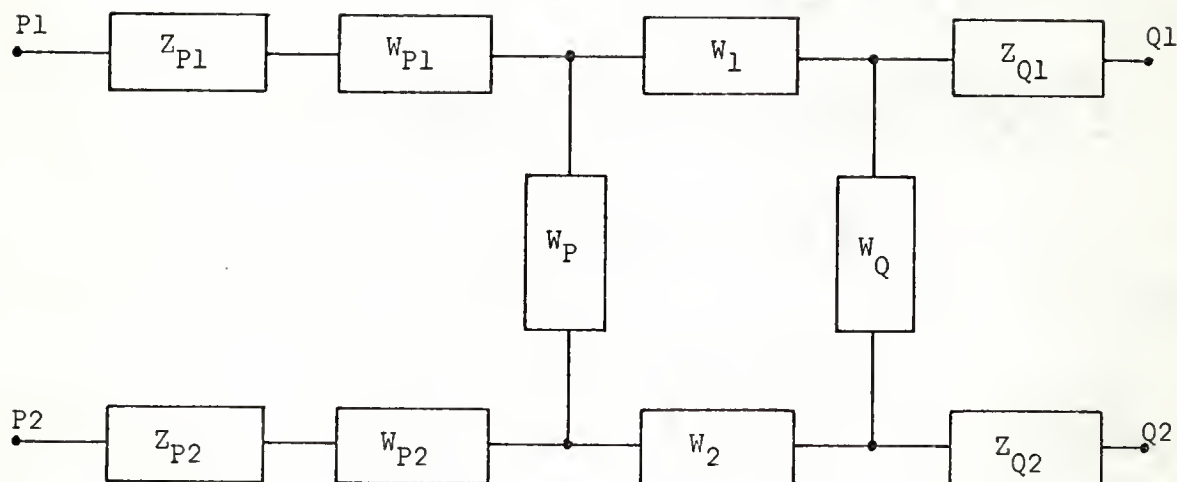


Figure 2.8. Complete Equivalent Network of the Electrode-Tissue System

parameters of Equation (2.22), this condition may not occur before the errors of measurement exceed permissible limits.

In the topics treated later in this work, the matrix parameters are used almost exclusively because they are more basic, easier to manipulate, and lead to more concise results. However, some phenomena are more readily understood when viewed in terms of the equivalent network.

Examples of Impedance Parameter Matrices

The major results of this chapter are illustrated in the examples that follow. To simplify the computation, the configurations

are idealized, and the effect of interfacial boundary conditions on the h coefficients is neglected. It is assumed that all electrodes have the same average interface impedance per unit area ($\bar{\chi}$), and the impedance medium is homogeneous with respect to the dimensions of the main field region. The specific impedance of the medium is denoted by ψ .

The h coefficients are found from the basic definitions in Table 2.1 with appropriate modifications (compare Equations [2.3] and [2.21]). The effective interface impedances follow from the definitions in Equations (2.16) through (2.19). Finally, the network elements may be calculated from Equations (2.29) through (2.35), if desired. For convenience, the results are tabulated as matrices following the form of the right hand terms in Equation (2.22).

In each example, numerical values are illustrated for the matrix elements at low and high frequencies. The computations make use of the approximate values of $\bar{\chi}$ and ψ shown in Table 2.2, which are based on observations by the author using stainless steel electrodes in 0.9 per cent (isotonic) saline. The factor $e^{-j\theta}$ is defined in Chapter 1.

TABLE 2.2

APPROXIMATE VALUES OF $\bar{\chi}$ AND ψ FOR STAINLESS STEEL ELECTRODES
IN ISOTONIC SALINE

Frequency	$\bar{\chi}$ ohm-cm ²	ψ ohm-cm
3 Hz	1,000 e^{-j72°	60 e^{j0°
100 kHz	0.5 e^{-j72°	60 e^{j0°

Here, it indicates a phase angle of minus 72 degrees. The complex number equivalent is

$$\begin{aligned}
 e^{-j72^\circ} &= \cos 72^\circ - j\sin 72^\circ \\
 &= 0.31 - j0.95
 \end{aligned}$$

The examples are calculated for the system shown in Figure 2.9, which consists of four hemispherical electrodes set into the surface of a semi-infinite impedance medium. Electrode radii and separation are represented by r and d with appropriate subscripts, respectively.

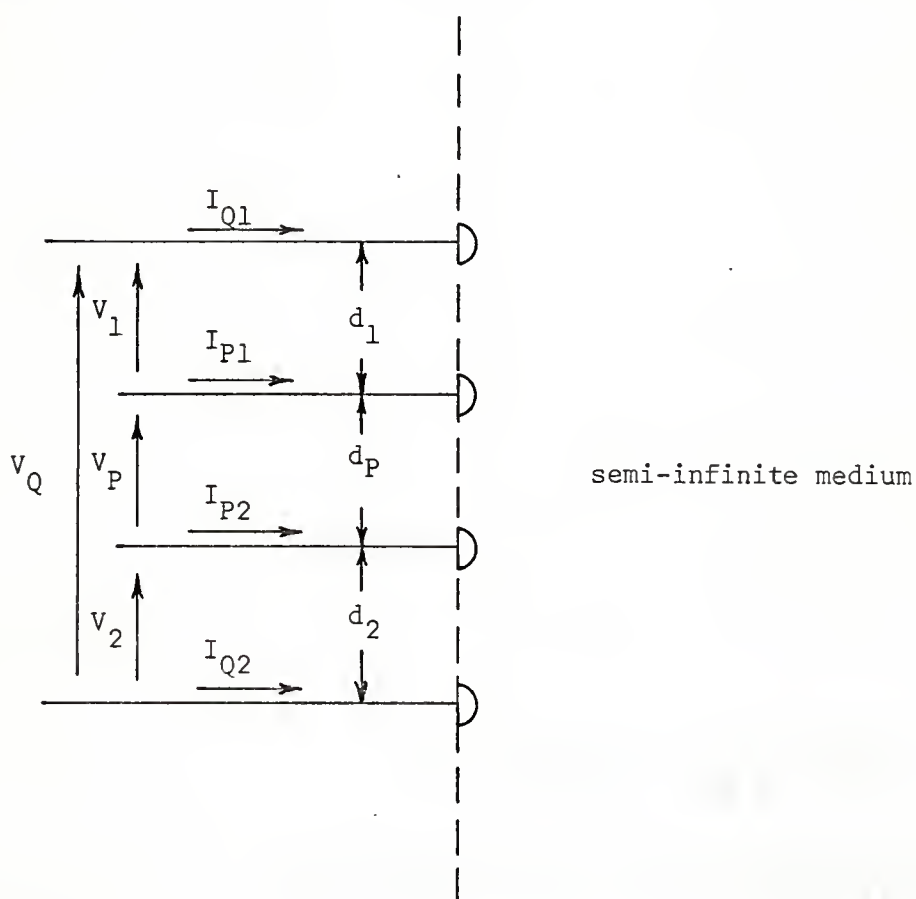


Figure 2.9. Four-Electrode System with Hemispherical Electrodes

Example 1

The approximate element expressions in Table 2.3 are determined for the following geometrical conditions

$$d_1 = d_P = d_2 \equiv d$$

and

$$r_{Q1} = r_{P1} = r_{P2} = r_{Q2} \equiv r \ll d$$

The numerical results correspond to $d=0.2$ cm and $r=0.01$ cm.

TABLE 2.3
MATRIX ELEMENTS FOR EXAMPLE 1

Frequency	Interface Impedance	h Coefficients
All $\bar{X}/\pi r^2$	$\begin{bmatrix} 0 & 1/2 & -1/2 \\ 1 & 1/2 & 1/2 \\ 1/2 & -1/2 & 0 \end{bmatrix}$	$\psi/\pi \begin{bmatrix} 1/2d & 1/2r & -1/2r \\ 1/r & 1/2r & 1/2r \\ 1/2r & -1/2r & -1/6d \end{bmatrix}$
3 Hz $10^6 e^{-j72}$	$\begin{bmatrix} 0 & 1.6 & -1.6 \\ 3.2 & 1.6 & 1.6 \\ 1.6 & -1.6 & 0 \end{bmatrix}$	$\begin{bmatrix} 47.7 & 955 & -955 \\ 1910 & 955 & 955 \\ 955 & -955 & -15.9 \end{bmatrix}$
100 kHz e^{-j72}	$\begin{bmatrix} 0 & 800 & -800 \\ 1600 & 800 & 800 \\ 800 & -800 & 0 \end{bmatrix}$	$\begin{bmatrix} 47.7 & 955 & -955 \\ 1910 & 955 & 955 \\ 955 & -955 & -15.9 \end{bmatrix}$

In this example, γ is approximately unity at all frequencies.

Example 2

The geometrical conditions for this example are

$$d_1 = d_p \equiv d \quad d_2 \gg d$$

$$r_{Q1} = r_{P1} = r_{P2} \equiv r \ll d \quad r_{Q2} = 2d$$

The approximate element expressions are given in Table 2.4, where the numerical results correspond, as before, to $d=0.2$ cm and $r=0.01$ cm.

TABLE 2.4
MATRIX ELEMENTS FOR EXAMPLE 2

Frequency	Interface Impedance	h Coefficients
All $X/2\pi$	$\begin{bmatrix} 0 & 1/r^2 & -1/r^2 \\ 1/r^2 & 1/4d^2 & 1/4d^2 \\ 1/r^2 & -1/r^2 & 0 \end{bmatrix}$	$\psi/2\pi \begin{bmatrix} 1/2d & 1/r & -1/r \\ 1/r & 3/2d & 1/d \\ 1/r & -1/r & -1/2d \end{bmatrix}$
3 Hz $10^6 e^{-j72}$	$\begin{bmatrix} 0 & 1.6 & -1.6 \\ 1.6 & 0.001 & 0.001 \\ 1.6 & -1.6 & 0 \end{bmatrix}$	$\begin{bmatrix} 23.8 & 955 & -955 \\ 955 & 71.4 & 47.7 \\ 955 & -955 & -23.8 \end{bmatrix}$
100 kHz e^{-j72}	$\begin{bmatrix} 0 & 800 & -800 \\ 800 & 0.5 & 0.5 \\ 800 & -800 & 0 \end{bmatrix}$	$\begin{bmatrix} 23.8 & 955 & -955 \\ 955 & 71.4 & 47.7 \\ 955 & -955 & -23.8 \end{bmatrix}$

In this example, γ is 2/3 at all frequencies.

Concluding Remarks

The analysis in this and succeeding chapters uses methods of linear mathematics which assume that the electrode-tissue system is linear throughout. In practice, while the exciting and observed variables may be linearly related, the voltages and currents at the current electrode interfaces may not necessarily be so, depending on the current densities and frequencies encountered. However, this discrepancy detracts little from the value of the linear approach in understanding and estimating system performance. A linear analysis also serves as a basis for the inclusion of nonlinear effects.

CHAPTER 3

ERRORS IN THE IDENTIFICATION OF TRANSFER IMPEDANCE BY THE CLASSICAL METHOD

Introduction

The classical mode of operation in four-electrode measurements is to ground one current electrode and record differentially from the potential electrodes. The purpose of this chapter is to define and analyze the errors of this method and provide a basis of comparison for the more advanced technique in the next chapter.

Errors in the identification of m_{11} include four major types. Briefly, they are

1. loading error
2. common mode rejection error
3. current control error
4. noise

Each of these errors is discussed and the first three are analyzed in detail in this chapter.

A basic block diagram for impedance measurements is shown in Figure 3.1. The signal-processing and display systems are irrelevant to the present study and have been omitted. The connecting system comprises all the conductors, connectors, and supporting materials that link the electrode-tissue system to the instrumentation. The electrode-tissue system includes the tissue and only those parts of the metal

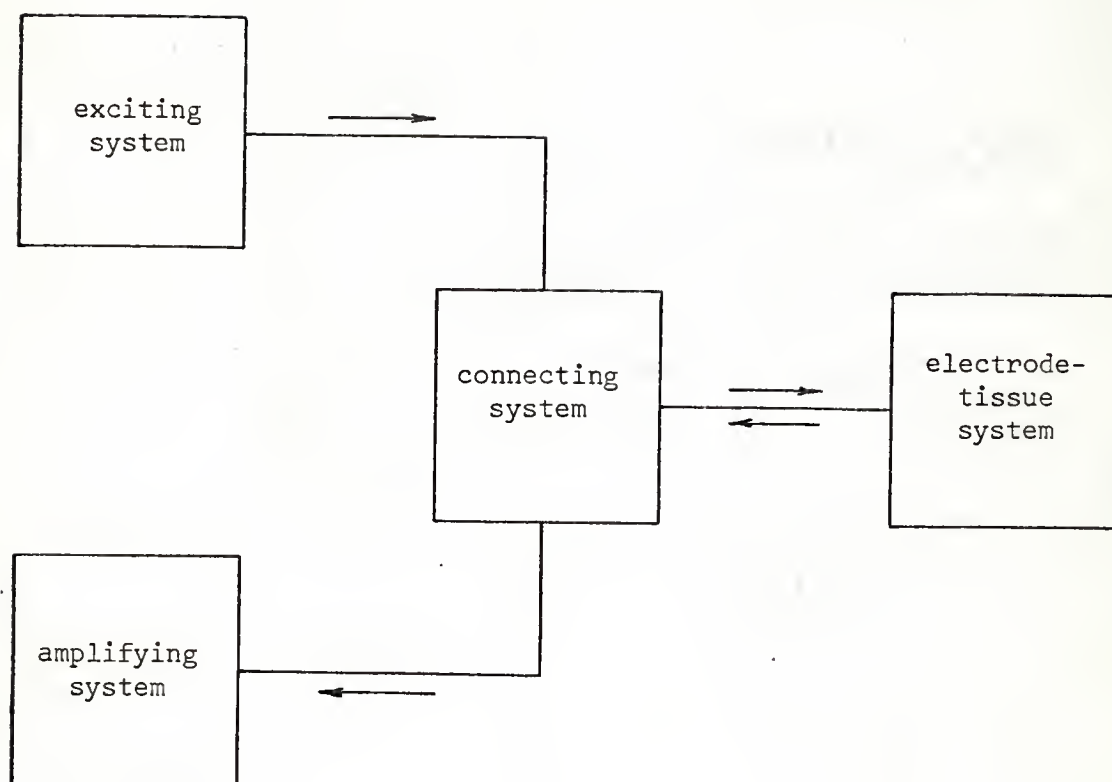


Figure 3.1. Basic Block Diagram for Impedance Measurements

electrodes which are in contact with the tissue. The exciting system usually includes a signal generator and means for controlling or sensing the applied current. The amplifying system amplifies the voltage response.

Loading Error

The term loading admittance will be used to refer to the extraneous admittances in an impedance experiment that permit undesirable currents to flow in the electrode-tissue system. For clarity, it may be viewed as consisting of four arbitrarily defined classes of components:

1. transverse admittance
2. cable admittance
3. amplifier input admittance
4. ground admittance

Transverse admittance.--Transverse admittance occurs in the connecting system and denotes parasitic current paths between any or all of the signal conductors. It arises from fixed and indeterminate properties of the insulators which support the electrodes and various connectors. Indeterminate properties are primarily due to bulk and surface contamination of the insulators by such media as blood, saline, water, and solder flux. Since it has a somewhat amorphous origin, transverse admittance is appropriately described by means of a 3 by 3 matrix, which may be converted to an equivalent network. If the transverse admittance obeys reciprocity, the matrix and the network each contain six independent elements.

Cable and amplifier input admittance.--These classes of admittance are commonly specified in terms of finite elements between ground and the signal conductors. Elements may also occur between the conductors directly.

Ground admittance.--Ground admittance encompasses all stray current paths occurring between the mass of the tissue and ground. In a practical sense, it may arise unintentionally by contact with grounded objects such as equipment, people, and wet surfaces. For present purposes, the manner in which the ground admittance is distributed need not be known. It is hereafter represented as a

finite element, connected between ground and an arbitrary point in the tissue.

The first three classes of loading admittance may be viewed as a four-terminal network in parallel with the electrode-tissue system. This network is indicated by $Q1'$, $P1'$, $P2'$, and $Q2'$ in Figure 3.2. In the same figure, ground admittance is represented by Y_g .

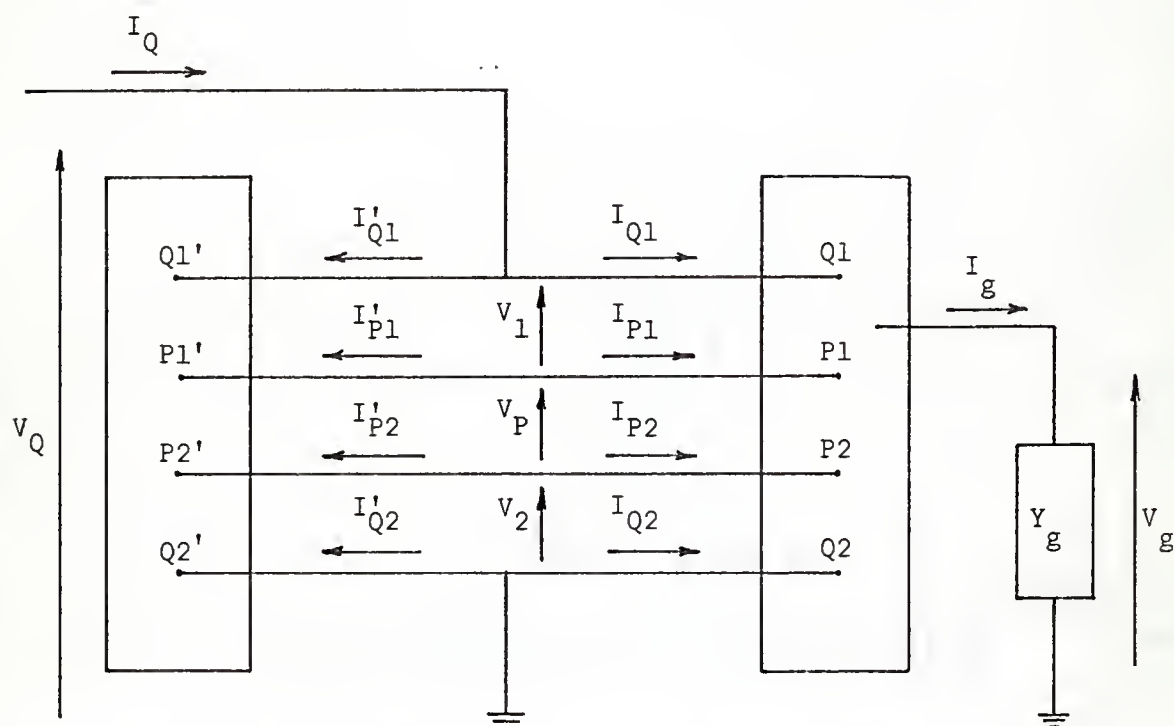


Figure 3.2. Schematic Diagram of the Electrode-Tissue and Loading Admittance Systems

The desired parameter of the electrode-tissue system, m_{11} , is estimated as the ratio of the voltage response, V_P , to the source current, I_Q . According to the definition of m_{11} in Table 2.1, the result is based on the assumption that I_{P1} and I_{P2} are zero, and that I_Q , I_{Q1} and $-I_{Q2}$ are equal. This assumption is valid only if the

loading currents I'_{Q1} , I'_{P1} , I'_{P2} and I_g are zero. Each non-zero loading current causes an error in the estimated value of m_{11} , which, by definition, is the loading error of that current.

The errors of admittance classes 1, 2, and 3 are analyzed together in the next section. For clarity, the error due to ground admittance is treated separately.

Errors Due to Admittance Classes 1, 2, and 3

It is convenient to represent the first three classes of loading admittance by the equivalent network defined in Figure 3.3 which contains six independent elements. The current vector of this network is

$$\begin{bmatrix} I'_{Q1} \\ I'_{P1} \\ I'_{P2} \end{bmatrix} = \begin{bmatrix} Y_3 & Y_Q & (Y_1+Y_3) \\ Y_P & Y_4 & -(Y_1+Y_4) \\ -(Y_P+Y_2+Y_3) & Y_2 & -(Y_2+Y_3) \end{bmatrix} \begin{bmatrix} V_P \\ V_Q \\ V_1 \end{bmatrix} \quad (3.1)$$

With reference to Figure 3.2, the current vector of the electrode-tissue system is given by

$$\begin{bmatrix} I_{Q1} \\ I_{P1} \\ I_{P2} \end{bmatrix} = \begin{bmatrix} I_Q \\ 0 \\ 0 \end{bmatrix} - \begin{bmatrix} I'_{Q1} \\ I'_{P1} \\ I'_{P2} \end{bmatrix} \quad (3.2)$$

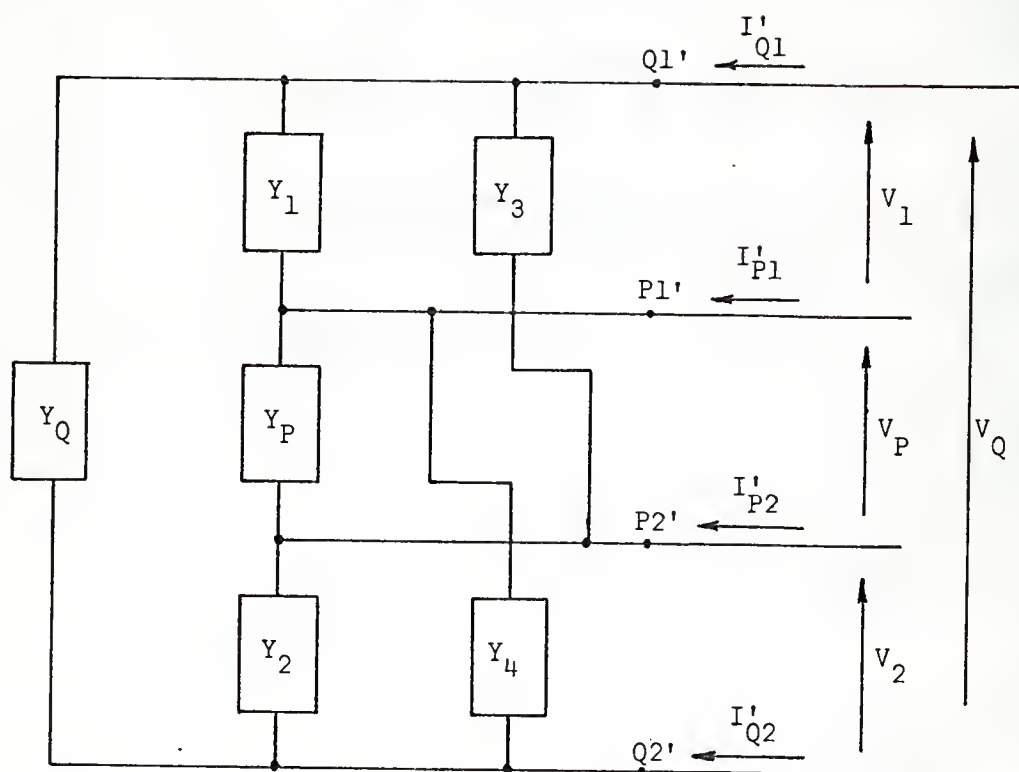


Figure 3.3. Equivalent Network for Loading Admittance Classes 1, 2, and 3

and from Equation (2.3), the voltage vector is

$$\begin{bmatrix} V_P \\ V_Q \\ V_1 \end{bmatrix} = \begin{bmatrix} m_{11} & m_{12} & -m_{13} \\ m_{21} & m_{22} & m_{23} \\ m_{31} & -m_{32} & -m_{33} \end{bmatrix} \begin{bmatrix} I_{Q1} \\ I_{P1} \\ I_{P2} \end{bmatrix} \quad (3.3)$$

It follows from Equations (3.2) and (3.3) that

$$V_P = m_{11}I_Q - m_{11}I'_{Q1} - m_{12}I'_{P1} + m_{13}I'_{P2} \quad (3.4)$$

where the terms involving I'_{Q1} , I'_{P1} and I'_{P2} are, by definition, loading errors in V_P which ideally should be zero. Dividing these terms by V_P and substituting for the currents from Equation (3.1), the relative loading errors in V_P may be written

$$\alpha_{Q1} \equiv \frac{-m_{11}I'_{Q1}}{V_P} = -m_{11} \left[\frac{V_Q}{V_P} Y_Q + \left(1 + \frac{V_1}{V_P}\right) Y_3 + \frac{V_1}{V_P} Y_1 \right] \quad (3.5)$$

$$\alpha_{P1} \equiv \frac{-m_{12}I'_{P1}}{V_P} = -m_{12} \left[\left(\frac{V_Q}{V_P} - \frac{V_1}{V_P}\right) Y_4 - \frac{V_1}{V_P} Y_1 + Y_P \right] \quad (3.6)$$

and

$$\alpha_{P2} \equiv \frac{m_{13}I'_{P2}}{V_P} = m_{13} \left[\left(\frac{V_Q}{V_P} - \frac{V_1}{V_P} - 1\right) Y_2 - \left(1 + \frac{V_1}{V_P}\right) Y_3 - Y_P \right] \quad (3.7)$$

The operating condition of primary interest in four-electrode measurements occurs when α_{Q1} , α_{P1} and α_{P2} are quite small. Under this condition, it is possible to approximate the voltage ratios in the bracketed terms of Equations (3.5), (3.6), and (3.7) by expressions involving only the m parameters. The procedure is justified by the fact that when the α are small, the errors in the approximating expressions will also be small as explained in the next paragraph.

According to Equation (3.3), V_P , V_Q , and V_1 each include a contribution from I_{P1} and I_{P2} . If one considers the geometrical and

interfacial properties of four-electrode systems, it is not difficult to see that V_1 and especially V_Q are, in most cases, less sensitive than V_P with respect to I_{P1} and I_{P2} . In the analysis that follows, the error in V_P due to these currents is required to be less than $0.05V_P$ in magnitude. It is reasonable to assume, therefore, that, under this condition, the corresponding errors in V_Q and V_1 will similarly be less than $0.05 V_Q$ and $0.05 V_1$, respectively.

To determine the voltage ratios, the errors in V_P , V_Q and V_1 due to I_{P1} and I_{P2} will be neglected in accord with the foregoing discussion. With this understanding, Equation (3.3) yields

$$V_P \approx m_{11}I_{Q1} \quad (3.8)$$

$$V_Q \approx m_{21}I_{Q1} = (m_{31} + m_{23} + m_{11})I_{Q1} \quad (3.9)$$

and

$$V_1 \approx m_{31}I_{Q1} \quad (3.10)$$

where the dependent parameter, m_{21} , has been replaced by means of Equation (2.6). It follows that the voltage ratios are

$$\frac{V_1}{V_P} \approx \frac{m_{31}}{m_{11}} \quad (3.11)$$

and

$$\frac{V_Q}{V_P} \approx \frac{m_{31} + m_{23} + m_{11}}{m_{11}} \quad (3.12)$$

Using Equations (3.11) and (3.12), the expressions for the relative errors become

$$\alpha_{Q1} \approx -[(m_{11} + m_{31} + m_{23})Y_Q + (m_{11} + m_{31})Y_3 + m_{31}Y_1] \quad (3.13)$$

$$\alpha_{P1} \approx \frac{-m_{12}}{m_{11}} [(m_{11} + m_{23})Y_4 - m_{31}Y_1 + m_{11}Y_P] \quad (3.14)$$

$$\alpha_{P2} \approx \frac{m_{13}}{m_{11}} [m_{23}Y_2 - (m_{11} + m_{31})Y_3 - m_{11}Y_P] \quad (3.15)$$

Magnitude and phase errors

Before continuing with the analysis of loading error, it is appropriate to determine how the error is manifested in the experimental results. The experimental estimation of the desired impedance parameter, m_{11} , is defined by

$$\hat{m}_{11} \equiv \frac{V_P}{I_Q} \quad (3.16)$$

If the total relative loading error in V_P due to admittance classes 1, 2, and 3 (i.e., the sum of α_{Q1} , α_{P1} and α_{P2}) is designated by α_L ,

then, from Equation (3.4)

$$\hat{m}_{11} = \frac{m_{11}}{1 - \alpha_L} \quad (3.17)$$

It follows from Equation (3.17) that the relative magnitude error in \hat{m}_{11} is

$$M \equiv \frac{|\hat{m}_{11}| - |m_{11}|}{|m_{11}|} = \frac{1}{|1 - \alpha_L|} - 1 \quad (3.18)$$

and the phase error is

$$\phi \equiv \angle \hat{m}_{11} - \angle m_{11} = - \angle (1 - \alpha_L) \quad (3.19)$$

To study the dependence of the magnitude and phase errors on α_L , consider the phasor diagram shown in Figure 3.4. If α_L is allowed to rotate in the complex plane, the algebraic signs of M and ϕ vary as indicated in Table 3.1. For a given $|\alpha_L|$, the relative magnitude error becomes maximum when the angle of α_L is 0 or 180 degrees, and the phase error becomes maximum when the angle of α_L is $\pm(90 - \sin^{-1}|\alpha_L|)$ degrees. For small $|\alpha_L|$, the maximum errors may be written

$$M \approx \pm |\alpha_L| \quad (3.20)$$

with zero phase error, and

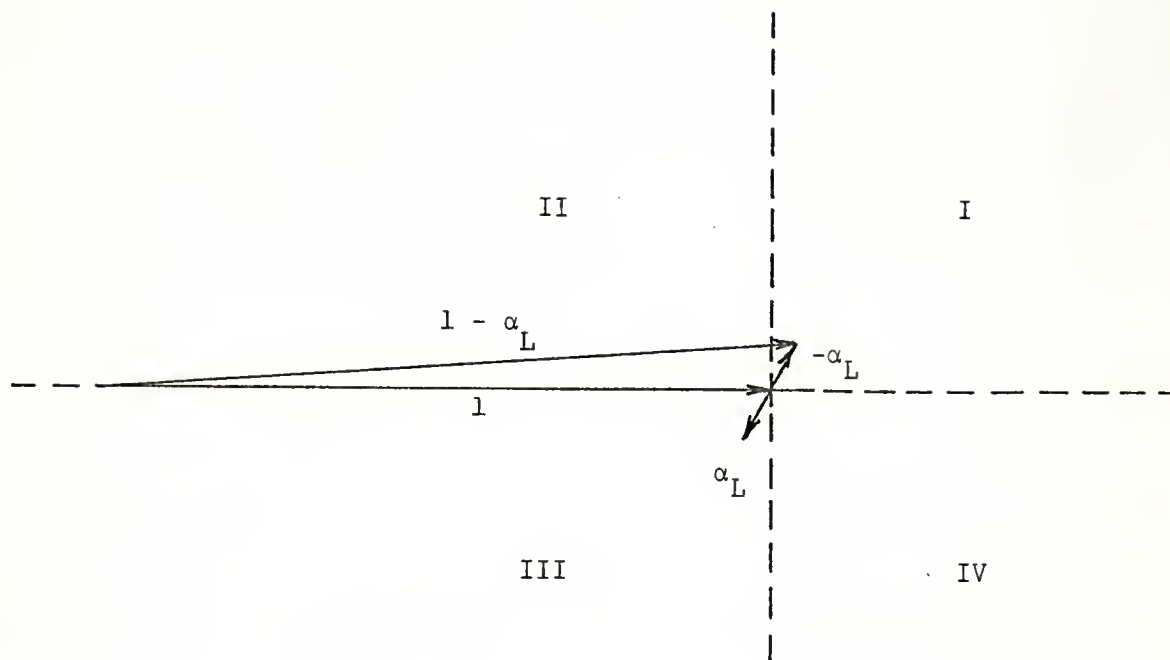


Figure 3.4. Phasor Relations of α_L in the Complex Plane

TABLE 3.1

SIGN OF MAGNITUDE AND PHASE ERRORS IN \hat{m}_{11} *

Quadrant of α_L --	I	II	III	IV
M	+	-	-	+
Φ	+	+	-	-

*More precisely, the sign of M changes when the angle of α_L passes through

$$\pm \left[90 - \frac{1}{2} \cos^{-1} \left(1 - \frac{1}{2} |\alpha_L|^2 \right) \right] \text{ degrees,}$$

which for $|\alpha_L| < 0.05$ is within 2.1 degrees of the quadrature axis.

$$\phi \approx \pm 57.3 |\alpha_L| \text{ degrees} \quad (3.21)$$

with approximately $\frac{|\alpha_L|^2}{2}$ relative magnitude error.

In the computations that follow, $|\alpha_L|$ will be limited to less than 0.05, corresponding to magnitude and phase errors within ± 5 percent and ± 2.9 degrees of zero, respectively. In practice (e.g., when measuring very low frequency dispersion phenomena) a smaller limit for $|\alpha_L|$ may be necessary. In that case, it is a simple matter to modify all of the results by the appropriate constant factor.

Low frequency errors

If reasonable care is taken in the construction and maintenance of the connecting system, low frequency errors do not become significant until the low frequency approximations of the m parameters indicated in connection with Equation (2.22) become valid. At low frequencies, the Y coefficients will normally be pure conductances. Making the appropriate substitutions in Equations (3.13), (3.14), and (3.15), and denoting Y by G for conductance, the low frequency relative loading errors become

$$\alpha_{Q1} \approx - [(Z_{Q1} + Z_{Q2})G_Q + Z_{Q1}G_3 + Z_{Q1}G_1] \quad (3.22)$$

$$\alpha_{P1} \approx \frac{-Z_{P1}}{h_{11}} [Z_{Q2}G_4 - Z_{Q1}G_1 + h_{11}G_P] \quad (3.23)$$

$$\alpha_{P2} \approx \frac{Z_{P2}}{h_{11}} [Z_{Q2}G_2 - Z_{Q1}G_3 - h_{11}G_P] \quad (3.24)$$

Since the effective interface impedances are generally much larger than h_{11} , α_{Q1} will ordinarily be negligible compared to α_{P1} and α_{P2} . For the same reason, the terms including G_P are likely to be negligible also.

When the angle of h_{11} is small, the phase angle of α_L is given approximately by the sum of the angles of two interface impedances plus 0 or 180 degrees, depending on the final sign of the result. For example, for the phase angles given in Table 2.2, the angle of α_L may fall in the first or third quadrant. In this case, the magnitude and phase errors are both positive or both negative as shown in Table 3.1, respectively.

If electrolytic residue contaminates the connecting system, metal-electrolyte interfaces may form at the signal conductor surfaces and act in series with the residue mass. In this case, the Y coefficients may be primarily conductive, or they may include large susceptible components. The outcome depends on the relative importance of the effective impedances of the residue mass and the interfaces formed. Clearly, unless these impedances are quite high, the analysis of small errors developed here is not valid.

If the expressions for α_{Q1} , α_{P1} and α_{P2} are combined, it is evident that the total relative error, α_L , comprises six terms, each multiplied by a different G coefficient. Since the G coefficients are independent finite parameters of the physical system (see Figure 3.3), it is desirable to determine what constraints they should satisfy to assure a certain level of experimental accuracy. The simplest approach is to place a suitable upper limit on the magnitude of each of the six terms in α_L . Since these terms possess different algebraic signs and

phase angles, the resulting upper limit on $|\alpha_L|$ can only be estimated in the general case. The terms including G_Q , G_P , G_3 , and G_4 carry negative signs, while those of G_1 and G_2 carry positive signs. Further, the G_3 and G_4 terms tend to cancel the G_1 and G_2 terms; and the terms including G_Q and G_P are usually much smaller than the others. Accordingly, the upper limit for $|\alpha_L|$ may be determined by setting the terms of G_3 and G_4 (or G_1 and G_2) at their upper limits and neglecting the remaining terms. If, for example, the magnitude of each of the six terms in α_L is limited to less than 0.025, then $|\alpha_L|$ may be assumed to be less than 0.05.

Combining Equations (3.22), (3.23) and (3.24) and applying the 0.025 limit as described yields the following requirements for the G coefficients:

$$G_Q^{-1} > 40 |Z_{Q1} + Z_{Q2}| \quad (3.25)$$

$$G_4^{-1} > 40 \left| \frac{Z_{P1} Z_{Q2}}{h_{11}} \right| \quad (3.26)$$

$$G_2^{-1} > 40 \left| \frac{Z_{P2} Z_{Q2}}{h_{11}} \right| \quad (3.27)$$

$$G_3^{-1} > 40 \left| \frac{Z_{P2} Z_{Q1}}{h_{11}} \right| \quad (3.28)$$

$$G_1^{-1} > 40 \left| \frac{Z_{P1} Z_{Q1}}{h_{11}} \right| \quad (3.29)$$

$$G_P^{-1} > 40 |Z_{P1} + Z_{P2}| \quad (3.30)$$

where the reciprocals are used in order to express the results in familiar ohmic dimensions. Table 3.2 illustrates the requirements on the G coefficients at a frequency of 3 Hz for the numerical examples at the end of Chapter 2.

TABLE 3.2
LIMITS OF CLASS 1, 2, AND 3 CONDUCTANCE FOR THE EXAMPLES OF
CHAPTER 2

		Example 1	Example 2	
G_Q^{-1}	>	130 M	64 M	
G_4^{-1}	>	$2.2 \cdot 10^{12}$	$2.6 \cdot 10^9$	
G_2^{-1}	>	$2.2 \cdot 10^{12}$	$2.6 \cdot 10^9$	
G_3^{-1}	>	$2.2 \cdot 10^{12}$	$4.4 \cdot 10^{12}$	ohms at 3 Hz
G_1^{-1}	>	$2.2 \cdot 10^{12}$	$4.4 \cdot 10^{12}$	
G_P^{-1}	>	130 M	130 M	

High frequency errors

Although, in the limit, the interface impedances become negligible with frequency, this condition may not occur before the error due

to parasitic capacitance in the Y coefficients exceeds permissible limits. Thus, in the analysis that follows, both components of the m parameters are included and the Y coefficients are represented by $e^{j90}S$, where S is the susceptance (magnitude) and e^{j90} is the 90-degree phase factor indicating pure capacitance. The high frequency relative loading errors are

$$\begin{aligned} \alpha_{Q1} = & -e^{j90} [(Z_{Q1} + h_{31} + h_{11} + Z_{Q2} + h_{23})S_Q \\ & + (Z_{Q1} + h_{31} + h_{11})S_3 + (Z_{Q1} + h_{31})S_1] \end{aligned} \quad (3.31)$$

$$\begin{aligned} \alpha_{P1} = & -e^{j90} \frac{Z_{P1} + h_{12}}{h_{11}} [(h_{11} + Z_{Q2} + h_{23})S_4 \\ & - (Z_{Q1} + h_{31})S_1 + h_{11}S_P] \end{aligned} \quad (3.32)$$

$$\begin{aligned} \alpha_{P2} = & e^{j90} \frac{Z_{P2} + h_{13}}{h_{11}} [(Z_{Q2} + h_{23})S_2 - (Z_{Q1} + h_{31} + h_{11})S_3 \\ & - h_{11}S_P] \end{aligned} \quad (3.33)$$

In addition to the e^{j90} factor, the phase angle of the total error is clearly a function of the phase angles in the interface impedance modified by the h parameters. One is led to the conclusion that α_L may fall in any quadrant of the complex plane, depending on the strengths of the various factors.

The combination of Equations (3.31), (3.32) and (3.33) to form

α_L produces six terms, each containing a different S coefficient. These terms are completely analogous to those of the G coefficients studied earlier and may be treated in the same manner. At high frequencies, the terms of S_Q and S_P are more significant than were their low frequency counterparts, but they may still be assumed to be smaller than the other high frequency terms. Hence the 0.025 limit is applied again to each term and $|\alpha_L|$ is reasoned to be less than 0.05. Accordingly, the requirements for the S coefficients are

$$S_Q^{-1} > 40 |Z_{Q1} + h_{31} + h_{11} + Z_{Q2} + h_{23}| \quad (3.34)$$

$$S_4^{-1} > 40 \left| Z_{P1} + h_{12} \right| \left| 1 + \frac{Z_{Q2} + h_{23}}{h_{11}} \right| \quad (3.35)$$

$$S_2^{-1} > 40 \left| Z_{P2} + h_{13} \right| \left| \frac{Z_{Q2} + h_{23}}{h_{11}} \right| \quad (3.36)$$

$$S_3^{-1} > 40 \left| Z_{P2} + h_{13} + h_{11} \right| \left| 1 + \frac{Z_{Q1} + h_{31}}{h_{11}} \right| \quad (3.37)$$

$$S_1^{-1} > 40 \left| Z_{P1} + h_{12} - h_{11} \right| \left| \frac{Z_{Q1} + h_{31}}{h_{11}} \right| \quad (3.38)$$

$$S_P^{-1} > 40 \left| Z_{P1} + h_{12} + Z_{P2} + h_{13} \right| \quad (3.39)$$

The results of these relations for the examples in Chapter 2 are summarized in Table 3.3. To show the effect of interface impedance and the importance of the h parameters at high frequencies, the limits were also computed with the interface impedances neglected. The limits are expressed in ohms at 100 kHz in the upper part of the table and in picofarads of capacitance in the lower part, where

$$C = (2\pi \cdot 10^5)^{-1}S \quad (3.40)$$

and $2\pi \cdot 10^5$ is the radian frequency at 100 kHz.

Transverse admittance errors.--Connectors and implanted electrodes are usually supported by means of a potting material such as acrylic or epoxy resin. This support introduces interelectrode capacitances of between 0.5 and 10.0 picofarads. The choice and handling of support materials requires special consideration, especially when limits on the reciprocal interelectrode conductances are above 10^9 ohms.

With respect to the results in Tables 3.2 and 3.3, the limits in Example 1 are precarious for G_4^{-1} , G_2^{-1} , G_3^{-1} , G_1^{-1} , C_4 , C_2 , C_3 and C_1 . In Example 2, the limits are precarious for G_3^{-1} , G_1^{-1} , C_3 and C_1 . These results demonstrate that for more reliable performance at both low and high frequencies, it is advantageous to minimize the current density at the current electrodes. If a larger electrode were used for Q1 in Example 2, all of the G and C limits would have been within convenient range.

Cable and amplifier input admittance errors.--The input circuit

TABLE 3.3

LIMITS OF CLASS 1, 2, AND 3 SUSCEPTANCE AND CAPACITANCE
FOR THE EXAMPLES OF CHAPTER 2*

		Example 1	Example 2	
S_Q^{-1}	>	120k (78k)	60k (40k)	
S_4^{-1}	>	1.8M (800k)	170k (110k)	
S_2^{-1}	>	1.7M (760k)	110k (76k)	ohms at 100 kHz
S_3^{-1}	>	1.8M (840k)	3.4M (1.6M)	
S_1^{-1}	>	1.7M (720k)	3.4M (1.6M)	
S_P^{-1}	>	110k (76k)	110k (76k)	
C_Q	<	13 (20)	26 (39)	
C_4	<	0.90 (1.9)	9.0 (14)	
C_2	<	0.90 (2.0)	14 (20)	
C_3	<	0.85 (1.8)	0.46 (1.0)	picofarads
C_1	<	0.95 (2.2)	0.46 (1.0)	
C_P	<	14 (20)	14 (20)	

*Values in parentheses are obtained by neglecting interface impedance.

of a typical differential amplifier may be represented by three admittance elements, as indicated in Figure 3.5 (Graham, 1965a). Two of the elements,

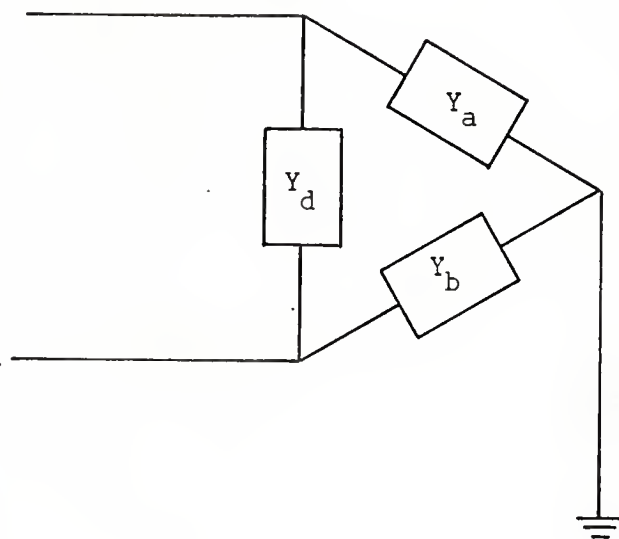


Figure 3.5. Input Circuit of a Differential Amplifier

Y_a and Y_b , are generally equal. In most cases, a foot or more of shielded cable is required to connect the amplifier to the P terminals of the electrode-tissue system. If the two cable conductors are enclosed in a single shield, a component of the cable admittance adds to Y_a , Y_b , and Y_d to form the major part of Y_4 , Y_2 , and Y_p (see Figure 3.3), respectively. If separate shields are used, the cables only contribute to Y_4 and Y_2 .

The results of Tables 3.2 and 3.3 for the elements of Y_4 , Y_2 , and Y_p illustrate requirements on cable and amplifier input admittance parameters. With respect to the amplifier, the limits in Example 2

are not difficult to meet, especially with field effect transistor input stages. In Example 1, the limits on G_4^{-1} and G_2^{-1} are borderline, while those on C_4 and C_2 may be very difficult to satisfy in practice. With respect to the cables, the requirements in Example 1 on C_4 and C_2 are too stringent to meet unless special provision is made to compensate the cable capacitance. One such technique is described in Chapter 5.

Another source of cable admittance is the cable connecting terminal Q1 to the exciting system. It usually constitutes the major part of Y_Q . With reference to Table 3.2, the requirements on G_Q^{-1} are easy to meet. In Table 3.3, however, special care may be necessary to satisfy the requirement on C_Q in Example 1. The Q1 cable is frequently not shielded.

Errors Due to Ground Admittance

Since the error due to ground admittance depends on how the stray ground current is distributed with respect to the main current field, a detailed analysis in the general case is not feasible. However, it is possible to characterize, in a general way, the susceptibility of a system to stray ground current. For that purpose, assume that all of the ground admittance, denoted as Y_g in Figure 3.2, is concentrated at a point of maximum voltage magnitude in the tissue mass. For this extreme condition, the voltage and current are indicated by V_{gmax} and I_{gmax} , respectively, and may be expressed in the following manner

$$\frac{|I_{gmax}|}{|I_{Q1}|} = F_g |Y_g| \quad (3.41)$$

where

$$F_g \equiv \frac{|V_{gmax}|}{|I_{Q1}|} \quad (3.42)$$

If the loading errors are small, F_g is primarily a function of electrode-tissue system parameters (as shown in the next paragraph) and may be viewed as a figure of merit for the system. The larger F_g is, the greater is the ratio of stray ground current to exciting current for a given Y_g , and the greater is the chance for error.

The maximum voltage in the tissue mass corresponds to points adjacent to the $Q1$ electrode and is given by

$$V_{gmax} = V_Q - Z_{Q1}I_{Q1} \quad (3.43)$$

If V_Q is eliminated by means of Equation (3.9), the expression for V_{gmax} becomes

$$V_{gmax} \approx (m_{31} + m_{23} + m_{11} - Z_{Q1})I_{Q1} \quad (3.44)$$

which is valid when the loading error in V_Q is small. Substituting Equation (3.44) into Equation (3.42) and replacing the m parameters by their constituents from Equation (2.22) yields

$$F_g \approx |h_{31} + h_{11} + Z_{Q2} + h_{23}| \quad (3.45)$$

Let the relative loading error in V_p due to ground admittance

be designated by α_g (analogous to α_{Q1} , α_{P1} , and α_{P2}). Then, α_g may be included in α_L and Equations (3.17) through (3.21) may be applied to determine the corresponding magnitude and phase errors in m_{11} . It is not difficult to see that $|\alpha_g|$ will be maximum when all of the ground admittance is concentrated at the point where V_{gmax} occurs. For this condition, $|\alpha_g|$ is approximately equal to the current ratio given in Equation (3.41). To illustrate requirements for Y_g , assume $|\alpha_g|$ is not to exceed 0.01. Then from Equation (3.41), the condition on Y_g becomes

$$|Y_g^{-1}| > 100F_g \quad (3.46)$$

Table 3.4 summarizes the results of Equation (3.46) at 3Hz and 100 kHz for the examples of Chapter 2. As before, the symbols G, S, and C are used to indicate conductance, susceptance, and capacitance, respectively.

TABLE 3.4

LIMITS OF GROUND ADMITTANCE FOR THE EXAMPLES OF CHAPTER 2*

		Example 1	Example 2	
G_g^{-1}	>	160M (200k)	160k (100k)	ohms at 3 Hz
S_g^{-1}	>	230k (200k)	100k (100k)	ohms at 100 kHz
C_g	<	6.8 (7.8)	16 (16)	picofarads

*Values in parentheses are obtained by neglecting interface impedance.

Since the extreme conditions assumed in deriving the tabulated results are not likely to occur in practice, the values shown are probably more severe than necessary. However, even allowing for one or two orders of magnitude, the requirements in Example 1 may be inconvenient to satisfy under certain experimental conditions (e.g., during surgical procedures).

Common Mode Rejection Error

If the differential amplifier of Figure 3.5 is connected to the test system of Figure 3.2, the common mode signal to the amplifier is V_2 . The effective differential input signal is given by

$$V_{P\rho} = V_P (1 + \alpha_\rho) \quad (3.47)$$

where

$$\alpha_\rho \equiv \frac{V_2}{\rho V_P} \quad (3.48)$$

and ρ is the common mode rejection ratio of the amplifier.

The second experimental estimation of m_{11} is defined as $\hat{\hat{m}}_{11}$ and includes both loading and common mode rejection error. It is given by

$$\hat{\hat{m}}_{11} \equiv \frac{V_{P\rho}}{I_Q} \quad (3.49)$$

which, using Equations (3.47) and (3.16), becomes

$$\hat{\hat{m}}_{11} = \hat{m}_{11} (1 + \alpha_p) \quad (3.50)$$

Magnitude and phase errors.--The relative error in the magnitude of $\hat{\hat{m}}_{11}$ as an estimate of \hat{m}_{11} is

$$M = |1 + \alpha_p| - 1 \quad (3.51)$$

and the phase error is

$$\phi = \angle(1 + \alpha_p) \quad (3.52)$$

For a given $|\alpha_p|$ the relative magnitude error becomes maximum when the angle of α_p is 0 or 180 degrees, and the phase error becomes maximum when the angle of α_p is $\pm(90 + \sin^{-1}|\alpha_p|)$ degrees. For small $|\alpha_p|$, the maximum errors may be written

$$M \approx \pm |\alpha_p| \quad (3.53)$$

with zero phase error, and

$$\phi \approx \pm 57.3 |\alpha_p| \text{ degrees} \quad (3.54)$$

with approximately $\frac{|\alpha_p|^2}{2}$ relative magnitude error. These expressions are analogous to those found for α_L . Since the common mode rejection

ratio is somewhat more controllable than the loading admittance parameters, it is reasonable to place a more severe limit on $|\alpha_p|$. For the computations to follow, $|\alpha_p|$ will be limited to less than 0.01, corresponding to magnitude and phase errors within ± 1 percent and ± 0.6 degrees of zero, respectively.

From Equation (2.1)

$$\frac{V_2}{V_P} = \frac{V_Q}{V_P} - \frac{V_1}{V_P} - 1 \quad (3.55)$$

which with the small error approximation of Equations (3.11) and (3.12) becomes

$$\frac{V_2}{V_P} \approx \frac{m_{23}}{m_{11}} \quad (3.56)$$

Substituting Equation (3.56) into Equation (3.48) and replacing m_{23} by its constituents from Equation (2.22) yields

$$\alpha_p \approx \frac{Z_{Q2} + h_{23}}{\rho h_{11}} \quad (3.57)$$

If $|\alpha_p|$ is required to be less than 0.01, then ρ must satisfy the following inequality

$$|\rho| > 100 \left| \frac{Z_{Q2} + h_{23}}{h_{11}} \right| \quad (3.58)$$

Table 3.5 summarizes the results of Equation (3.58) for the examples in Chapter 2.

TABLE 3.5

MINIMUM VALUES OF COMMON MODE REJECTION RATIO FOR THE
EXAMPLES OF CHAPTER 2*

Frequency	Example 1	Example 2
3 Hz	3.4M (2.0k)	4.2k (200)
100 kHz	3.0k (2.0k)	200 (200)

*Values in parentheses are obtained by neglecting interface impedance.

The requirements for Example 1 in Table 3.5 would be extremely difficult to satisfy in practice. Low noise broad band differential amplifiers with high common mode rejection ratios and high input impedances are rather difficult to obtain. In addition, special precautions are necessary to realize the potential capabilities of such amplifiers. Some units are supplied with high impedance probes which usually lead to common mode rejection ratios well below that of the amplifier alone.

Current Control Error

Ideally, one would like to establish the applied signal current independently of the properties of the electrode-tissue system and have available a convenient measure of the current as a reference in measuring the voltage response. The simplest approach is to use a

voltage generator in series with a large resistor as indicated in Figure 3.6. If I_Q were determined entirely by E_q (within an arbitrary

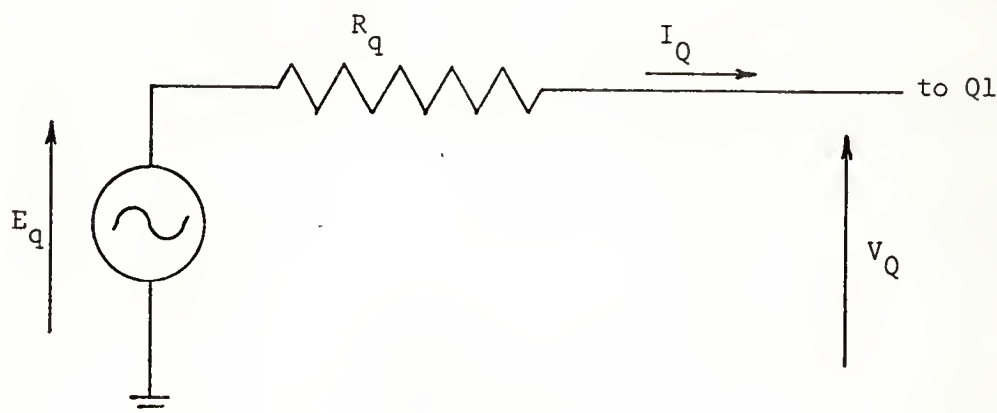


Figure 3.6. Approximation of a Current Source

real constant), then E_q could be used as the reference signal. Furthermore, this condition would permit controlled nonsinusoidal currents to be applied when information is desired at several frequencies simultaneously. The errors of this method are analyzed in the following paragraphs. The results are used again in Chapters 4 and 5 to evaluate the new techniques presented there.

In a physical system, parasitic capacitance will generally reduce the effective value of R_q and produce phase shift at the high frequencies. To account approximately for this effect in the present analysis, let the resistor value be multiplied by the factor $(1 + jf/f_0)^{-1}$. This form results if the parasitic capacitance is assumed to act entirely in parallel with R_q . Assume that E_q serves

as the reference signal for measuring the voltage response, V_p , of the electrode-tissue system. Then the experimental estimation of I_Q is defined by

$$\hat{I}_Q \equiv \frac{E_q}{R_q} \quad (3.59)$$

This expression may also be written

$$\hat{I}_Q = I_Q \left(\frac{1}{1+jf/f_o} + \alpha_Q \right) \quad (3.60)$$

where

$$\alpha_Q \equiv \frac{V_Q/I_Q}{R_Q} \quad (3.61)$$

The third experimental estimation of m_{11} , which includes loading, common mode rejection, and current control error, is defined by

$$\hat{\hat{m}}_{11} \equiv \frac{V_{Pp}}{\hat{I}_Q} \quad (3.62)$$

where V_{Pp} is as defined in Equation (3.47). Using Equations (3.60) and (3.49), Equation (3.62) may be written

$$\hat{\hat{m}}_{11} = \frac{\hat{m}_{11}}{\frac{1}{1+jf/f_o} + \alpha_Q} \quad (3.63)$$

It is clear that the current control error arises from the two terms in the denominator of Equation (3.63). As shown in the following sections, low frequency errors are determined by α_Q , while high frequency errors are determined by the parasitic capacitance term.

Low frequency errors

For small loading errors,

$$I_Q \approx I_{Q1} \quad (3.64)$$

and from Equation (3.9)

$$\frac{V_Q}{I_{Q1}} \approx m_{31} + m_{23} + m_{11} \quad (3.65)$$

Substituting Equations (3.64) and (3.65) into Equation (3.61) and replacing the m parameters by their constituents from Equation (2.22) yields

$$\alpha_Q \approx \frac{Z_{Q1} + h_{31} + h_{11} + Z_{Q2} + h_{23}}{R_Q} \quad (3.66)$$

At low frequencies, the effective interface impedances predominate and drive the angle of α_Q well into the fourth quadrant of the complex plane. As the frequency increases, $|\alpha_Q|$ decreases and the angle of α_Q moves toward zero.

Since the ratio f/f_o in Equation (3.63) is generally negligible

at frequencies below 10 kHz, the low frequency relative error in the magnitude of $\hat{\hat{m}}_{11}$ as an estimate of \hat{m}_{11} is

$$M = \frac{1}{|1 + \alpha_Q|} - 1 \quad (3.67)$$

and the phase error is

$$\phi = - \angle(1 + \alpha_Q) \quad (3.68)$$

The vector, $1 + \alpha_Q$, is indicated in Figure 3.7.

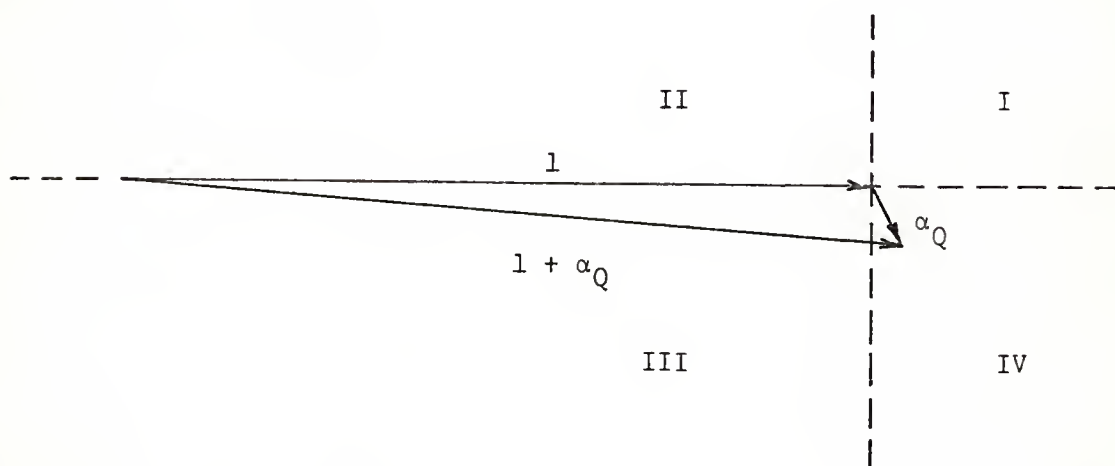


Figure 3.7. Phasor Relations of α_Q in the Complex Plane

It is evident that M is negative and ϕ is positive.

If $|\alpha_Q|$ is limited to less than 0.01, then from Equation (3.66), R_Q must satisfy the following inequality

$$R_q > 100 |Z_{Q1} + h_{31} + h_{11} + Z_{Q2} + h_{23}| \quad (3.69)$$

The limits for the examples in Chapter 2 are summarized in Table 3.6, where the 100 kHz calculation is included for comparison.

TABLE 3.6

MINIMUM VALUES OF CURRENT SOURCE RESISTANCE*
FOR THE EXAMPLES OF CHAPTER 2

Frequency	Example 1	Example 2	
3 Hz	320M (200k)	160M (100k)	
100 kHz	290k (200k)	150k (100k)	ohms

*Values in parentheses are obtained by neglecting interface impedance.

High frequency errors

At high frequencies, α_Q generally becomes negligible, so that Equation (3.63) may be written

$$\hat{\hat{m}}_{11} = \hat{m}_{11} (1 + jf/f_o) \quad (3.70)$$

It is evident that parasitic capacitance across the source resistor causes positive magnitude and phase errors at high frequencies. The 3 d.b. frequency, f_o , may be expected to vary more or less inversely with the resistance value so that the larger R_q must be to satisfy the limit on α_Q , the worse the frequency response becomes. For example, a 1 megohm carbon resistor might have an f_o at about 200 kHz. To

avoid a phase error greater than 6 degrees, the frequencies for impedance measurements would have to be less than $0.1 f_o$, or 20 kHz in this example. For the values in Table 3.6, the useful frequency range is proportionately smaller.

To conclude the analysis of loading, common mode rejection, and current control error, it is instructive to consider all three error factors explicitly in one expression. Thus, combining Equations (3.17), (3.50) and (3.63), the third estimation of m_{11} may be written

$$\hat{\hat{m}}_{11} = m_{11}(1 + jf/f_o) \frac{(1 + \alpha_o)}{(1 - \alpha_L)(1 + \alpha_Q[1 + jf/f_o])} \quad (3.71)$$

Equation (3.71) may be simplified if the denominator factors are replaced by equivalent series expansions in the numerator. Then, if each α is assumed to be small (e.g., less than 0.05), the factors in the numerator may be multiplied together, and the resulting second order terms may be neglected. This procedure leads to the following approximate expression for the third estimation of m_{11} :

$$\hat{\hat{m}}_{11} \approx m_{11}(1 + jf/f_o)(1 + \alpha_o + \alpha_L - \alpha_Q[1 + jf/f_o]) \quad (3.72)$$

The most uncertain factor in Equation (3.72) will generally be α_L . This follows from the fact that transverse and ground admittance components are easily influenced by indeterminate properties of the experimental environment. In contrast, common mode rejection and current control capabilities are relatively definite characteristics

of the instrumentation system which can be evaluated for a given electrode-tissue system. The effect of the frequency factor multiplying m_{11} can usually be eliminated by introducing suitable compensation at the input signal generator, or, more conveniently, in the gain of the response amplifier. The frequency factor multiplying α_Q cannot be eliminated and its importance depends on α_Q .

For convenience, assume the frequency factor multiplying m_{11} has been compensated and the frequency factor multiplying α_Q is included with α_Q . The total relative error is then given approximately by the algebraic sum of the three α terms, which may be reduced to magnitude and phase error in a manner similar to that for α_p in Equations (3.50) and (3.54). The relative importance of the α terms depends on the properties of the instrumentation system and the electrode-tissue system used. Each case may be evaluated in the light of the analyses presented in this and succeeding chapters.

Noise in the Classical System

A detailed analysis of the noise problem is beyond the scope of the present work. This section gives a brief account of the major types of noise found in biological impedance measurements. It also serves as a basis for the noise analysis presented in Chapter 4.

In linear studies of tissue impedance, the response voltage is normally much less than one millivolt and frequently less than one hundred microvolts, in amplitude. Noise, which may be significant at these levels, originates in the instrumentation system, in the external environment, and in the electrode-tissue system itself. These

classes of noise are considered in the following sections with the aid of Figure 3.8.

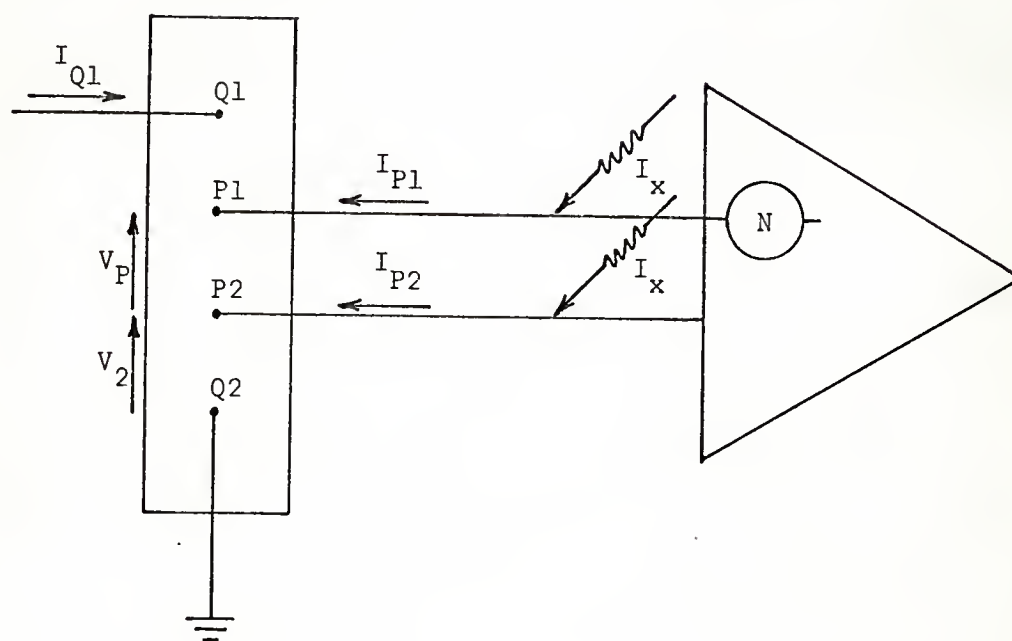


Figure 3.8. Noise Sources in the Classical Method.

Instrumentation Noise

Instrumentation noise consists primarily of shot and/or thermal noise which originates in the active and passive components of the initial amplifier stages. It may be distinguished from other noise by its broad bandwidth (limited primarily by the method of observation) and by its more limited and consistent range of amplitude. Part of the noise may be described by means of noise current sources connected between the amplifier input terminals and from each input to ground (not shown in Figure 3.8). The rest may be described by

means of a noise voltage source in series with the input terminals (N in Figure 3.8). Since most of the noise energy occurs at frequencies above 10 kHz, where the terminal impedances of the electrode-tissue system are not especially large, the noise current sources are usually less significant than the noise voltage source. For bandwidths up to 1 MHz, the equivalent input noise of most amplifiers is less than 30 microvolts peak-to-peak (as observed on an oscilloscope trace).

Environmental Noise

Noise originating in the external environment enters the system by means of electrostatic and/or electromagnetic coupling. The system is most sensitive to this noise at the cables of P1 and P2, where the impedance level is high, the signal level is low, and the exposure is relatively great. Environmental noise may also enter throughout the volume of the impedance subject and by means of the Q1 cable. The discussion that follows is concerned only with the P1 and P2 cables.

In addition to shielding the cables, electrostatic noise may be reduced by arranging them symmetrically with respect to possible noise sources, which takes advantage of the differential nature of the amplifier. To reduce electromagnetic coupling, the loop area between cables should be kept to a minimum. Both objectives may be achieved by twisting the cables together. Electrostatic noise also depends on the impedance levels in the electrode-tissue system and since it usually is a more prevalent problem, an analysis follows.

Electrostatically coupled noise may be described by means of noise currents feeding the P1 and P2 cables. For simplicity, assume

the currents are equal as indicated by I_x in Figure 3.8. If V_{Px} and V_{2x} designate the differential and common mode voltages created by I_x , then the effective differential noise voltage is

$$V_{Px\rho} = V_{Px} + \frac{V_{2x}}{\rho} \quad (3.73)$$

where ρ is the common mode rejection ratio of the differential amplifier.

Since the external circuit impedances to ground at P1 and P2 are quite high, the noise components of I_{P1} and I_{P2} are essentially I_x . Using this value in Equation (2.3) yields for the noise component of V_P

$$V_{Px} = I_x(m_{12} - m_{13}) \quad (3.74)$$

The noise component of V_2 may be written according to Equation (2.1) as

$$V_{2x} = V_{Qx} - V_{1x} - V_{Px} \quad (3.75)$$

If V_{Qx} , V_{1x} , and V_{Px} are replaced according to Equation (2.3), and the dependent parameters, m_{22} and m_{32} , are eliminated by means of Equations (2.4) and (2.5), the expression for V_{2x} becomes

$$V_{2x} = I_x(m_{13} + 2m_{23} + 2m_{33}) \quad (3.76)$$

Substituting Equations (3.74) and (3.76) into Equation (3.73)

and replacing the m parameters by their constituents from Equation (2.22), the effective differential noise voltage may be written

$$\frac{V_{Pxp}}{V_P} = \frac{I_x}{I_{Q1}} \left[\frac{Z_{P1} - Z_{P2} + h_{12} - h_{13}}{h_{11}} + \frac{Z_{P2} + 2Z_{Q2} + h_{13} + 2h_{23} + 2h_{33}}{\rho h_{11}} \right] \quad (3.77)$$

where the expression is divided by V_P (as given in Equation (3.8)) to obtain the noise in relative terms. Note that I_{Q1} is the nominal exciting current and V_P is the nominal voltage response. As a rule, the cancellation occurring in the numerator of the left term in the brackets is neither complete nor easily controlled (even in symmetrical systems) and cannot be used as a reliable index of noise reduction. This statement is especially true at noise frequencies where the interface impedances are large. The right term in the brackets is not likely to be important unless ρ is abnormally small.

It is instructive to determine the requirement on the signal-to-noise current ratio to meet a given limit on the signal-to-noise voltage ratio in the response. Assume that $|V_P|$ is required to be greater than $10|V_{Pxp}|$. Then according to Equation (3.77), the currents must satisfy the following inequality:

$$\frac{|I_{Q1}|}{|I_x|} > 10 \left[\frac{Z_{P1} - Z_{P2} + h_{12} - h_{13}}{h_{11}} + \frac{Z_{P2} + 2Z_{Q2} + h_{13} + 2h_{23} + 2h_{33}}{\rho h_{11}} \right] \quad (3.78)$$

Since an upper limit is placed on I_{Q1} by the requirements of linearity and passivity in the tissue to be measured, the inequality can not be satisfied by increasing I_{Q1} indefinitely. Thus, special precautions are often necessary to minimize I_x . The greatest problem is usually presented by sixty-cycle power lines and equipment. In many situations, Equation (3.78) cannot be satisfied for this type of noise, unless the potential cables are shielded to reduce I_x .

Electrode-Tissue Noise

Noise of the electrode-tissue system originates independently in the tissue mass and at each of the electrode-tissue interfaces. These two classes of noise are explained in the following paragraphs.

Tissue noise.--Noise potentials reflect the spontaneous and induced electrochemical activity of living cells. It is well known that potentials of myogenic and/or nervous origin occur in most body tissues and differ in form and amplitude from place to place. In the brain, for example, these potentials, called the electrocortigram, may make impedance measurements especially difficult. The electrocortigram appears as a random, rhythmic, relatively continuous activity, which changes in character and amplitude with the physiological state of the individual. Maximum peak amplitudes generally range from 100 to 150 microvolts. Most of the energy in the electrocortigram lies in the low frequency band between 1 and 30 Hz.

Interface noise.--Noise potentials also arise from the spontaneous electrochemical activity of the metal-electrolyte interface

and include d.c. and a.c. components (Flasterstein, 1966a, b). In theory, thermodynamics predicts the occurrence of a d.c. equilibrium potential between the metal and the electrolyte. In practice, a number of factors relating to the inherent inhomogeneity of the interface prevent the attainment of a true equilibrium. Consequently, the d.c. level is unstable and varies randomly in time. The d.c. potential of two apparently identical electrodes in electrolyte may differ by more than several tenths of a volt with variations (positive and negative) of the same order. Superimposed on this slow noise, there often occur faster a.c. and pulse potentials with frequency components in the electrocortigram spectrum. The peak amplitude of the a.c. and pulse potentials may reach several hundred microvolts.

It is evident from Figure 3.8 that each input of the differential amplifier receives noise from the Q2 interface and the corresponding P interface in addition to noise generated in the tissue mass. The differential signal includes the noise of both P interfaces. To prevent the instrumentation system (amplifiers and/or other equipment) from being overdriven, d.c. imbalances and slow fluctuations should be rejected in the early stages of amplification. For example, a system with any member set to near-full range for signals on the order of 100 microvolts, would have to reject 99 percent or more of the noise to assure reliable operation. A versatile system should be able to handle signals down to 0.1 Hz and have the option of d.c. coupling. To achieve these aims, without degrading amplifier performance, is likely to prove difficult because of the large filter components required. One may also object to the inconvenience of making modifications inside the amplifier.

When the impedance information of interest occurs at frequencies well above the spectrum of electrode-tissue noise, a low frequency filter usually suffices to establish an adequate signal-to-noise ratio before application to the measuring instruments. If signal frequencies overlap the noise spectrum, then special averaging techniques may be necessary to improve the signal-to-noise ratio. These techniques make use of the random character of the noise and the deterministic nature of the signal, and usually require extended observation times.

CHAPTER 4

THE VIRTUAL-GROUND CONFIGURATION

Introduction

The analysis of the classical method in Chapter 3 shows that to achieve a given experimental accuracy, the common mode rejection ratio, the loading admittance and the current source resistance must satisfy requirements that depend on the parameters of the electrode-tissue system. For small electrode systems (for example in animal experiments in vivo) these requirements are often too severe to satisfy in practice. This statement is illustrated by the numerical results in Chapter 3 for the examples of Chapter 2. Another problem which lacks a convenient solution in the classical method is presented by electrode-tissue noise.

In the virtual-ground configuration, described in this chapter, the parameters of the electrode-tissue system continue to influence the experimental accuracy. However, the requirements on instrumentation parameters are much easier to meet than in the classical method. The proposed system also provides a convenient means of controlling the effect of electrode-tissue noise.

The basic connections of the virtual-ground configuration are illustrated in Figure 4.1. A high gain inverting amplifier is shown connected between electrodes P2 and Q2 of the electrode-tissue system.

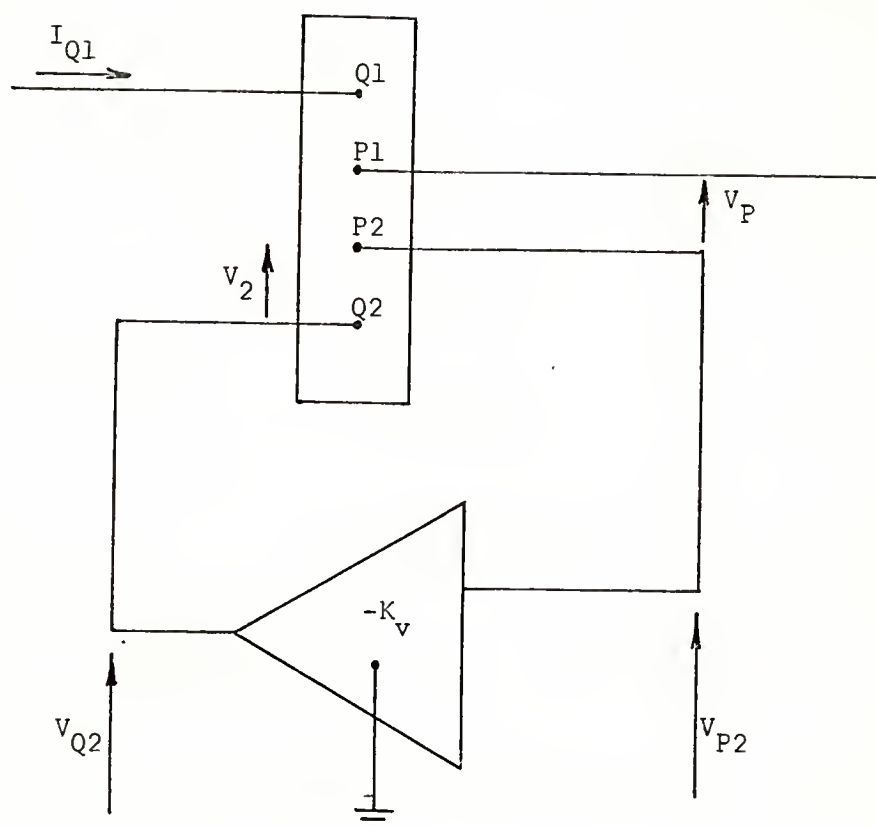


Figure 4.1. Basic Connections of the Virtual-Ground Configuration

The signal current is injected at Q1 and flows through the tissue to Q2, where it returns to ground via the output stage of the amplifier. Since the gain is high, V_{P2} is much smaller than V_{Q2} , so that the latter tracks V_2 of the electrode-tissue system (with inverted sign). If the gain is sufficiently high, V_{P2} will also be negligible compared to V_P and the voltage response may be measured between P1 and ground with a single-ended amplifier. Otherwise, the response must be measured differentially between P1 and P2. Both cases are analyzed in this chapter.

The most suitable amplifiers for the virtual-ground connection belong to a class of devices known as operational amplifiers. Nominal open-loop gain and phase shift characteristics for the type of operational amplifier of interest here are sketched in Figure 4.2 (Philbrick, 1966). The figure also shows common ranges for the gain

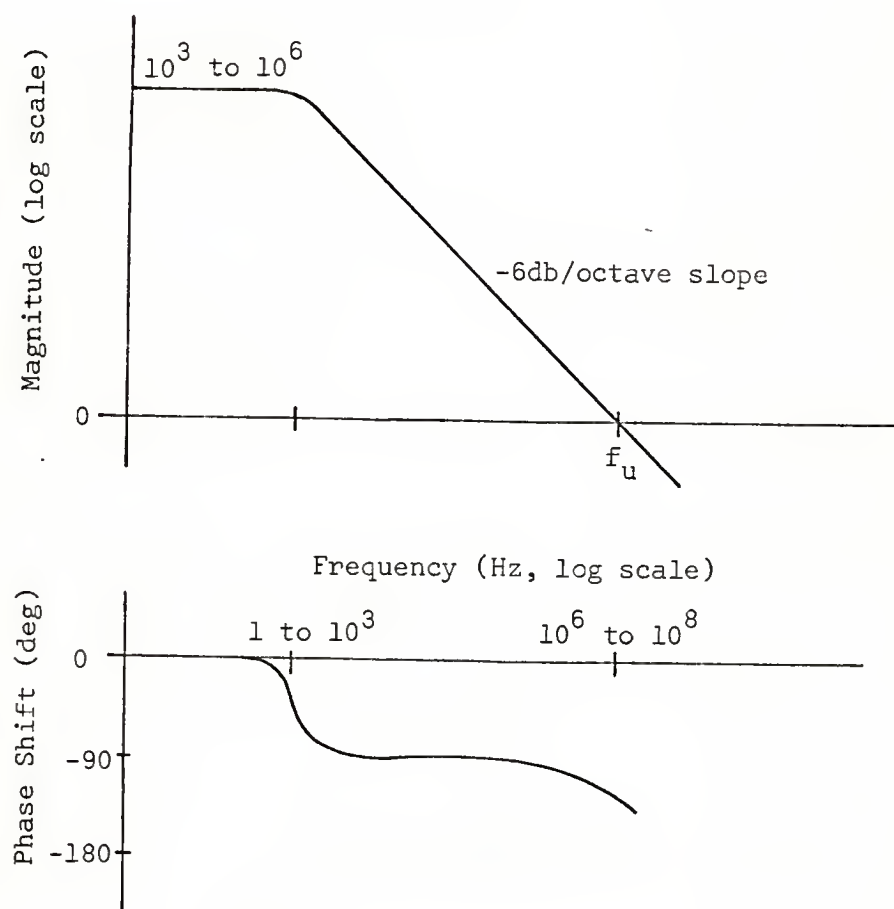


Figure 4.2. Nominal Gain and Phase Shift Characteristics of Operational Amplifiers

magnitude, the break frequency and the unity gain frequency. For an inverting amplifier, an additional 180 degrees must be added to the

phase plot to give the total phase shift from input to output. It is evident that the total internal phase lag of the amplifier does not reach 360 degrees until well beyond the unity gain frequency. This characteristic of operational amplifiers makes it possible to construct stable wideband circuits having tight negative feedback loops. The matter of stability is considered in a later section.

The essential elements for the analysis of the virtual-ground configuration are indicated in Figure 4.3. The noise sources (I_x , N_v , and N_p) are treated in a separate section and should be neglected unless otherwise noted.

Common Mode Rejection Error

Single-Ended Operation

With reference to Figure 4.3, the input signal to the single-ended amplifier at P1 is

$$V_{P1} = V_P(1 + \beta_v) \quad (4.1)$$

where

$$\beta_v \equiv \frac{V_{P2}}{V_P} \quad (4.2)$$

Note that β_v plays the same role here as α_o does in Equation (3.47).

By inspection, from Figure 4.3

$$V_{P2} = V_2 - K_v V_{P2} + Z_o I_{Q2}'' \quad (4.3)$$

where $-K_v$ is the complex open-loop unloaded gain and Z_o is the output impedance of the virtual-ground amplifier. For small loading error

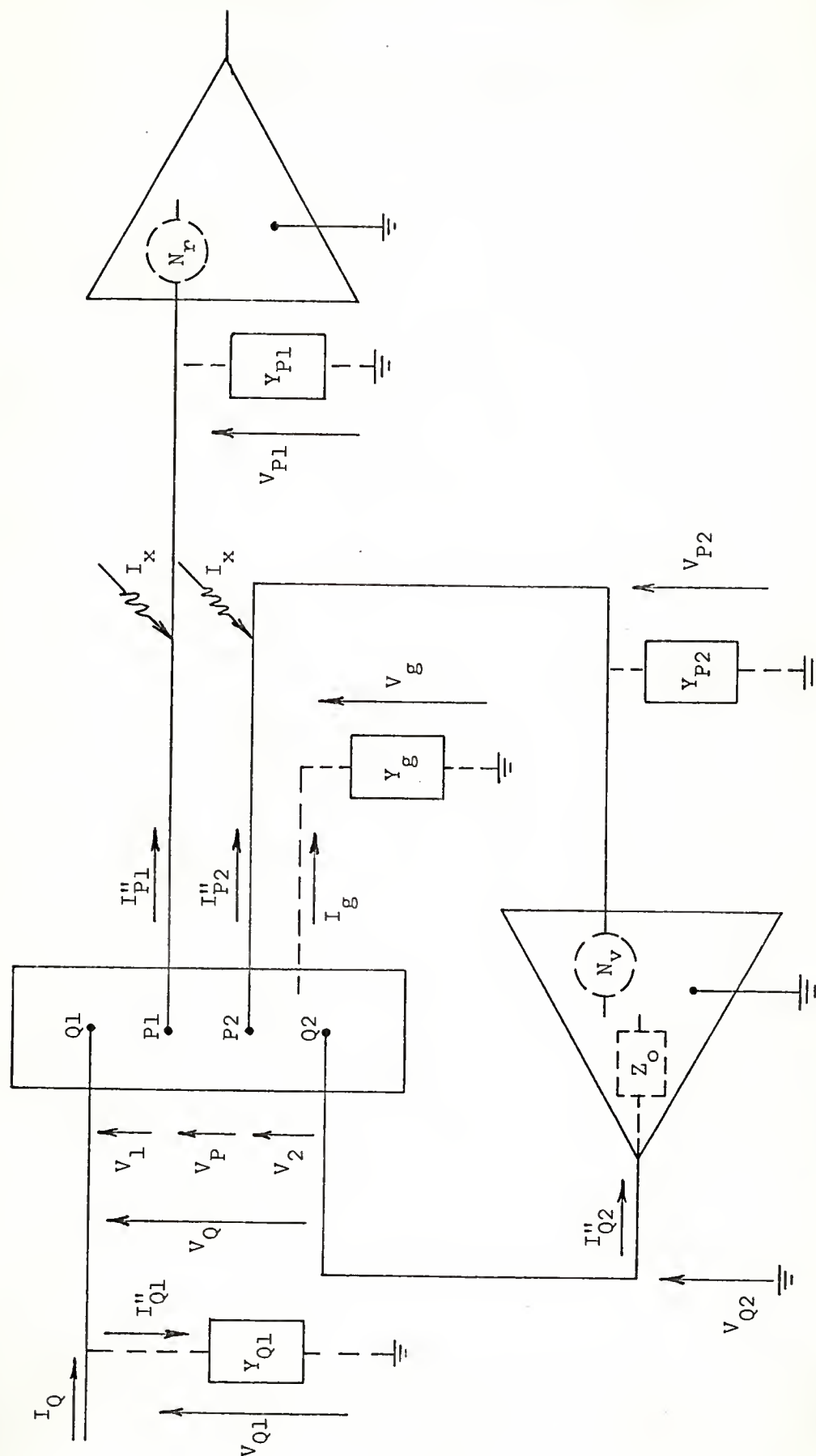


Figure 4.3. Virtual-Ground System Showing Loading Admittances and Noise Sources

$$I_{Q2}'' \approx I_{Q1} \quad (4.4)$$

where I_{Q1} is as defined in Figure 3.2. Combining Equations (4.3) and (4.4), solving for V_{P2} and substituting the result into Equation (4.2) yields

$$\beta_v = \frac{\frac{V_2}{V_P} + \frac{Z_o}{V_P/I_{Q1}}}{1 + K_v} \quad (4.5)$$

Using the small loading error approximations of Equations (3.8) and (3.56), and replacing m_{23} by its constituents from Equation (2.22), Equation (4.5) may be written

$$\beta_v \approx \frac{m_{23} + Z_o}{(1+K_v)m_{11}} = \frac{Z_{Q2}+h_{23}+Z_o}{(1+K_v)h_{11}} \quad (4.6)$$

Note that the factor $(1+K_v)$ plays the same role here as the rejection ratio of the differential amplifier does in Equation (3.57). As a rule, the unity term is negligible in comparison to K_v .

If $|\beta_v|$ is restricted to less than 0.01, then by Equation (4.6), the amplifier must satisfy the following inequality

$$|K_v| > 100 \left| \frac{Z_{Q2}+h_{23}+Z_o}{h_{11}} \right| \quad (4.7)$$

Except for the term Z_o , this relation places the same requirement on $|K_v|$ as was found for $|\rho|$ in Equation (3.58). It is evident that the gain requirement is reduced if Z_o is negligible compared to $Z_{Q2}+h_{23}$. In addition, the smaller Z_o is at high frequencies, the more parasitic capacitance the amplifier can tolerate at its output terminal without

becoming unstable. The results of Table 3.5 are directly applicable to Equation (4.7) if $|\rho|$ is replaced by $|K_v|$ and Z_o is neglected.

The unity gain frequency of wideband operational amplifiers is commonly between 30 MHz and 100 MHz. Since the gain rolls off at about 6 db per octave, it typically falls in the range of 300 to 1000 at 100 kHz. Amplifiers with unity gain frequencies near or exceeding 100 MHz are likely to incur formidable stability problems in the virtual-ground connection and may not be practical for general applications (see section on stability). If 1000 is taken as a practical upper limit on $|K_v|$ at 100 kHz, Equation (4.7) may be rearranged to give

$$\left| \frac{Z_{Q2} + h_{23} + Z_o}{h_{11}} \right| < 10 \quad (4.8)$$

This relation restricts the type of electrode-tissue systems which can be measured by the single-ended method with better than 1 percent accuracy at 100 kHz. With reference to the examples of Chapter 2, only Example 1 exceeds the limit with a parameter ratio of 30.

Differential Operation

When the requirements on $|K_v|$ cannot be met with single-ended operation, a differential amplifier may be employed at P1 and P2. With reference to Figure 4.3, the common mode signal to the differential amplifier would be V_{P2} . The effective differential input signal would be

$$V_{P\rho} = V_P (1 + \beta_\rho) \quad (4.9)$$

where

$$\beta_{\rho} \equiv \frac{V_{P2}}{\rho V_P} \quad (4.10)$$

and ρ is the common mode rejection ratio of the differential amplifier. Note that β_{ρ} plays the same role in Equation (4.9) as β_v does in Equation (4.1) and α_{ρ} does in Equation (3.47). It follows from Equations (4.10) and (4.2) that

$$\beta_{\rho} = \frac{\beta_v}{\rho} \quad (4.11)$$

which, using Equation (4.6), becomes

$$\beta_{\rho} = \frac{Z_{Q2} + h_{23} + Z_o}{\rho(1 + K_v)h_{11}} \quad (4.12)$$

Equation (4.12) is to be compared with Equations (3.57) and (4.6).

Placing the 0.01 limit on $|\beta_{\rho}|$ in Equation (4.12) yields the following requirement on ρ and K_v

$$|\rho K_v| > 100 \left| \frac{Z_{Q2} + h_{23} + Z_o}{h_{11}} \right| \quad (4.13)$$

where the unity term is omitted as justified earlier. This expression is to be compared with Equations (3.58) and (4.7).

The results in Table 3.5 apply directly to Equation (4.13) if $|\rho|$ is replaced by $|\rho K_v|$ and Z_o is neglected. Recall that the classical differential system and the single-ended virtual-ground

system are not satisfactory in the case of Example 1. For the present system, the requirements for Example 1 are easily satisfied with relatively modest amplifiers. As an illustration, consider a virtual-ground amplifier with $|K_v|$ equal to $2 \cdot 10^5$ at 3 Hz and 300 at 100 kHz. Then, $|\rho|$ need only exceed 17 and 10 at the two frequencies, respectively.

Loading Error

The four classes of loading admittance defined in Chapter 3 also occur in the virtual-ground system. With respect to the transverse admittance (class 1) and the component of cable and amplifier input admittance (classes 2 and 3) that may occur between P1 and P2, the loading error analysis of Chapter 3 and the results of Tables 3.2 and 3.3 apply directly. These admittances may be assumed to be included in the four terminal block of Figure 4.3. The remainder of the loading admittances (class 4 and most of classes 2 and 3) is referenced to ground and requires special consideration.

Cable and Amplifier Input Admittance

Cable and amplifier input admittance is indicated by Y_{Q1} , Y_{P1} , and Y_{P2} in Figure 4.3. From the figure, the corresponding loading currents are

$$I''_{Q1} = V_{Q1} Y_{Q1} \quad (4.14)$$

$$I''_{P1} = V_{P1} Y_{P1} \quad (4.15)$$

$$I_{P2}'' = V_{P2} Y_{P2} \quad (4.16)$$

and

$$V_{Q1} = V_1 + V_P + V_{P2} \approx \left(\frac{m_{31}}{m_{11}} + 1 + \beta_v \right) V_P \quad (4.17)$$

where V_1 has been replaced by the small loading error approximation of Equation (3.11) and V_{P2} has been eliminated by means of Equation (4.2).

Using Equations (4.1), (4.2), and (4.17), the expressions for the loading currents may be written

$$I_{Q1}'' \approx \left(\frac{m_{31}}{m_{11}} + 1 + \beta_v \right) V_P Y_{Q1} \quad (4.18)$$

$$I_{P1}'' = (1 + \beta_v) V_P Y_{P1} \quad (4.19)$$

$$I_{P2}'' = \beta_v V_P Y_{P2} \quad (4.20)$$

If I_{Q1}'' , I_{P1}'' , and I_{P2}'' are considered as additions to I_{Q1}' , I_{P1}' , and I_{P2}' in Equation (3.4), respectively, the new relative error terms to be added to α_{Q1} , α_{P1} , and α_{P2} in Equations (3.13), (3.14), and (3.15) are,

$$\beta_{Q1} \equiv \frac{-m_{11} I_{Q1}''}{V_P} \approx -[m_{31} + (1 + \beta_v) m_{11}] Y_{Q1} \quad (4.21)$$

$$\beta_{P1} \equiv \frac{-m_{12} I_{P1}''}{V_P} = -m_{12} (1 + \beta_v) Y_{P1} \quad (4.22)$$

$$\beta_{P2} \equiv \frac{m_{13} I_{P2}''}{V_P} = m_{13} \beta_v Y_{P2} \quad (4.23)$$

respectively. These terms may now be analyzed following the method for the loading errors (i.e., the α) in Chapter 3.

If the magnitudes of β_{Q1} , β_{P1} , and β_{P2} are limited to less than 0.025, then, from Equations (4.21), (4.22), and (4.23), the requirements on the loading admittances become,

$$|Y_{Q1}^{-1}| > 40 |Z_{Q1} + h_{31} + h_{11} + \beta_v h_{11}| \quad (4.24)$$

$$|Y_{P1}^{-1}| > 40 |Z_{P1} + h_{12}| |1 + \beta_v| \quad (4.25)$$

$$|Y_{P2}^{-1}| > 40 |Z_{P2} + h_{13}| |\beta_v| \quad (4.26)$$

where the m parameters have been replaced by their constituents. Note that for single-ended amplification, $|\beta_v|$ is normally negligible compared to unity. With differential amplification, $|\beta_v|$ may not be negligible, but it will almost certainly be less than unity in a well-designed system. Comparing Figure 4.3 with Figure 3.3, it is evident that Y_{Q1} , Y_{P1} , and Y_{F2} correspond to the cable and amplifier components of Y_Q , Y_4 , and Y_2 , respectively. Accordingly, Equations (4.24), (4.25) and (4.26) are to be compared at low frequencies to Equations (3.25), (3.26), and (3.27); and at high frequencies to Equations (3.34), (3.35), and (3.36), respectively.

To illustrate the admittance requirements of Equations (4.24), (4.25) and (4.26) for the examples at the end of Chapter 2, it is

first necessary to determine suitable values for β_v . For this purpose, assume Z_o is negligible and let K_v be $2 \cdot 10^5 e^{-j0}$ at 3 Hz and $300 e^{-j90}$ at 100 kHz. The electrode-tissue system parameters are given in Tables 2.3 and 2.4. The values of β_v have been calculated from Equation (4.6) and are given in Table 4.1. It is evident that for Example 1, $|\beta_v|$

TABLE 4.1
VALUES OF β_v FOR THE EXAMPLES OF CHAPTER 2*

Frequency	Example 1	Example 2
3 Hz	$0.17e^{-j72}$ ($0.0001e^{j0}$)	$0.00021e^{-j69}$ ($0.00001e^{j0}$)
100 kHz	$0.10e^{j58}$ ($0.067e^{j90}$)	$0.0067e^{j90}$ ($0.0067e^{j90}$)

*Values in parentheses are obtained by neglecting interface impedance.

is too large for single-ended amplification to be used. This case was noted in the section on differential operation where it was found that the rejection ratio of the differential amplifier would only have to be greater than 17 at 3 Hz and greater than 10 at 100 kHz.

The limits of cable and amplifier input admittance for the examples of Chapter 2 are given in Table 4.2 which is based on the values of β_v in Table 4.1. If the limits in Table 4.2 are compared with the corresponding limits in Tables 3.2 and 3.3, it is evident that the requirements on cable and amplifier input admittance have been significantly relaxed.

TABLE 4.2

LIMITS OF CABLE AND AMPLIFIER INPUT ADMITTANCE FOR THE
EXAMPLES OF CHAPTER 2*

		Example 1	Example 2	
G_{Q1}^{-1}	>	64M (40k)	64M (40k)	ohms at 3 Hz
G_{P1}^{-1}	>	64M (38k)	64M (38k)	
G_{P2}^{-1}	>	11M (3.8)	13k (.38)	
S_{Q1}^{-1}	>	58k (40k)	58k (40k)	ohms at 100 kHz
S_{P1}^{-1}	>	58k (38k)	58k (38k)	
S_{P2}^{-1}	>	5.8k (2.6k)	380 (260)	
C_{Q1}	<	27 (39)	27 (39)	picofarads
C_{P1}	<	27 (41)	27 (41)	
C_{P2}	<	270 (600)	4,000 (6,000)	

*Based on β_v from Table 4.1. Values in parentheses are obtained by neglecting interface impedance.

Ground Admittance

As in Chapter 3, assume that all of the ground admittance, denoted by Y_g in Figure 4.3, is concentrated at a point of maximum voltage magnitude in the tissue mass. In the virtual-ground system, the maximum voltage may occur at points adjacent to the Q1 and/or the Q2 electrode. For points adjacent to Q1, the figure of merit defined by Equation (3.42) is

$$F_{g1} = \left| \frac{V_{Q1} - Z_{Q1} I_{Q1}}{I_{Q1}} \right| \approx \left| m_{31} + (1 + \beta_v) m_{11} - Z_{Q1} \right| \quad (4.27)$$

where V_{Q1} has been eliminated by means of Equations (4.17), and (3.8).

For points adjacent to Q2, the figure of merit is

$$F_{g2} = \left| \frac{-K_v V_{P2} + (Z_{Q2} + Z_o) I_{Q2}''}{I_{Q1}} \right| \approx \left| -K_v \beta_v m_{11} + Z_{Q2} + Z_o \right| \quad (4.28)$$

where V_{P2} and I_{Q2}'' have been eliminated by means of Equations (4.2), (3.8), and (4.4).

Replacing the m parameters by their constituents from Equation (2.22), and substituting for β_v from Equation (4.6), Equations (4.27) and (4.28) may be written

$$F_{g1} \approx |h_{31} + h_{11} + \beta_v h_{11}| \quad (4.29)$$

and

$$F_{g2} \approx \left| -h_{23} + \frac{Z_{Q2} + Z_o}{K_v} \right| \quad (4.30)$$

It is evident that both F_{g1} and F_{g2} are smaller than F_g of the classical method given in Equation (3.45). The results of Equation (3.46), using F_{g1} and F_{g2} in place of F_g for the examples of Chapter 2, are summarized in Table 4.3. As before, Z_o is neglected and K_v is assumed to be $2 \cdot 10^5 e^{-j0}$ at 3 Hz and $300 e^{-j90}$ at 100 kHz.

TABLE 4.3

LIMITS OF GROUND ADMITTANCE FOR THE EXAMPLES OF CHAPTER 2*

		Example 1	Example 2	
G_{g1}^{-1}	>	100k (100k)	98k (98k)	ohms at 3 Hz
G_{g2}^{-1}	>	96k (96k)	4.8k (4.8k)	
S_{g1}^{-1}	>	100k (100k)	98k (98k)	ohms at 100 kHz
S_{g2}^{-1}	>	96k (96k)	4.8k (4.8k)	
C_{g1}	<	15 (15)	16 (16)	picofarads
C_{g2}	<	16 (16)	320 (320)	

*Values in parentheses are obtained by neglecting interface impedance.

Current Control Error

Consider again the current control source shown in Figure 3.6, but with V_Q replaced by V_{Q1} . The error analysis of Chapter 3 may be

applied directly to the virtual-ground system if α_Q of Equation (3.60) is replaced by β_Q , where

$$\beta_Q \equiv \frac{V_{Q1}/I_Q}{R_Q} \quad (4.31)$$

Using Equations (4.17), (3.64), and (3.8), the expression for β_Q becomes

$$\beta_Q \approx \frac{m_{31} + (1+\beta_v)m_{11}}{R_q} \quad (4.32)$$

Replacing m_{31} and m_{11} by their constituents from Equation (2.22), Equation (4.32) yields

$$\beta_Q \approx \frac{Z_{Q1} + h_{31} + h_{11} + \beta_v h_{11}}{R_q} \quad (4.33)$$

It is evident that β_Q is smaller than α_Q as given for the classical method in Equation (3.66). If $|\beta_Q|$ is limited to less than 0.01, the requirement on R_q becomes

$$R_q > 100 \left| Z_{Q1} + h_{31} + h_{11} + \beta_v h_{11} \right| \quad (4.34)$$

which is to be compared with Equation (3.69). The limits on R_q for the examples of Chapter 2 are summarized in Table 4.4 and are to be compared with those of Table 3.60.

TABLE 4.4

MINIMUM VALUES OF CURRENT SOURCE RESISTANCE*
FOR THE EXAMPLES OF CHAPTER 2

Frequency	Example 1	Example 2	
3 Hz	160M (100k)	160M (100k)	ohms
100 kHz	147k (100k)	145k (98k)	

*Based on β_v from Table 4.1. Values in parentheses are obtained by neglecting interface impedance.

Note that for Example 1, the virtual-ground method reduces the resistance requirement to approximately half that of the classical method. For the assymetrical electrode-tissue system of Example 2, the improvement is negligible.

Stability Considerations

If the virtual-ground system is to be used in the single-ended mode for broadband measurements, the unity gain frequency of the virtual-ground amplifier, in most cases, would have to be greater than 4 MHz to meet common mode rejection requirements at signal frequencies. In such systems, special techniques must be employed to assure stability for various operating conditions. These techniques and their rationale are the subject of this section.

The loop gain of the virtual-ground amplifier circuit shown in Figure 4.3 may be written

$$K'_v = -K_v(f)\Gamma_v(f) \quad (4.35)$$

where Γ_v is the complex voltage transfer function from Q2 to P2 of the network consisting of the electrode-tissue system and all of its loading admittances. As before, $-K_v$ is the complex open-loop unloaded gain of the virtual-ground amplifier. The effect of amplifier output impedance is considered in a later paragraph. It is reasonable to assume that the magnitude of K_v' decreases monotonically with frequency. If f_u' designates the frequency at which $|K_v'|$ becomes unity, the condition for stability is

$$f_u' < f_\pi \quad (4.36)$$

where f_π is any frequency at which the sum of the phase lags in K_v and Γ_v becomes 180 degrees.

Nominal magnitude and phase characteristics of K_v are sketched in Figure 4.2. Over most of the spectrum $|K_v|$ is a linear function of frequency. The phase lag is fairly constant except where the slope of $|K_v|$ is changing. At higher frequencies where stability becomes a problem, the phase lag is at least 90 degrees. The frequency at which $|K_v|$ crosses unity is designated by f_u . Near f_u , the phase lag begins to increase sharply but does not pass through 180 degrees until beyond f_u .

Since Γ_v describes a passive resistance-capacitance network, $|\Gamma_v|$ is always less than unity, so that f_u' is always less than f_u . It follows that only three different sequences are possible for the critical frequencies. With frequency increasing from left to right, these sequences are

$$f_{\pi}, f_u', f_u \quad (4.37)$$

$$f_u', f_u, f_{\pi} \quad (4.38)$$

$$f_u', f_{\pi}, f_u \quad (4.39)$$

The first sequence is the unstable condition to be avoided. The second sequence is stable, but it places f_{π} in a region where the phase lag in K_v is approaching 180 degrees and leaves only a small margin for the phase lag of Γ_v . Therefore, it would not occur, in practice, unless f_u were relatively low (e.g., below 4 MHz). A low f_u proportionately reduces $|K_v|$ at signal frequencies, which is undesirable. The third sequence represents the most efficient condition and is considered further in the section on stabilization techniques.

The phase lag in Γ_v is caused by Y_{Q1} , Y_{P1} , Y_{P2} and Y_g which are capacitive at high frequencies and significantly load the electrode-tissue system. For a given set of loading admittances (of all four classes), the resulting phase lag in Γ_v depends on the h parameters (or the W elements) of the electrode-tissue system. Thus, a given instrumentation system may operate in a stable mode with some electrode-tissue systems, and not with others, or it may not be stable with any.

To illustrate the foregoing discussion, consider the simplified equivalent network shown in Figure 4.4. The W elements correspond to those of Figure 2.7 and the capacitors represent the major components of Y_{Q1} , Y_{P1} , Y_{P2} and Y_g , respectively. Symbols v , r and e have been

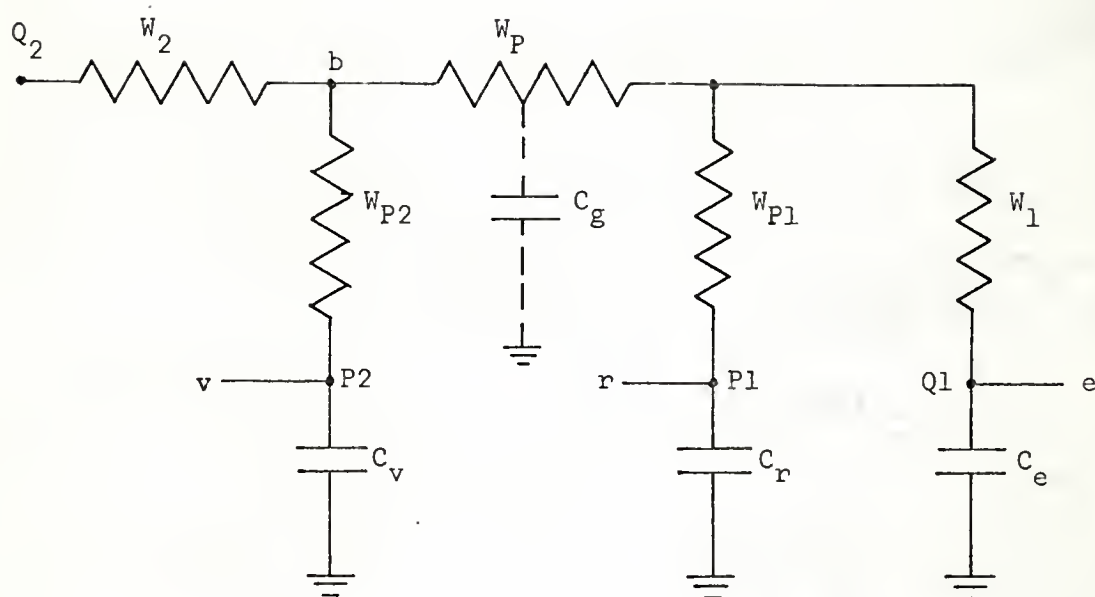


Figure 4.4. Simplified Equivalent Circuit for the Virtual-Ground Amplifier Feedback Loop

introduced for convenience in the next section. The transverse loading admittance, the effective interface impedances and W_Q have been neglected. It is evident that there may be a phase lag from Q_2 to b and an additional lag from b to v . The lag from b to v will usually be the larger of the two, but it may not exceed 90 degrees. The total lag from Q_2 to v becomes worse (and f_π decreases) as W_2 and W_{P2} become large and W_P , W_{P1} and W_1 become small. It may exceed 90 degrees.

The output impedance of the virtual-ground amplifier should be negligible compared to the capacitive reactance at Q_2 to avoid an additional phase lag in the loop. Output impedances below 50 ohms

are desirable. If necessary, this condition may be achieved by adding an emitter follower circuit at the amplifier output terminal.

Stabilization Techniques

The techniques described in this section are suggested as a means of achieving the condition in Equation (4.39) with as large an f_u as practical. For clarity, the stabilization process may be viewed in two steps:

Make f_π as large as possible

Select f_u and reduce f'_u below f_π

These steps are explained in the following paragraphs.

Maximizing f_π

As a rule, f_π will lie in a region where the phase lag in K_v is approximately 90 degrees (or somewhat larger). Consequently, the phase lag in Γ_v at f_π will also be approximately 90 degrees (or somewhat smaller). The task of maximizing f_π is equivalent to minimizing the capacitive effects that cause the lag in Γ_v . For this purpose, resistors are added in series with each of the loading capacitors as indicated by R_{Q1} , R_{P1} , R_g and R_v in Figure 4.5. For the present discussion, neglect the presence of R_{P2} . If these resistors are sufficiently large, the lag from Q2 to b and from b to v will each be reduced to safe values. However, upper limits are forced on R_{Q1} and R_{P1} by the loading error conditions which must be

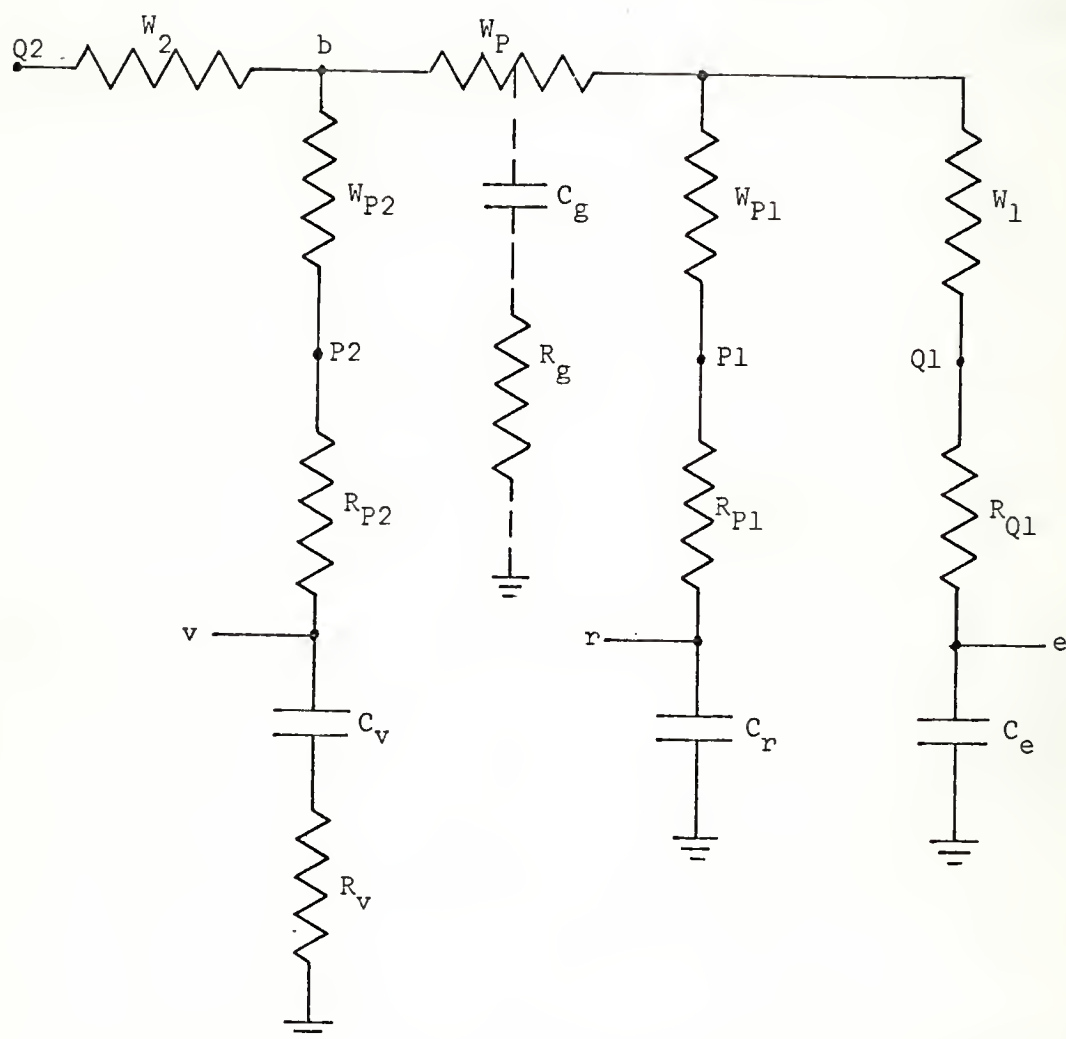


Figure 4.5. Stabilization Techniques for the Virtual-Ground Amplifier Feedback Network

satisfied at signal frequencies. Equations (4.24) and (4.25) are applicable if C_r and C_e are used to calculate Y_{P1} and Y_{Q1} , and R_{Q1} and R_{P1} are considered as part of Z_{Q1} and Z_{P1} , respectively.

In the simplified circuit of Figure 4.5, the lag from Q2 to v

would peak at some intermediate frequency (or frequencies) and become zero at higher frequencies. Actually, all of the loading capacitance cannot be compensated with series resistance. The scheme shown in Figure 4.5 pertains primarily to cable shields and other conducting objects (table tops, cages, etc.) which are in proximity to critical parts of the system and require a ground connection to reduce extraneous noise. These items usually introduce capacitance in the range of 20 to 200 picofarads, which if left uncompensated would reduce f_{π} to undesirably low values (for example, below 4 MHz).

There remain scattered throughout the Γ_v network small parasitic elements which cause the lag from Q2 to v to continue to increase at higher frequencies. Included in this group is the input capacitance of the virtual-ground amplifier. These elements impose a natural upper limit on f_{π} . Fortunately, they can usually be held to small values (typically 0.5 to 10 pf) so that, in most cases of interest, f_{π} would be greater than 10 MHz.

Reducing f'_u

As indicated earlier, f'_u will always be less than f_u . Thus if f_u were not much greater than f_{π} , the existing attenuation of Γ_v might be sufficient to place f'_u below f_{π} , resulting in a stable condition. This possibility unnecessarily restricts f_u and is not reliable since f_{π} and Γ_v will vary with different electrode-tissue systems. In some cases, such a system might actually be operating in the condition of Equation (4.38). Furthermore, as f_u is decreased toward f_{π} , f_{π} also decreases because of the increasing phase lag

in K_v . It is evident that a larger f_u may be used if f'_u is reduced by additional means.

To reduce f'_u , it is convenient to use the lag attenuator network consisting of C_v , R_v , W_{P2} and R_{P2} as indicated in Figure 4.5. Normally, R_{P2} and R_v are the controllable elements, while C_v is a cable shield capacitance and W_{P2} is an electrode-tissue system parameter. Typical magnitude and phase characteristics of the transfer function from b to v of this network are sketched in Figure 4.6.

The break frequencies of the lag network are given by

$$f_1 = \frac{1}{2\pi(W_{P2} + R_{P2} + R_v)C_v} \quad (4.40)$$

$$f_2 = \frac{1}{2\pi R_v C_v} \quad (4.41)$$

and the attenuation factor is

$$\xi = \frac{f_1}{f_2} \quad (4.42)$$

The peak phase lag occurs at

$$f_p = \sqrt{f_1 f_2} \quad (4.43)$$

and is given by

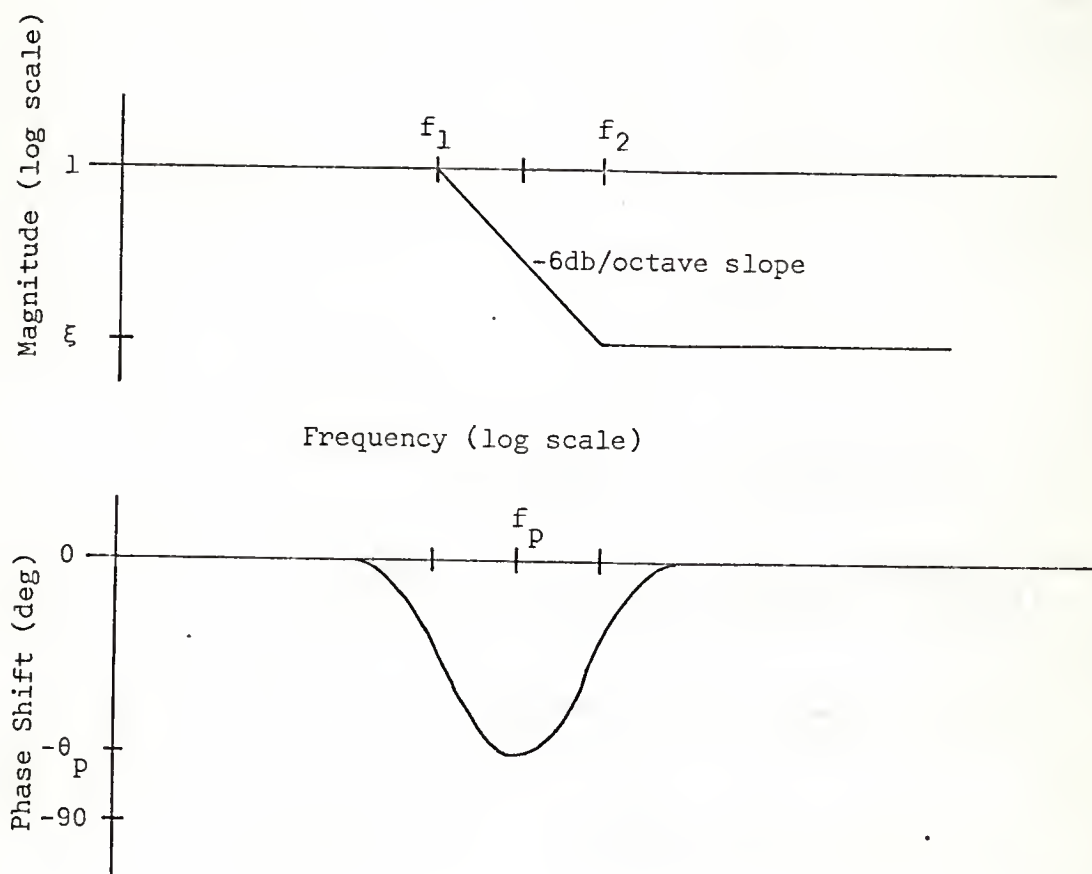


Figure 4.6. Typical Magnitude and Phase Characteristics of a Lag Network

$$\theta_p = (90 - 2 \tan^{-1} \sqrt{\xi}) \text{ degrees} \quad (4.44)$$

which may be rearranged to give

$$\xi = \left[\tan \left(45 - \frac{\theta_p}{2} \right) \right]^2 \quad (4.45)$$

The major design parameters are f_1 and ξ . The selection of these factors is not unique. It is, however, subject to certain constraints which are discussed in the following paragraphs.

Restrictions on f_1 .--At signal frequencies, loading error in the P2 arm must be negligible. The condition in Equation (4.26) is applicable and may be rearranged to give

$$\frac{1}{2\pi|Z_{P2} + h_{13} + R_{P2}|C_v} > 40f|\beta_v| \quad (4.46)$$

where R_{P2} has been included as part of the electrode-tissue system, Y_{P2} has been replaced by the admittance of C_v , and R_v has been neglected. The worst case occurs at the highest signal frequency of interest, hereafter designated by f_s . At f_s the left term in Equation (4.46) will usually approximate f_1 as given in Equation (4.40). Thus to a first approximation, f_1 should meet the following condition

$$f_1 > 40f_s|\beta_v| \quad (4.47)$$

where β_v is evaluated at f_s . This condition holds whether the system is operated in the single-ended or the differential mode. In the single-ended case, $|\beta_v|$ must be very small so that f_1 could, in principle, be less than f_s . However, a factor of safety may be necessary because of the variable nature of W_{P2} . Even in the differential mode, $|\beta_v|$ would normally be less than unity so that the limit in Equation (4.47) would never be greater than $40f_s$.

Restrictions on ξ .--The peaked phase lag characteristic of Figure 4.6 raises the possibility of a new f_π in the region between f_1 and f_2 in addition to the inherent f_π at higher frequencies. To avoid this potentially unstable situation, the phase lag from Q2 to v at frequencies between f_1 and f_2 must be less than 90 degrees. This lag is likely to be greatest at approximately f_p . If the phase lag from Q2 to b at f_p is designated as ϕ_p , then θ_p must satisfy the following inequality

$$\theta_p < (90 - \phi_p) \text{ degrees} \quad (4.48)$$

An equivalent inequality on ξ results if Equation (4.48) is substituted into Equation (4.45)

$$\xi > \left[\tan \frac{\phi_p}{2} \right]^2 \quad (4.49)$$

Numerical values for this inequality are given in Table 4.5.

TABLE 4.5
LIMITS OF ξ FOR GIVEN VALUES OF ϕ_p

ϕ_p degrees	$\xi >$
10	.0075
20	.031
30	.072
40	.13
50	.22
60	.33

Since f_1 must be on the same order as or greater than f_s , f_p will usually fall in a region (e.g., above 1 MHz) where ϕ_p may not be neglected. To be sure, at least a 10-degree factor of safety is necessary. In many cases, much larger values may be required. It follows that ξ cannot, in general, be made arbitrarily small.

Amplifier considerations.--Since the minimum value of ξ is restricted, f_u cannot be arbitrarily large if f'_u is to be kept below the inherent limit on f_π . In a properly adjusted attenuator network, f'_u will fall above f_2 and will be somewhat lower than ξf_u due to the additional attenuation from Q2 to b. The input capacitance of the virtual-ground amplifier should be as small as possible (less than 10 pf) to minimize the loading of R_v and maximize the inherent limit of f_π . To accommodate a wide range of electrode-system parameters, it is desirable to make R_v and possibly R_{p2} variable.

In summary, stabilization of the virtual-ground system involves the selection of at least four resistors (two for the P2 arm, and one each for the P1 and Q1 arms). Some resistance can often be put in the ground paths of C_r and C_e with similar stabilizing effects. The resistor selection is somewhat arbitrary and will depend largely on how a particular system is implemented. The most satisfactory set of values generally must be found by an educated trial and error procedure based on the theory presented and certain common considerations.

The stabilizing resistors which occur in series with the terminals of the electrode-tissue system are indicated in Figure 4.7.

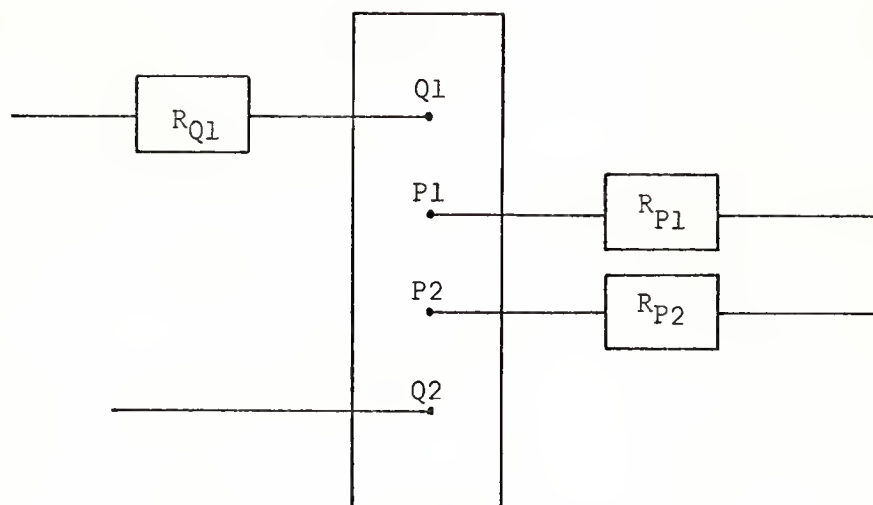


Figure 4.7. Electrode-Tissue System with Stabilizing Resistors

It is convenient to view these resistors as additions to the corresponding effective interface impedances, i.e., Z_{Q1} , Z_{P1} and Z_{P2} . With this simple modification, the analytical results derived in previous sections may be applied directly to the compensated system. The same convenience applies to the noise analyses that follow.

Noise in the Virtual-Ground System

Instrumentation Noise

Instrumentation noise arises in the virtual-ground amplifier and the response amplifier. For reasons similar to those discussed in Chapter 3, the instrumentation noise of greatest significance is that which may be described by means of a noise voltage source in

series with the amplifier input terminals. These sources are represented as N_v and N_r in Figure 4.3. N_v produces a noise component at the input to the response amplifier which together with N_r comprises the instrumentation noise that is amplified along with the desired response signal.

The noise due to N_v at the input of the response amplifier may well be greater than N_v itself. To verify this statement, consider again the simplified network in Figure 4.5. The gain for N_v from the input of the virtual-ground amplifier to Q2 is given by

$$K_N = \frac{-K_v}{1 + K_v \Gamma_v} \quad (4.50)$$

where, as before, Γ_v is the transfer function from Q2 to v and $-K_v$ is the open-loop unloaded gain of the amplifier. If Γ_r designates the complex transfer function from Q2 to r (the input to the response amplifier), then the power spectral density of the noise at r due to N_v is given by

$$N_{rv}(f) = |K_N(f)\Gamma_r(f)|^2 N_v(f) \quad (4.51)$$

where the symbol N is taken to mean power spectral density. If $|K_N \Gamma_r|$ is greater than unity in a certain frequency band, then the noise power at r will be greater than the noise power of N_v in that band.

As a rule, the instrumentation system is designed to minimize loading at the P1 terminal so that $|\Gamma_r|$ will usually remain close to

unity at all frequencies of concern. Therefore, it follows from Equation (4.51) that N_{rv} will be greater than N_v at approximately those frequencies where $|K_N|$ exceeds unity. In the signal band (below 200 kHz) and perhaps somewhat higher, $|K_N|$ is approximately equal to unity (see Equation [4.50]) because $|K_v|$ is large and $|\Gamma_v|$ is approximately unity. At higher frequencies, $|K_v \Gamma_v|$ crosses unity at f'_u , while $|K_v|$ crosses unity at f_u . As indicated in the section on stability, f'_u is usually well below f_u . Hence $|K_N|$ may be greater than unity for frequencies above the signal band and up to approximately f_u (e.g., at frequencies between 300kHz and 30MHz). In at least part of this range, the instrumentation noise at Pl due to N_v will generally be enhanced. Experimental evidence indicates that this enhancement will usually correspond to less than a factor of two in the noise voltage level at Pl.

It is evident that the virtual-ground system is inherently noisier than the classical system with respect to a given level of amplifier noise. Fortunately, a significant portion of the power in this noise lies at frequencies well above the usual impedance measurement band and it can be filtered out after amplification. In addition, because of its regular random nature, instrumentation noise may be eliminated by means of standard averaging techniques.

Environmental Noise

The effects of environmental noise on the virtual-ground system are similar to those found in the classical system. Consider, for example, the electrostatically coupled noise currents, I_x ,

indicated in Figure 4.3. The noise voltage at P1 due to these currents is

$$V_{Plx} = V_{Px} + \frac{V_{2x}}{1 + K_v} \quad (4.52)$$

This expression is the dual of Equation (3.73) with V_{Plx} replacing V_{Px} and $1 + K_v$ replacing ρ . The values of V_{Px} and V_{2x} are essentially as given by Equations (3.74) and (3.76), respectively. Finally, the virtual-ground equivalent of Equation (3.77) is

$$\frac{V_{Plx}}{V_P} = \frac{I_x}{I_{Q1}} \left[\frac{Z_{P1} - Z_{P2} + h_{12} - h_{13}}{h_{11}} + \frac{Z_{P2} + 2Z_{Q2} + h_{13} + 2h_{23} + 2h_{33}}{(1 + K_v)h_{11}} \right] \quad (4.53)$$

As before, the cancellation occurring in the numerator of the left term in the brackets is neither complete nor easy to control and cannot be used as a reliable index of noise reduction. Also, the term on the right in the brackets is not likely to be important because K_v will usually be quite large.

If the signal voltage is required to be greater than ten times the noise voltage, then the dual of Equation (3.78) is for the virtual-ground system

$$\frac{|I_{Q1}|}{|I_x|} > 10 \left[\frac{Z_{P1} - Z_{P2} + h_{12} - h_{13}}{h_{11}} + \frac{Z_{P2} + 2Z_{Q2} + h_{13} + 2h_{23} + 2h_{33}}{(1 + K_v)h_{11}} \right] \quad (4.54)$$

As in the classical system, this inequality can seldom be satisfied unless the potential cables are shielded.

Electrode-Tissue Noise

The electrode-tissue noise at the input of the response amplifier in Figure 4.3 is equal to the noise in V_p (including two interfaces), plus a contribution from the noise in V_2 due to the fact that K_v is not infinite. This is similar to what occurs in the classical system except that K_v takes the place of the amplifier common mode rejection ratio. As a rule, electrode-tissue noise in V_2 will not saturate the virtual-ground amplifier because it appears in the feedback path where the dynamic range is large (e.g., ± 10 volts). On the other hand, noise in V_p may saturate the response amplifier and/or the instruments that follow it. This problem is resolved conveniently by means of the negative feedback filter loop, described in the next section.

The Negative-Feedback Filter Loop

The negative-feedback filter loop provides a high performance alternative to using a.c. coupling between the response amplifier and the electrode-tissue system. It permits the filter for d.c. and noise rejection to be placed outside the main signal channel, where it introduces no spurious effects on the signal and adjustments are

particularly convenient to make. This arrangement is especially desirable in a system which is to operate over a broad frequency spectrum. The feedback filter loop is also convenient for reducing the operating point disturbances that accompany changes from one electrode-tissue system to another.

Many operational amplifiers are available with a noninverting input channel in addition to the standard inverting connection. In the virtual-ground system of Figure 4.8, the output of the response

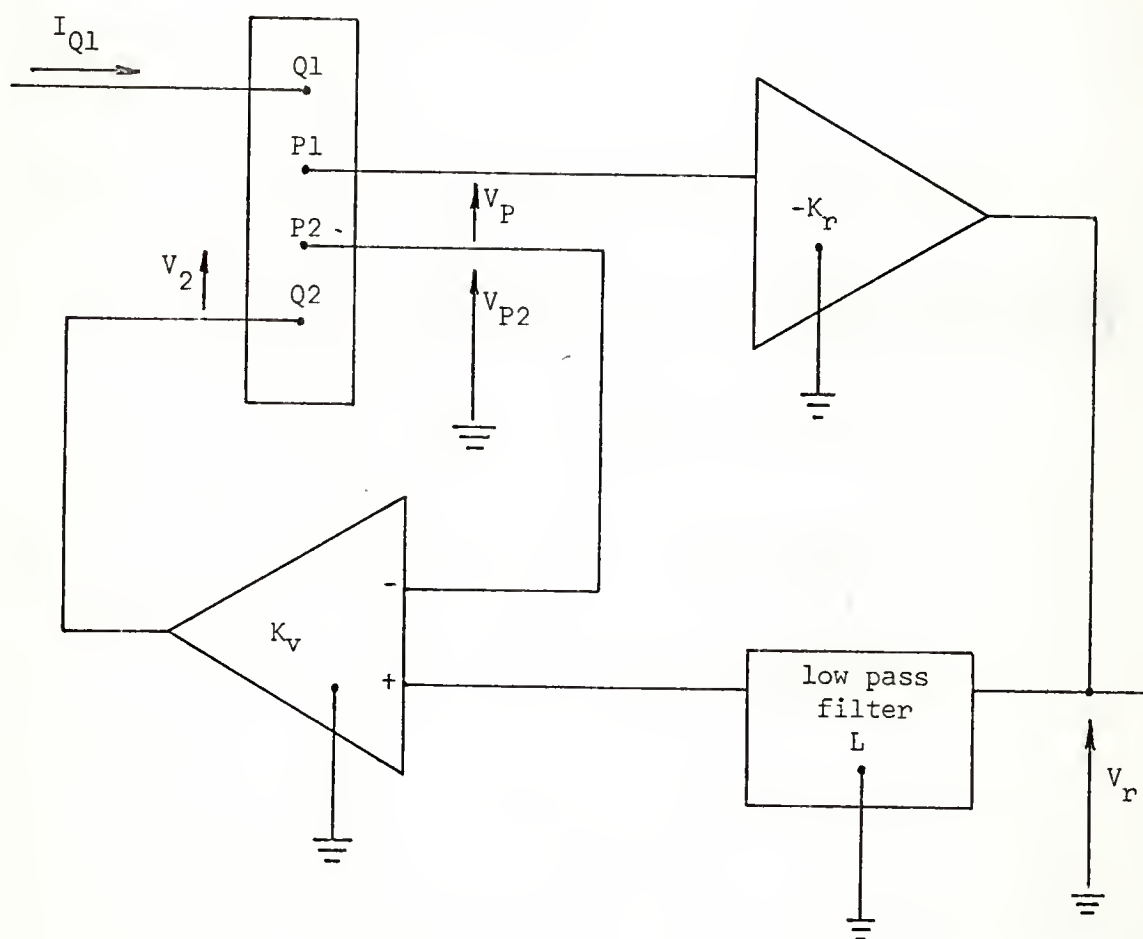


Figure 4.8. Virtual-Ground System with Negative-Feedback Filter Loop

amplifier is fed back through a low-pass filter to the noninverting side of the virtual-ground amplifier. Signals with frequencies well within the filter pass band are subject to heavy negative feedback while those with frequencies well beyond the pass band are not feedback at all. In this way, the system is made to fully amplify the higher frequency signals, while the lower ones are passed with little or no amplification. The feedback filter loop is relatively insensitive to extraneous disturbances and greatly facilitates the use of variable and large filter components.

With reference to Figure 4.8, the output voltage of the response amplifier is

$$V_r = -K_r(V_P + V_{P2}) \quad (4.55)$$

where $-K_r$ is the complex gain of the response amplifier. Further, it is not difficult to show that

$$V_{P2} = \frac{V_2 + K_v(1 + \frac{1}{\rho})LV_r}{1 + K_v} \quad (4.56)$$

where ρ is the common mode rejection ratio of the virtual-ground amplifier and $L(f)$ is the complex voltage transfer function of the feedback filter. As before, K_v is the unloaded open-loop complex gain of the virtual-ground amplifier and the output impedance is neglected. Substituting Equation (4.56) into Equation (4.55) and solving for V_r yields

$$V_r \approx \frac{-K_r}{1 + LK_r} \left(V_P + \frac{V_2}{K_v} \right) \quad (4.57)$$

where the $1/\rho$ in the numerator and the unity in the denominator of the right side of Equation (4.56) have been neglected. The expression for V_r is discussed in the following paragraphs for desirable and undesirable signals.

Signals due to I_{Q1} .--For signals produced by I_{Q1} , the term in parenthesis in Equation (4.57) is equal to V_{P1} when there is no feedback filter and is given by Equation (4.1), where β_v is as given in Equation (4.6). Excitation for impedance measurements is normally produced at frequencies well above the filter pass band where $LK_r \ll 1$. For this case, Equation (4.57) becomes

$$V_r \approx -K_r \left(V_P + \frac{V_2}{K_v} \right) \quad (4.58)$$

which is as though the filter were absent.

Electrode-tissue noise.--The electrode-tissue noise voltages of interest occur in V_P and V_2 and are hereafter designated by V_{Pe} and V_{2e} , respectively. Looking out of the terminals of the electrode-tissue system, the effective impedance presented by the external circuit is quite high. Therefore, V_{Pe} and V_{2e} correspond to what would be observed if the electrode-tissue system were not connected. For noise voltages falling well within the filter pass band, $LK_r \gg 1$, and Equation (4.57) yields for the noise output

$$V_{re} \approx -\frac{1}{L}(V_{Pe} + \frac{V_{2e}}{K_v}) \quad (4.59)$$

In a typical passive filter, L is unity from d.c. through an arbitrary band of frequencies. In this range, the noise is passed without amplification. At higher frequencies, L begins to decrease and the noise amplification increases, eventually catching up with that of the signal (Equation [4.58]).

To illustrate the advantages of the filter loop, let K_r be 1000 and assume that the output stage of the amplifier has a maximum range of ± 10 volts. If this system were not compensated, it would tolerate, at most, ± 10 millivolts of d.c. and low frequency electrode-tissue noise. With the feedback filter, the system could handle up to ± 10 volts of the noise. In addition, the signal-to-noise ratio is improved by a factor of 1000.

Instrumentation noise.--Most of the energy in instrumentation noise lies at frequencies well above the pass band of the feedback filter. Accordingly, the analysis of instrumentation noise given in a previous section applies directly in the presence of the filter.

Environmental noise.--For environmental noise due to equal currents, I_x , the term in parenthesis in Equation (4.57), is equal to V_{Plx} as given in Equations (4.52) and (4.53). For noise frequencies well within the filter pass band,

$$V_{rx} \approx -\frac{1}{L}V_{Plx} \quad (4.60)$$

It is apparent that the feedback filter loop may be used for supplementary reduction of environmental noise provided that the noise frequencies are well below the signal frequencies of interest.

Examples of filter loop operation

To illustrate the operation of the feedback filter loop, let the feedback filter be as shown in Figure 4.9.

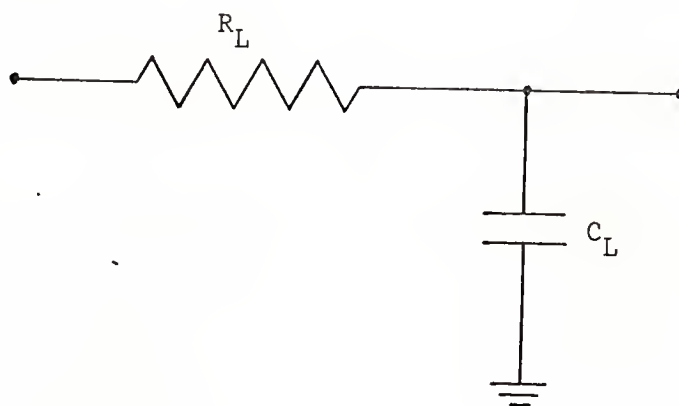


Figure 4.9. Simple Low-Pass Filter

For this filter,

$$L = \frac{1}{1 + jf/f_L} \quad (4.61)$$

and the overall transfer function indicated in Equation (4.57) becomes

$$T_L = \frac{-K_r}{1 + LK_r} = \frac{-K_r}{1 + K_r} \frac{1 + jf/f_L}{1 + jf/(1 + K_r)f_L} \quad (4.62)$$

where

$$f_L = \frac{1}{2\pi R_L C_L} \quad (4.63)$$

If, instead of using the low-pass feedback filter, the high-pass filter shown in Figure 4.10 were placed in the input path of the response amplifier, the overall transfer function would be

$$T_H = -K_r \frac{jf/f_H}{1 + jf/f_H} \quad (4.64)$$

where

$$f_H = \frac{1}{2\pi R_H C_H} \quad (4.65)$$

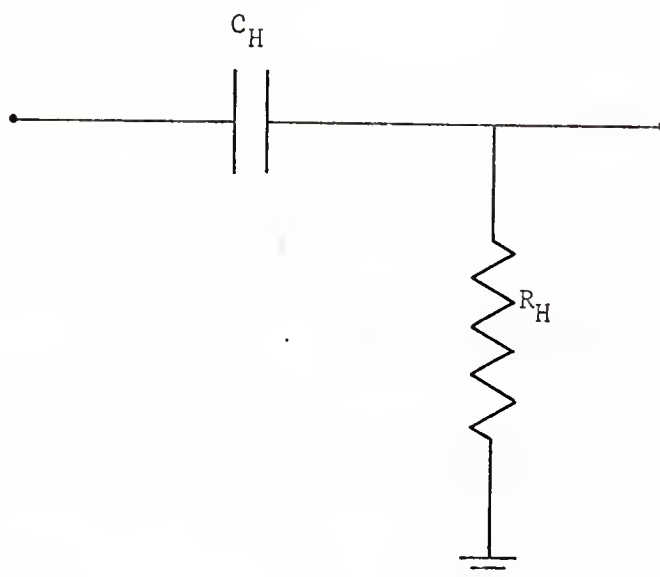


Figure 4.10. Simple High-Pass Filter

The asymptotic log modulus and phase characteristics of T_L and T_H are sketched in Figure 4.11 for the values $(1 + K_r)f_L = f_H = 1\text{Hz}$ and $K_r = 1000$. The characteristics of T_L and T_H are essentially identical except at frequencies near 10^{-3}Hz and below. In this region, the transfer function of the feedback method remains at unity, while the forward-path filter continues to attenuate. Since the gain is rather high, the advantage of extra attenuation in the latter case is not especially significant. Note that to achieve the same upper break frequency, f_L must be about one thousandth of f_H with correspondingly larger circuit elements. However, since the feedback filter occurs outside the amplifier and one end of the capacitor is grounded, the larger components present no special problem.

A disadvantage of simple filters is that the desired signal frequencies must be well above the upper break frequency to avoid phase distortion. For example, with reference to T_L and T_H , if phase distortion is not to exceed 2 degrees, signal frequencies must be at least 29 times greater than the break frequency.

The "dead space" between significant noise attenuation and the lowest allowable signal frequency may be reduced by adding a high pass filter in the forward path outside the feedback loop in addition to the feedback filter. For example, with the simple filters of Figures 4.9 and 4.10, the overall transfer function would be

$$T_{LH} = \frac{-K_r}{1 + K_r} \frac{1 + jf/f_L}{1 + jf/(1 + K_r)f_L} \frac{jf/f_H}{1 + jf/f_H} \quad (4.66)$$

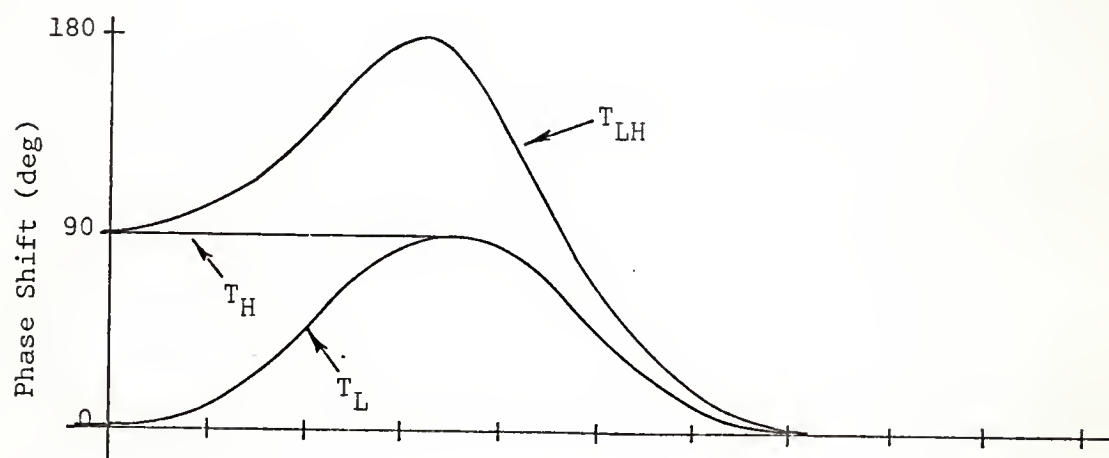
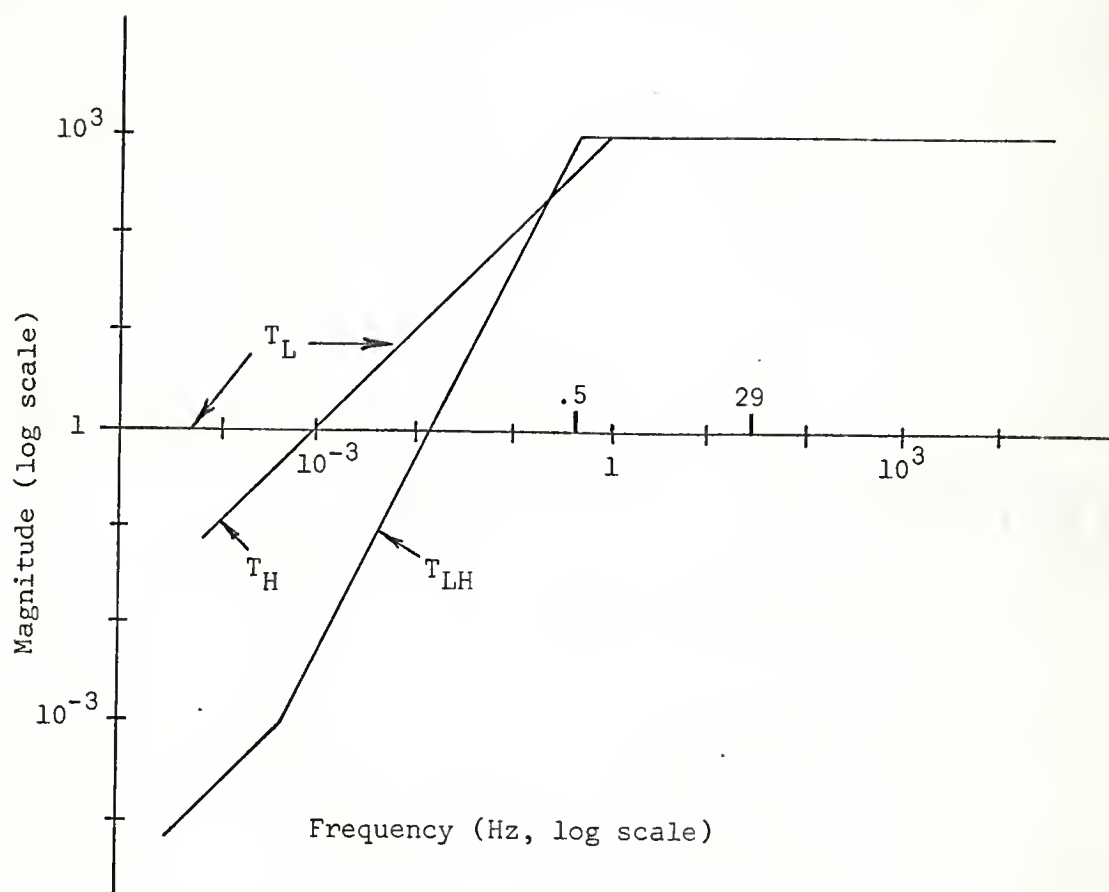


Figure 4.11. Overall Transfer Function Characteristics Using Several Methods of Noise Filtering

If the denominator break frequencies are made equal, i.e., $(1 + K_r)f_L = f_H$, then for less than 2 degrees' phase distortion, signal frequencies must be $58 f_H$ or greater. It follows that for the same lowest allowable signal frequency, the break frequencies of the combined filters must be half as large as the break frequency of either filter acting alone. The phase and log modulus characteristics of T_{LH} are indicated in Figure 4.11 for the case $(1 + K_r)f_L = f_H = 0.5 \text{ Hz}$ and $K_r = 1000$. It is evident that the noise attenuation is significantly improved with the combined filters for the same lowest allowable signal frequency.

Further reduction of the filter dead space between noise and useful signal frequencies may be achieved with higher order and nonlinear filters in the feedback and forward paths. In the design of second order and higher filters for the feedback loop, care must be exercised to prevent the appearance of underdamped complex roots in the closed-loop transfer function. Such roots may cause objectionable ringing to occur in the presence of common disturbances.

CHAPTER 5

AN EXPERIMENTAL SYSTEM BASED ON THE VIRTUAL-GROUND CONFIGURATION

Introduction

The theory and analysis of the virtual-ground system were given in Chapter 4. Much of that work was based on experience obtained with the experimental system described in the present chapter. The system was first assembled by the author in March of 1967, and minor improvements have been made as needed. Since that time it has been used regularly to measure impedance in certain animal tissues in situ. The major application has been concerned with the impedance properties of the cerebral cortex in unrestrained rats. This tissue is especially difficult to measure accurately because electrode dimensions must be quite small. Hence, it provides a proper proving ground for the virtual-ground technique. Some of the results of tissue measurements will be reported later in the chapter.

The basic configuration of the experimental system is shown in Figure 4.8 and may be referred to for the discussions that follow. The system consists of three major components, the virtual-ground amplifier, the response amplifier and the low-pass filter. In addition, a special current control circuit has been designed to supply the signal current. The various circuits are discussed in detail following a description of the physical layout.

The Physical Layout

A close-up photograph of the experimental virtual-ground system, with important components labeled, is shown in Figure 5.1. Four solid state operational amplifier units, similar to the one indicated, are plugged into sockets on the circuit board. The second response amplifier costs approximately \$85.00. The first response amplifier, the virtual-ground amplifier, and the current control amplifier are identical types and cost about \$155.00 each. The remaining components of the system, less power supply, total less than \$15.00. The entire system may be powered from a single supply with plus and minus 15 volt d.c. outputs and a 30 ma current capacity. The power unit shown in the picture is much larger than necessary.

Connection to the Electrode-Tissue System

Another view of the experimental virtual-ground system, including additional paraphernalia, is shown in Figure 5.2. The electrode-tissue system (in this case, rat plus electrode assembly) is connected to the circuit board by means of four miniature coaxial cables. The voltage and current cables are twisted in pairs to minimize extraneous electrical signals and coupling between the current and voltage circuits. The cables extend about 2.5 feet from the circuit board and end in a small female connector. The mating male connector is attached to the electrode-tissue system through approximately seven inches of unshielded wire. This arrangement is light and flexible and permits a great deal of versatility in connecting to various impedance subjects. The female connector also serves as a

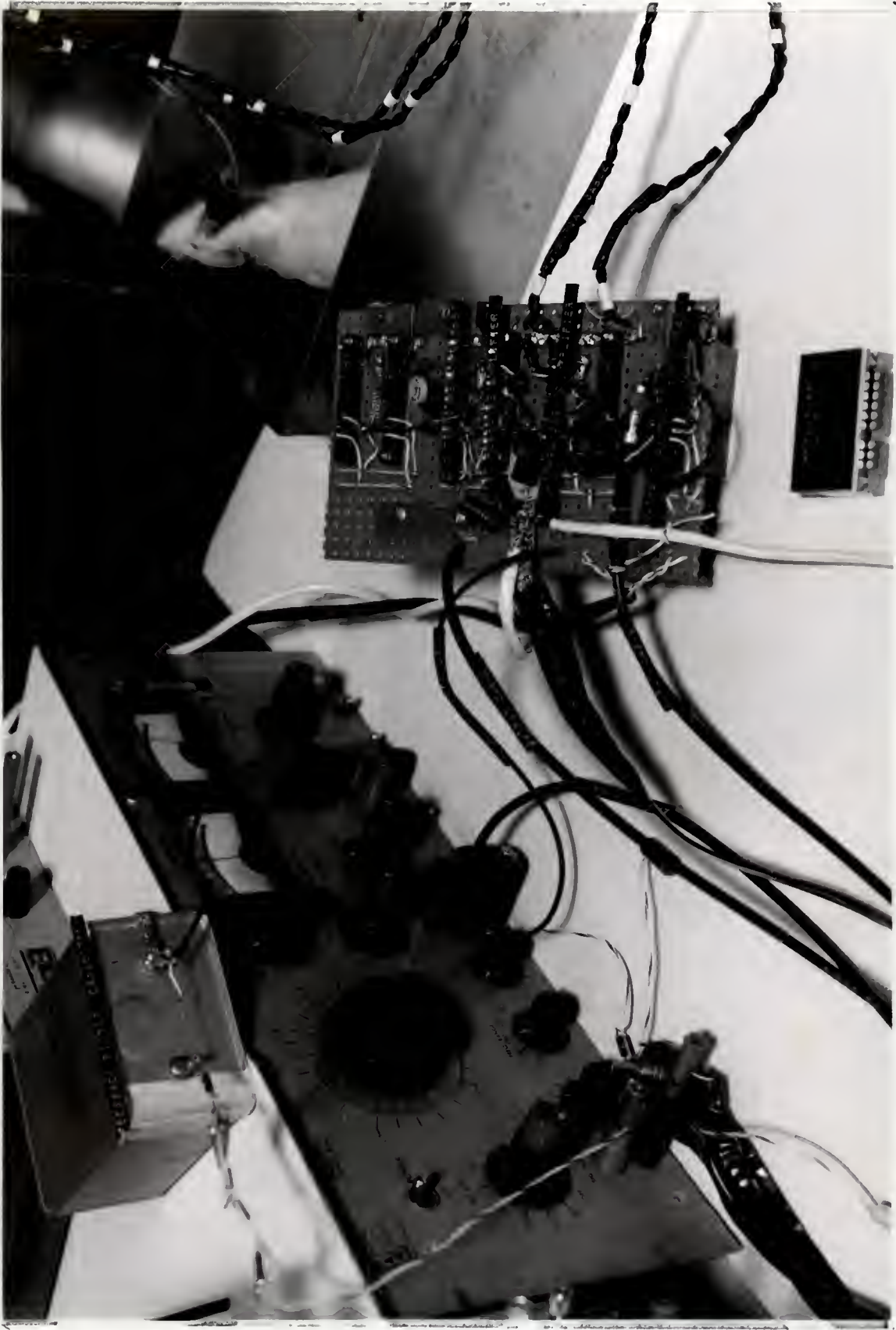


Figure 5.1. Close-Up Photograph of the Experimental Virtual-Ground System

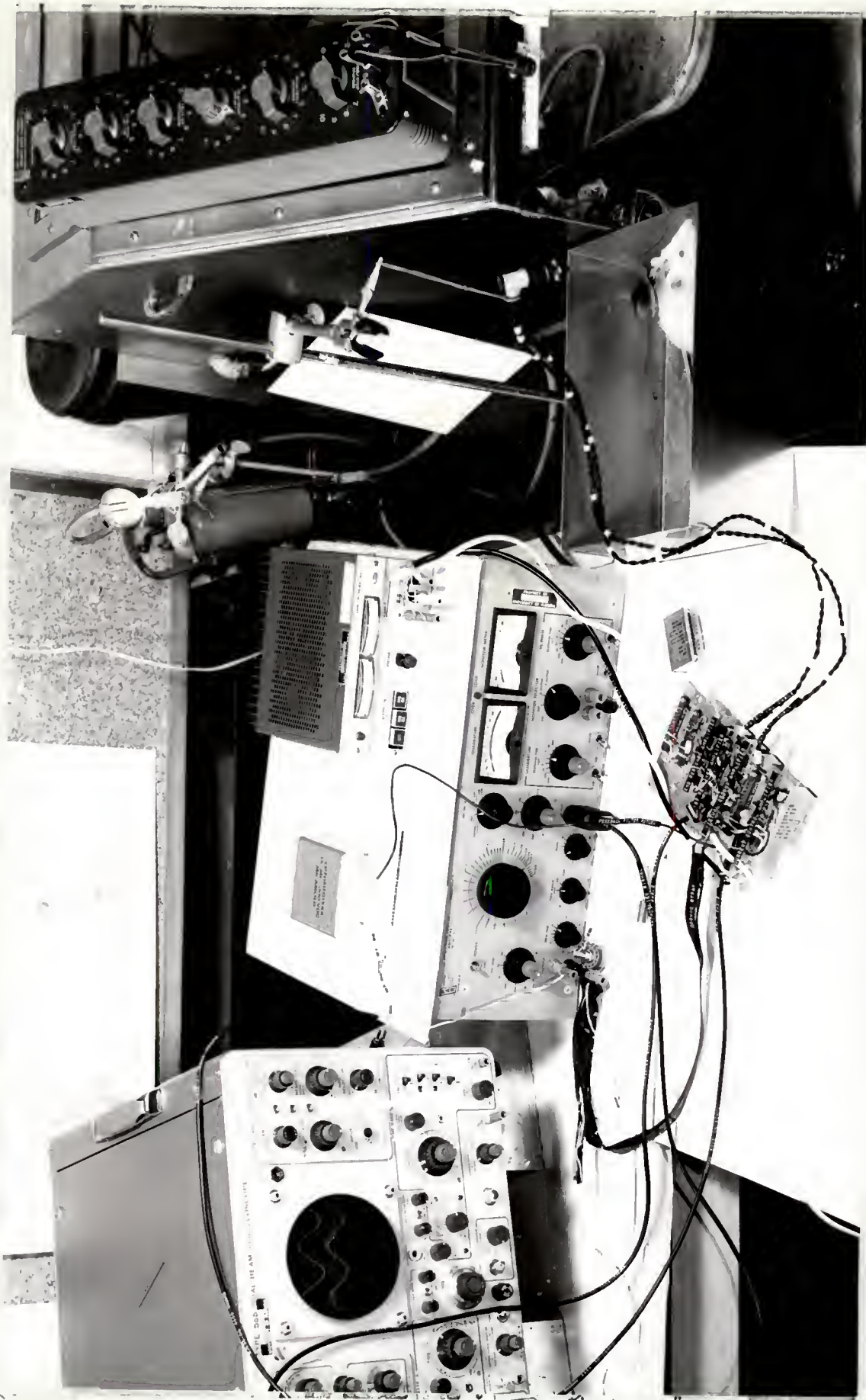


Figure 5.2. Complete View of the Experimental Arrangement

convenient location for the stabilization resistors R_{P2} , R_{P1} , and R_{Q1} as discussed in Chapter 4. In the present system, 2.2 kilohms has been a satisfactory value for R_{P2} and R_{P1} , and no resistor has been necessary for R_{Q1} .

The female connector actually comprises two sets of receptacles which have been soldered together. This feature facilitates changes from one electrode-tissue system to another (one of which may be for reference) and helps to minimize amplifier operating point disturbances during the changes. The double-ended connector also aids in the realization of an important advantage of the virtual-ground technique, i.e., the ability to check whether the common-mode error signal at P2 is indeed negligible. Hence, during an experiment, one simply disconnects the unshielded P1 lead at the electrode-tissue system and plugs it into the vacant P2 receptacle on the female connector, leaving the other leads undisturbed. The system output then reflects the voltage at P2, which should be negligible compared to the response at P1. Similarly, this technique may also be used to observe the voltages at Q1 and Q2 by plugging the P1 lead into the appropriate vacant receptacle. The connection at the electrode-tissue system itself is discussed later in the chapter.

As explained in Chapter 4, the shields of the P1 and P2 cables are especially important to reduce environmental noise. The shield of the Q1 cable is usually not important and that of the Q2 cable may be completely omitted.

The total shield to center conductor capacitance of each coaxial cable is approximately 130 picofarads. To avoid the effects of this

capacitance, each shield is connected in a special way on the circuit board. The shields of the Q1 and P1 cables are maintained at the same voltage as their center conductors to minimize the effective loading admittance at signal frequencies. These connections are described in the circuit section. The shield of the P2 cable is connected to ground by means of a miniature 500 ohm potentiometer which forms R_v of the stabilization scheme discussed in Chapter 4. The shield of the Q2 cable is generally not used.

Ground Connection

The system is connected to ground by means of a braided ribbon conductor (the ground strap) which is approximately 0.5 inch wide and 3 feet long. The ground strap serves as the signal common and is connected to an arbitrary ground point on the peripheral equipment. No other ground path is provided between the circuit board and the equipment (house) ground. The power supply common and the metal case of each amplifier are connected to ground on the circuit board.

Output Connection

The amplified voltage response is led out of the circuit board through approximately three feet of RG 58A/U coaxial cable (the output cable) which terminates in a BNC connector. The shield is connected to ground through a 270 ohm resistor on the circuit board. This resistor is a precaution to insure the stability of the output section of the response amplifier under the load of the shield capacitance. The shield is necessary to minimize feedback from the output cable to

low level parts of the system, which might otherwise cause instability.

The center conductor (but not the shield) of the output cable is connected to an oscilloscope which is used to monitor the voltage response. From this point, another coaxial cable is run to the input of the feedback filter and other measuring apparatus. The shield of this cable is joined to that of the output cable. The output of the feedback filter returns to the circuit board by means of a miniature coaxial cable. The cable shield is grounded at the circuit board and serves as the ground connection for the filter.

Input Connection

The current control circuit is excited by means of an external voltage generator. The cable from the generator usually runs directly to an oscilloscope which monitors the input signal. At this point, it feeds the input cable of the virtual-ground system which consists of 2.5 feet of RG 58A/U coaxial cable terminated in a BNC connector. The shields of both cables are grounded to the equipment.

Circuit Details

The Response Amplifier

The response amplifier consists of two sections as shown in Figure 5.3. The first section is a common voltage follower configuration with a nominal noninverting gain of 3.13. A voltage divider is connected at its output to provide a unity gain point for the shield of the P1 cable. The input impedance of this section corresponds to

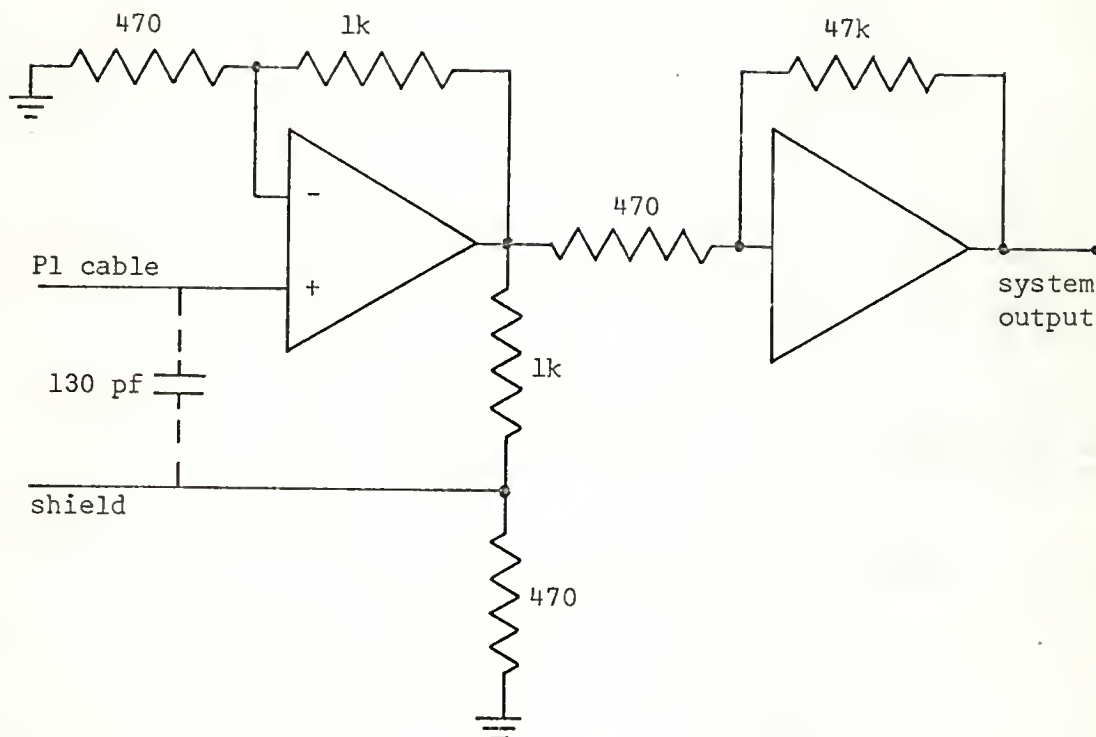


Figure 5.3. The Response Amplifier Circuit

10^{11} ohms in parallel with 5 picofarads which is more than adequate for virtual-ground operation. These values stem from a field effect transistor input stage which also requires negligible d.c. offset current (less than 150 picoamperes) from the electrode-tissue system. The second section of the response amplifier is a common inverter circuit with a nominal gain of 100.

An analysis of the follower and inverter configurations is presented in Appendices 2 and 3. The first and second amplifier units have unity gain frequencies of at least 30 MHz and 100 MHz, respectively. Hence, according to Equation A2.1, the first section should have less

than 1 percent decrease in gain out to 100 kHz. The gain of the second section tends to decrease somewhat as 100 kHz is approached due to the finite gain of the amplifier unit (see Equation [A3.1]). This feature may be used to advantage to offset a slight current increase which occurs due to parasitic capacitance in the current control circuit at high frequencies (see Current Control Error in Chapter 3). Additional flattening of the system response (from input signal voltage to system output for a purely resistive electrode-tissue system) has been accomplished by adding an adjustable series resistor-capacitor combination in parallel with the 47 kilohm feedback resistor.

The high gain of the response amplifier predisposes the system to instability due to spurious feedback from the system output to the P1 cable (center conductor and shield) and less importantly to the Q1 and P2 cables. Therefore, a shielded cable is used for the output channel. The shield is connected to ground through a 270 ohm resistor to insure the stability of the output section against the reactive load of the shield capacitance. Another precaution is to connect a suitable capacitor from the shield of the P1 cable to ground. In the present system, a 300 picofarad capacitor has been satisfactory. Acting in parallel with the 470 ohm divider resistor, this capacitor does not affect the +1 gain return to the P1 shield at signal frequencies, but becomes effective at higher frequencies where instability normally occurs. It also serves to counter the increase in high frequency amplifier noise which accompanies the +1 connection.

The Virtual-Ground Amplifier

The virtual-ground amplifier was chosen for its low d.c. offset current, high gain and broad bandwidth, and is identical in design to the first response amplifier. This particular unit exhibits a frequency dependent output impedance which decreases from roughly 50 kilohms at very low frequencies to less than 50 ohms at 100 kHz.

Recall that the common mode rejection of the system is described by β_v as defined in Equation (4.2). If $|\beta_v|$ is to be less than 0.01, then according to Equation (4.5), the voltages of the electrode-tissue system under study must satisfy the following requirement

$$\frac{|v_2|}{|v_p|} < 0.01 |K_v| \quad (5.1)$$

where the Z_o and the unity terms have been neglected. For the amplifier used here, the right side of Equation (5.1) becomes approximately 2,000 at very low frequencies and 3 at 100 kHz. That these conditions are met in a particular experiment may be easily checked as described in a previous section.

The Feedback Filter

The feedback filter is of the form shown in Figure 4.9. The capacitor is a large fixed element of 15 uf and is nonelectrolytic. Resistor values from 100 megohms to 100 kilohms have been provided for selection into the filter circuit. Since the response amplifier gain is 313, these values correspond to upper break frequencies of 0.031 Hz to 31 Hz in the system transfer function (see Equation [4.63]). At the higher resistance setting, the system can handle signal frequencies

down to 0.9 Hz with less than 2 degrees' phase distortion. At the lower resistance setting, the signal frequencies would have to be greater than 900 Hz, but all noise below 31 Hz would be attenuated. Wider ranges of operation can easily be achieved with other resistor and capacitor values.

It is especially significant to note that the input impedance of the virtual-ground amplifier is of the order of 10^{11} ohms so that the filter components are not at all loaded. The feedback filter is convenient for minimizing the system settling time following a change-over from one electrode-tissue system to another. Hence, during such changes, one uses the smallest resistor value in the filter.

The Current Control Circuit

For many applications, the resistance of a simple current source (Figure 3.6) would have to be impractically large, resulting in poor frequency response and excessive driving voltage requirements. The scheme which was chosen for the experimental system is capable of reducing these problems by several orders of magnitude. The basic configuration may be found in most applications manuals for analog computing amplifiers (e.g., Philbrick [1966]; Burr-Brown [1963]).

It is instructive to present the current control circuit in terms of the elementary principles involved. Consider the circuit shown in Figure 5.4. Let the q elements represent a simple current source and let the f elements designate a correction circuit applied as shown to the electrode-tissue system. It is desired to control I_f such that

$$I_Q = \frac{E_q}{R_q} \quad (5.2)$$

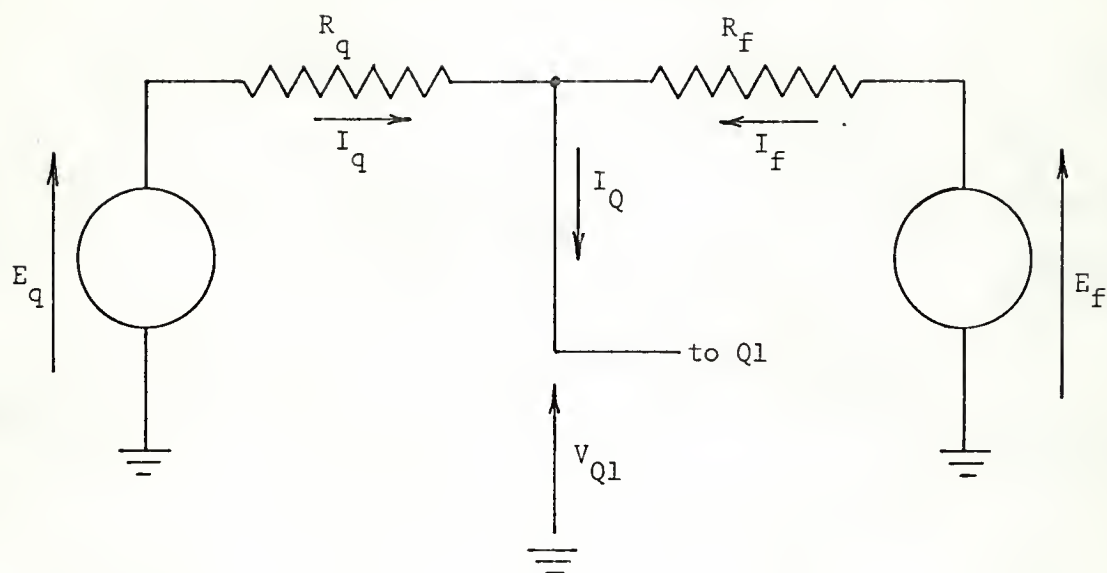


Figure 5.4. Principles of Current Control

which is independent of the impedance occurring at Q1. Since

$$I_q = \frac{E_q}{R_q} - \frac{V_{Q1}}{R_q} \quad (5.3)$$

it is evident that the required value of I_f is V_{Q1}/R_q . Noting that

$$I_f = \frac{E_f}{R_f} - \frac{V_{Q1}}{R_f} \quad (5.4)$$

the specification for the f generator may be written

$$\frac{E_f}{V_{Q1}} = 1 + \frac{R_f}{R_q} \quad (5.5)$$

The right side of Equation (5.5) is equal to the ideal transfer function of a common voltage follower (Figure A2) if

$$\frac{R_2}{R_1} = \frac{R_f}{R_q} \quad (5.6)$$

Hence the complete current control circuit may be drawn as in Figure 5.5.

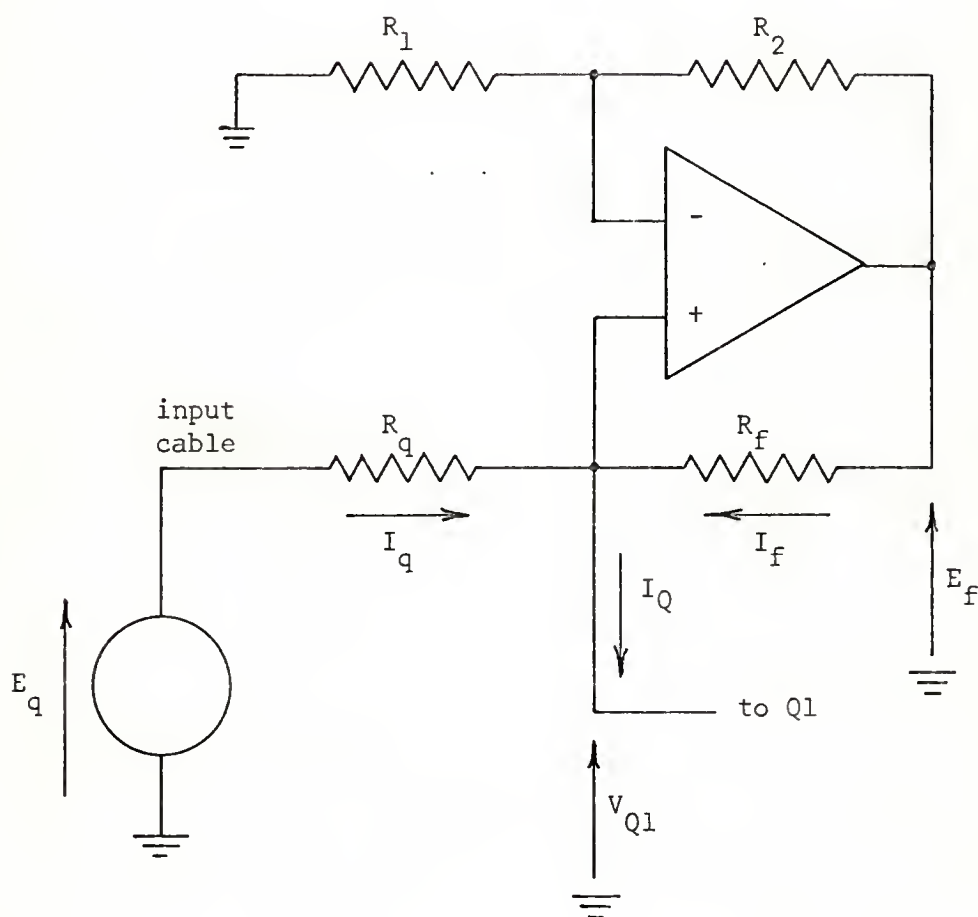


Figure 5.5. The Current Control Circuit

The exact output of the current control circuit may be written

$$I_Q = \frac{E_q}{R_q} (1 + \delta_Q) \quad (5.7)$$

The term, δ_Q , is the current control error and is analogous to α_Q and β_Q of Chapters 3 and 4. It is given by

$$\delta_Q = \beta_Q \left[\frac{K_f - 1}{R_f/R_q} - 1 \right] \quad (5.8)$$

where K_f is the exact transfer function of the voltage follower given by Equation A2.1. β_Q is the current control error that would result if E_q and R_q were used without the correction circuit and is defined by Equation (4.31). When the amplifier gain and common mode rejection ratio are sufficiently high (see Equations [A2.4] and [A2.5]), Equation (5.8) reduces to

$$\delta_Q \approx \beta_Q \left[\frac{R_2/R_1}{R_f/R_q} - 1 \right] \quad (5.9)$$

which goes to zero if Equation (5.6) is exactly satisfied.

As a practical illustration, assume that the difference term in Equation (5.9) is adjusted to 0.01. Then if, as in previous examples, the magnitude of the current control error (here $|\delta_Q|$) is limited to less than 0.01, the generator resistance requirement becomes

$$R_q > |Z_{Q1} + h_{31} + h_{11} + \beta_v h_{11}| \quad (5.10)$$

where use has been made of Equation (4.33). This condition is significantly less stringent than that for the simple current source in Equation (4.34). In many electrode-tissue systems, β_Q is significant only at very low frequencies where the interface impedance becomes large.

In such cases, the difference term in Equation (5.8) becomes unimportant at higher frequencies, and a low frequency amplifier may suffice in the current control circuit.

In the experimental system, R_1 and R_2 are 10 kilohms, and R_q and R_f are 1 megohm each. It is desirable not to make the ratio of R_2 to R_1 large to avoid reducing the dynamic range for current control. Since the amplifier used has an output voltage range of approximately ± 10 volts, the present circuit is capable of controlling up to ± 5 microamperes into a 1 megohm load at Q1. The current drawn by the input admittances of the amplifier must have negligible effect on circuit performance. This condition is virtually assured here since the impedance at either input is determined by a field effect transistor and corresponds to 10^{11} ohms in parallel with 5 picofarads.

In the actual system, R_q is on the circuit board and is connected to the voltage generator through several feet of coaxial cable. The shield of this cable is grounded at the generator. The current output of the control circuit is fed to the electrode-tissue system connector by one of the four miniature coaxial cables discussed earlier. The shield of this cable is tied to a voltage divider at the output of the current control amplifier in similar fashion as was done for the shield of the P1 cable in Figure 5.3.

Experimental Studies

The experimental virtual-ground system provides current control for the applied signal and amplification for the voltage response. Additional instruments are necessary to process and display the signals

for impedance determinations. In the experiments to be described, the input (E_q in Figure 5.4) and output (Figure 5.3) voltages of the system were continuously monitored on a dual-trace oscilloscope (see Figure 5.2). This display was convenient for observing approximate amplitude and phase relationships between the two signals and for ascertaining that the system was functioning properly.

Precise measurements were made with a model JB-6 Lock-in Amplifier from Princeton Applied Research Inc. (see Appendix 4 for principles of operation). When suitably calibrated, this instrument continuously displays, on separate meters, the relative in-phase and quadrature components of the system output with respect to the system input, or any other reference signal. The system input signal was derived from the internal generator of the JB-6. Aside from the convenience of a direct meter display, the lock-in amplifier permits measurements to be made in the presence of signal-to-noise ratios much below unity (Moore, 1962).

The experimental results are reported in two separate sections designated: Performance Tests and Four-Electrode Impedance Measurements. The measurement techniques used are incorporated in the block diagram of Figure 5.6. The components enclosed in the dashed block constitute the experimental virtual-ground system. Switch S_2 symbolically represents the double female connector and the male connectors described previously. Additional information about measurement techniques is given as needed in the discussions that follow.

Performance Tests

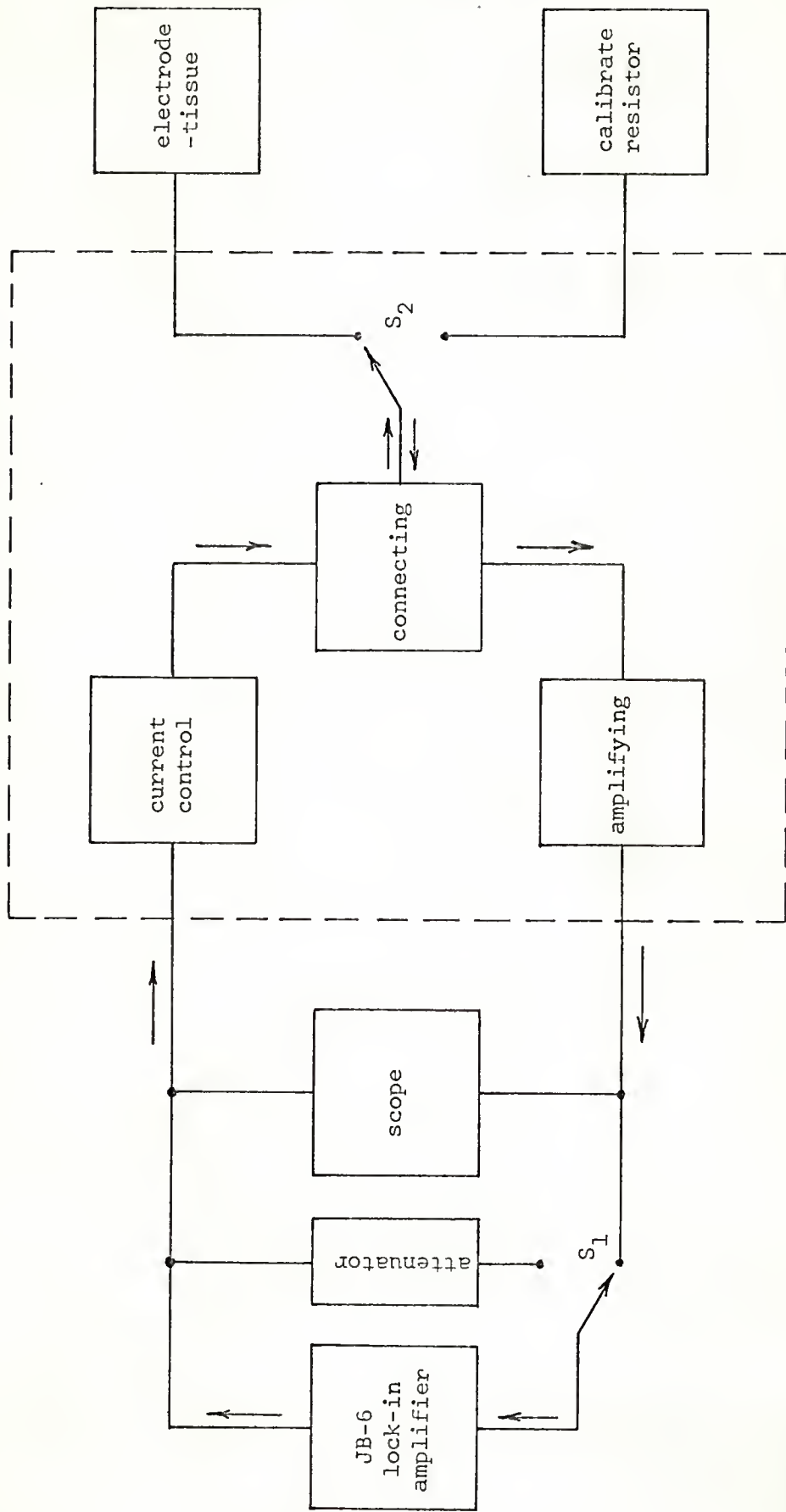


Figure 5.6. Block Diagram for Experimental Studies

The success of an impedance experiment depends on the overall performance of the combined electrode-tissue and instrumentation systems. The three experiments to be described are aimed at outlining the basic capabilities of the present virtual-ground system. Simple circuit arrangements are used to permit an independent evaluation of the frequency response, current control and common mode rejection characteristics of the system.

Frequency response test

The frequency response of the virtual-ground system is primarily of interest in cases where nonsinusoidal input waveforms are to be used. Hence, if a rectangular wave were applied to the current-control circuit and the electrode-tissue transfer impedance (m_{11}) were a pure resistance, the output waveform of the virtual-ground system should also be a rectangular wave, differing only in amplitude from the input signal. If the electrode-tissue transfer impedance includes reactive elements, then the output waveform should accurately represent the effects of these elements so that a spectral analysis can be made.

To measure the frequency response, a 1/4 watt carbon resistor of 10 or 100 ohms was used as the test subject in place of the electrode-tissue system. Since the resistor is a two terminal device, terminals Q1 and P1, and P2 and Q2, were coincident. This arrangement eliminated the possibility of current control and common mode rejection errors, which could have masked the true frequency response. The reference voltage for this test was derived from a simple resistive attenuator as shown in Figure 5.7. This circuit provides an adjustable frequency-independent fraction of the JB-6 output voltage.

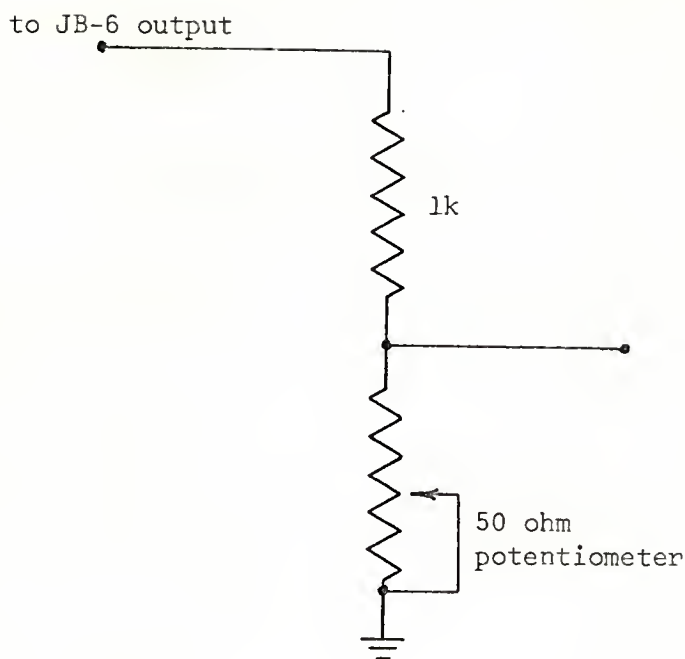


Figure 5.7. Attenuator Circuit for Frequency Response Test

The first step in the procedure was to adjust the attenuation ratio of the attenuator to equal the overall transfer function of the virtual-ground system and test resistor. This was done at an intermediate frequency (e.g., 100 Hz) where the transfer function was known to be real and constant. Then, the attenuator was maintained at this setting to provide the reference voltage at all other test frequencies. The procedure at each frequency was to calibrate the JB-6 using the attenuator output and then to switch over to the virtual-ground system. Magnitude and phase errors were detected as changes in the JB-6 meter readings from the calibration values.

At frequencies of 2 Hz, 10 Hz, 100 Hz, 1 kHz, and 10 kHz, no phase or magnitude errors could be detected. The results at higher

frequencies are indicated in Table 5.1. As a practical estimate, the maximum uncertainty in the tabulated results is approximately ± 1 percent for the magnitude errors and ± 1 degree for the phase errors. At frequencies of 10 kHz and below, the uncertainties in the zero errors observed are smaller.

TABLE 5.1

FREQUENCY RESPONSE ERRORS

Frequency Hz	Magnitude Error percent	Phase Error degrees
40 k	+1.4	0
70 k	0	-1.7
85 k	+1.3	0
100 k	+1.6	-1.8
150 k	+8.6	-3.3

The errors shown in Table 5.1 are probably within tolerable limits for most nonsinusoidal measurements in tissue at the present state of the art. However, it is reasonably certain that the frequency response could be improved using simple compensation techniques, should the occasion require it. One such technique was mentioned previously in the description of the response amplifier circuit.

Common mode rejection test

Common mode rejection capability is of interest because it establishes certain limits for the type of electrode configuration which

can be accurately measured with a given virtual-ground system. More specifically, it determines how large the impedance ratio of Equation (4.6) may become before $|\beta_v|$ exceeds an arbitrary maximum value. It is evident that common mode rejection capability is directly proportional to the gain of the virtual-ground amplifier.

To test the common mode rejection capability of the experimental system, the circuit shown in Figure 5.8 was used as the test subject in place of the electrode-tissue system. The calibrate resistance and

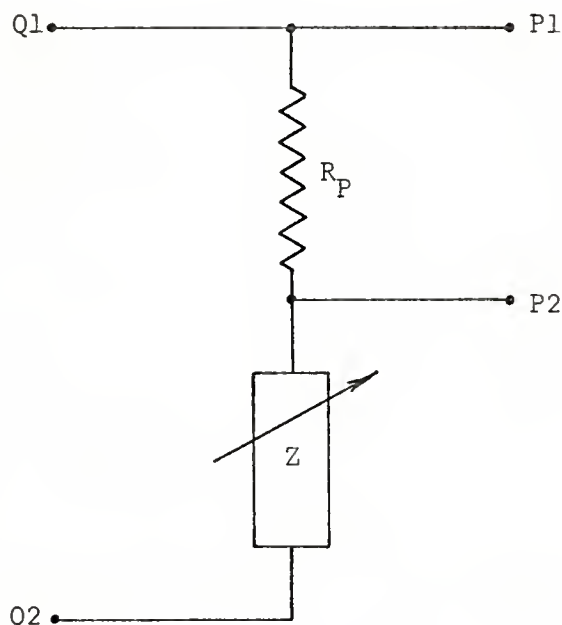


Figure 5.8. Circuit for Common Mode Rejection Test

the attenuator of Figure 5.6 were not used during this test. At each frequency of measurement, the procedure was to set Z equal to zero and calibrate the JB-6 against R_P . Then Z was increased in arbitrary steps until the magnitude or phase error due to excessive common mode signal

became large. The errors were detected as changes in the JB-6 meter readings from their calibration values. At very low frequencies, Z was derived from a decade capacitance box. At other frequencies, it was derived from a decade resistance box. This technique permitted phase shift to be used as the most sensitive indicator of error for all measurements.

The results of the common mode rejection test are summarized in Table 5.2. Notice that with each decade increase in frequency above 100 Hz, the value of $|Z|/R_p$, at which a similar phase error occurs, decreases by roughly one decade. At frequencies of 100 Hz and lower, the ratio corresponding to similar phase errors is much less dependent on frequency. Furthermore, it is evident that the phase angle was the predominant indicator of error at all frequencies, and that this was accomplished by making Z reactive at frequencies below 100 Hz and resistive at 100 Hz and above. The foregoing observations are in agreement with the nominal gain and phase shift characteristics given for the virtual-ground type of amplifier in Figure 4.2.

It is apparent that, at 100 kHz, the present system does not possess the capability expressed by Equation (4.8) if $|\beta_v|$ is required to be less than 0.01. The equation holds in the present case, however, if the limit for $|\beta_v|$ is taken as 0.04. In other words, the gain of the virtual-ground amplifier in the experimental system is approximately 250 at 100 kHz rather than the conjectured practical upper limit of 1000.

The frequency dependence of the common mode rejection capability of the virtual-ground system is especially appropriate for measurements in electrolytic (biological) media. Consider for example, the impedance

TABLE 5.2

COMMON MODE REJECTION ERRORS*

Frequency Hz	$ Z /R_p$	Magnitude Error percent	Phase Error degrees
2	2,700	0	0
	8,000	<0.2	-2.0
	16,000	<2	-4.7
10	1,600	0	0
	16,000	<0.5	-3.1
	32,000	<1	-7.4
100	1,600	0	0
	10,000	2.7	4.2
1k	100	0	0
	1,000	<0.5	3.1
10k	10	0	0
	100	<0.5	2.4
70k	1	0	0
	10	<0.5	1.4
100k	1	0	0
	5	<0.1	0.9
	10	<0.5	2.8
	20	<0.5	4.8

*Z is capacitive reactance at 2 Hz and 10 Hz, and resistance at all other frequencies. Results were obtained with R_p equal to 100 ohms. Similar results were obtained with R_p equal to 10 ohms.

ratio of Equation (4.7). At high frequencies, the interface impedance, Z_{Q2} , becomes small and the ratio approaches a constant value determined mainly by the geometry of the electrode system. As the frequency is decreased, the ratio increases and Z_{Q2} eventually becomes the dominant factor in the numerator. Since Z_{Q2} varies according to a fractional power of frequency (as noted in Chapter 1), it increases more slowly than K_V , which depends on the first power of frequency (see Figure 4.2). Therefore, if Equation (4.7) is satisfied at a given test frequency, it will almost certainly be satisfied (to an even greater extent) at frequencies below the test frequency. More precisely, since $|K_V|$ becomes constant at very low frequencies, the inequality will eventually become invalid at some frequency below the break in $|K_V|$.

When measuring an unknown electrode-tissue system, the foregoing considerations imply that it is sufficient to ascertain that V_{P2} is negligible compared to V_P (i.e., $|\beta_V|$ falls below an arbitrary limit) at the highest and lowest frequency in the measurement band. Then the common mode rejection error will also be negligible at all other frequencies in the band. In most cases, only the high frequency check is necessary.

Current control test

Current control capability determines how large the electrode-tissue impedance between the $Q1$ terminal and ground (given by the right side of Equation (5.10)) may become before the error in the applied current exceeds an arbitrary maximum value. It is primarily important at low frequencies where the interface impedance of the $Q1$ electrode

may become very large. Current control capability, per se, is fairly independent of frequency and is rarely a limiting factor at higher frequencies due to the predominance of loading and common mode rejection errors.

To test the current control capability of the experimental system, the circuit shown in Figure 5.9 was used as the test subject in place of the electrode-tissue system. The calibrate resistance and the

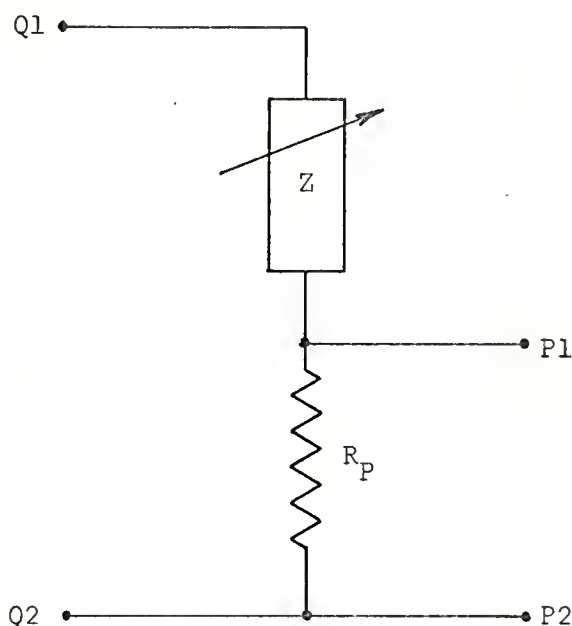


Figure 5.9. Circuit for Current Control Test

attenuator of Figure 5.6 were not used during this test. At each frequency of measurement, the procedure was to set Z equal to zero and calibrate the JB-6 against R_P. Then Z was increased in arbitrary steps until the magnitude or phase error became large as evidenced by changes in the JB-6 meter readings.

The results of the current control test are summarized in Table 5.3. Since R_q , in the present system, is 1 megohm, the results reported

TABLE 5.3

CURRENT CONTROL TEST RESULTS*

Frequency Hz	$ Z $ ohms	Magnitude Error percent	Phase Error degrees
10	16k	0	0
	160k	0	0
	1.6M	-1.8	2.1
	3.2M	-3.3	4.3
100k	500	0	0
	2.7k	<0.1	-1.9
	10k	1.6	-3.8

*Z is capacitive reactance at 10 Hz and resistance at 100 kHz. Results were obtained with R_p equal to 100 ohms.

for 10 Hz are in approximate agreement with the requirement expressed by Equation (5.10) for a current control error of less than 1 percent. The errors obtained at 100 kHz are not current control errors. They represent combined loading errors and have been included only for comparison.

Noise levels

Noise accompanying the signal output of the experimental virtual-ground system has been observed on the monitoring oscilloscope. Using a scope amplifier with a 3 db bandwidth of 500 kHz, the broadband peak-to-peak instrumentation noise has been between 20 and 40 microvolts

referred to the P1 terminal. The peak-to-peak noise due to sixty-cycle pick-up has consistently fallen within the range of the instrumentation noise. This low sixty-cycle level is obtained without the use of shielded enclosures, and in the presence of fluorescent lighting under ordinary laboratory conditions.

Four-Electrode Impedance Measurements

The measurements reported in this section were all made using a substitution technique suggested by Dr. Jack R. Smith. With reference to Figure 5.6, switch S_1 was maintained on the system output. The initial step at each frequency of interest was to calibrate the JB-6 for phase measurements with S_2 set on the calibrate resistor (the decade resistance box in Figure 5.2). This resulted in a zero reading on the quadrature meter and an arbitrary reading on the in-phase meter which was proportional to the resistance used. The resistance was generally chosen to approximate the anticipated value of the transfer impedance to be measured.

The next step was to set S_2 on the electrode-tissue (or other medium) system and record the quadrature and in-phase readings of the JB-6. The ratio of the quadrature to in-phase reading gave the tangent of the transfer impedance phase angle.

The final step was to switch S_2 back to the calibrate resistor and adjust the resistance until the in-phase reading was equal to that observed for the electrode-tissue system. This resistance was equal to the resistive part of the transfer impedance. Hence, knowing the phase angle and resistive part, the reactive part and the magnitude of the transfer impedance could be determined.

The substitution technique has the advantage that amplifier gain and frequency response characteristics need not be known precisely. In addition, it minimizes the chances for calibration errors since these will tend to be similar for both the calibration resistor and the unknown electrode-tissue system. The substitution technique, however, does not eliminate the effects of common mode rejection and current control error since the calibrate resistor is a two-terminal device and the electrode-tissue system is a four-terminal device. Therefore, these properties should be checked during experiment as previously described.

Electrode development

An important part of the current program has been to develop more reliable electrode systems, especially, for use in situ at very low frequencies. The problems stem mainly from transverse admittance in the electrode support materials (Chapter 3) and boundary condition effects at the electrode-electrolyte interfaces (Chapter 2), which occur independently of the instrumentation technique used. The virtual-ground system has made it possible to evaluate the performance of various electrode systems (in known test media) independently of errors which were previously introduced by less reliable instrumentation techniques.

One of the more recent electrode assemblies developed during the current program is illustrated in Figure 5.10. The square arrangement of the electrodes was designed by Dr. Arnold H. Nevis and is the outgrowth of a suggestion by the author to place the potential electrodes

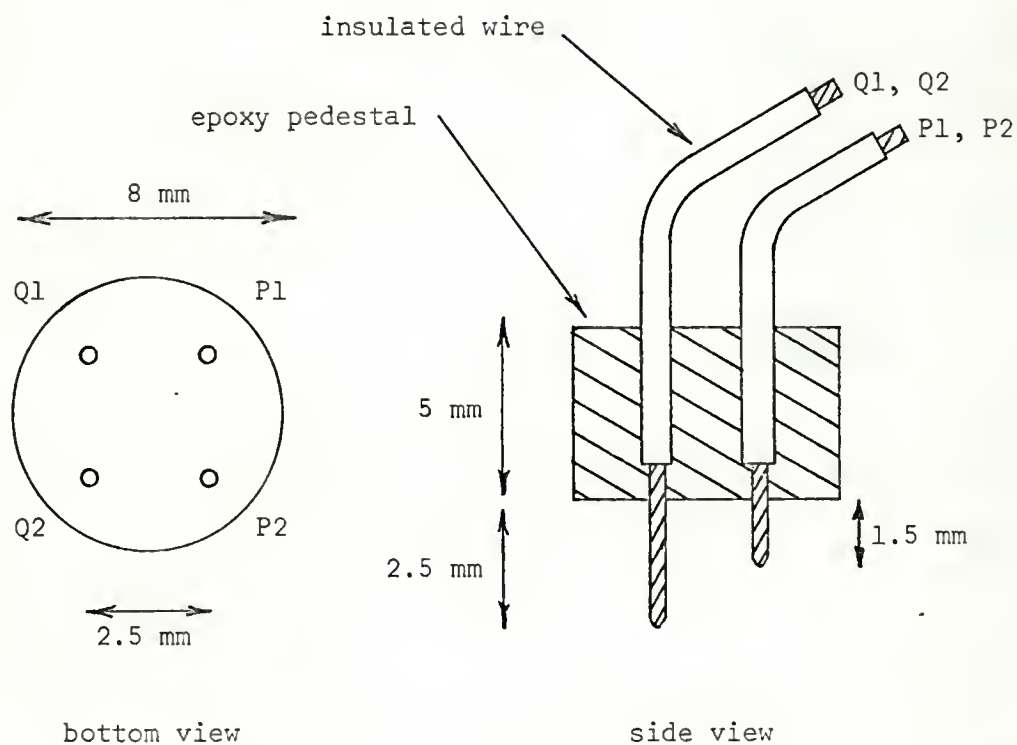


Figure 5.10. Electrode Assembly for In Situ Impedance Measurements

in a region of low potential gradient (see discussion of Equation [2.14] and Figure [2.3]). Stainless steel and platinum have been used for the electrode materials. In the latter case, the surfaces were platinized.

Experiments are in progress to evaluate the effects of insulating various portions of the electrode surfaces.

Each electrode is soldered to a flexible piece of insulated wire approximately one inch in length. The electrodes and wires are cast, as indicated, in a cylindrical epoxy pedestal. Connections to the wire ends are made by means of small covered alligator clips which are attached to the leads of the male connector of the virtual-ground system (see rat's head in Figures 5.1 and 5.2).¹ By bringing the exposed connections away from the electrode assembly, problems due to transverse admittance at very low frequencies have virtually been eliminated. Furthermore, the alligator clips are especially easy to apply to unrestrained animals.

A typical set of test results for an electrode assembly of the type indicated in Figure 5.10 using 0.18 mm diameter platinized platinum wires are given in Table 5.4. The transfer impedance (m_{11}) was found to be purely resistive and independent of frequency, except at 100 Hz where an anomalous 2.1 percent increase was observed. The source of this increase has not been determined. Additional and more carefully controlled electrode studies will be necessary before valid explanations can be given for the anomalous results which are sometimes observed. Sources of error may lie in human factors, in malfunctions of the JB-6 and in boundary condition effects in the electrode-saline system.

The fifth column in Table 5.4 indicates the ratio of common mode to differential signal of the electrode-saline system. The sixth

¹The epoxy pedestal and wire connection technique were developed by William K. Converse.

TABLE 5.4

TEST RESULTS OF AN ELECTRODE ASSEMBLY IN ISOTONIC SALINE

Freq Hz	m_{11} ohms	Magnitude Error percent	Phase Error degrees	$\frac{ V_2 }{ V_P }$	$ Z $ ohms
2	14.2	0	0	230	3,200
10	14.2	0	0	60	850
100	14.5	+2.1	0	--	---
1k	14.2	0	0	--	---
50k	14.2	0	0	--	---
100k	14.2	0	0	5.9	84

column indicates the effective impedance at the Q1 terminal which the current source must drive. It is apparent from the performance data in Tables 5.2 and 5.3 that the parameters of the electrode-saline system are well within the capabilities of the experimental virtual-ground system except at 100 kHz. At this frequency, the ratio of common mode to differential signal is in the range (greater than 5) where the common mode rejection errors start to become significant. This condition could be improved with more efficient placement of the potential electrodes (as indicated in Figure 2.3).

If the electrode assembly of Table 5.4 were used in tissue, the values in the $|Z|$ column would be greater than, while the values in the $|V_2|/|V_P|$ column would be similar to those in isotonic saline. Since the $|Z|$ column is well within system capabilities, the measurement of

tissue impedance would not be any more challenging to the virtual-ground system than the measurement of isotonic saline impedance.

Tissue impedance measurements

The experimental virtual-ground system has been used successfully to measure impedance in the cerebral cortex of rats and in the femur bone of rabbits. The cortical studies are part of a research program conducted by Doctors Arnold H. Nevis, Jack R. Smith, and George H. Collins. The bone measurements were part of a research project conducted by medical student Jim Mandel. These applications are especially noteworthy because they represent two widely different impedance levels, the bone impedance being roughly five times that of the cortex. Several of the cortical experiments are discussed in the following paragraphs to demonstrate the quality of results already obtained with the virtual-ground technique.

Electrode assemblies of the type shown in Figure 5.10 have been chronically implanted in the cerebral cortex of rats. The measurement techniques were described earlier in this section. The experimental arrangement is shown in Figures 5.1 and 5.2. The current density used at the current electrodes (area approximately 1.4 mm^2) was usually less than 1 microampere peak-to-peak/ mm^2 , and the response voltages were usually less than 100 microvolts peak-to-peak. In the experiments to be described, the electrodes were made of platinum wire (0.18 mm diameter) and were platinized.

The results plotted in Figure 5.11 characterize seven separate frequency runs measured in the same rat on seven different days during

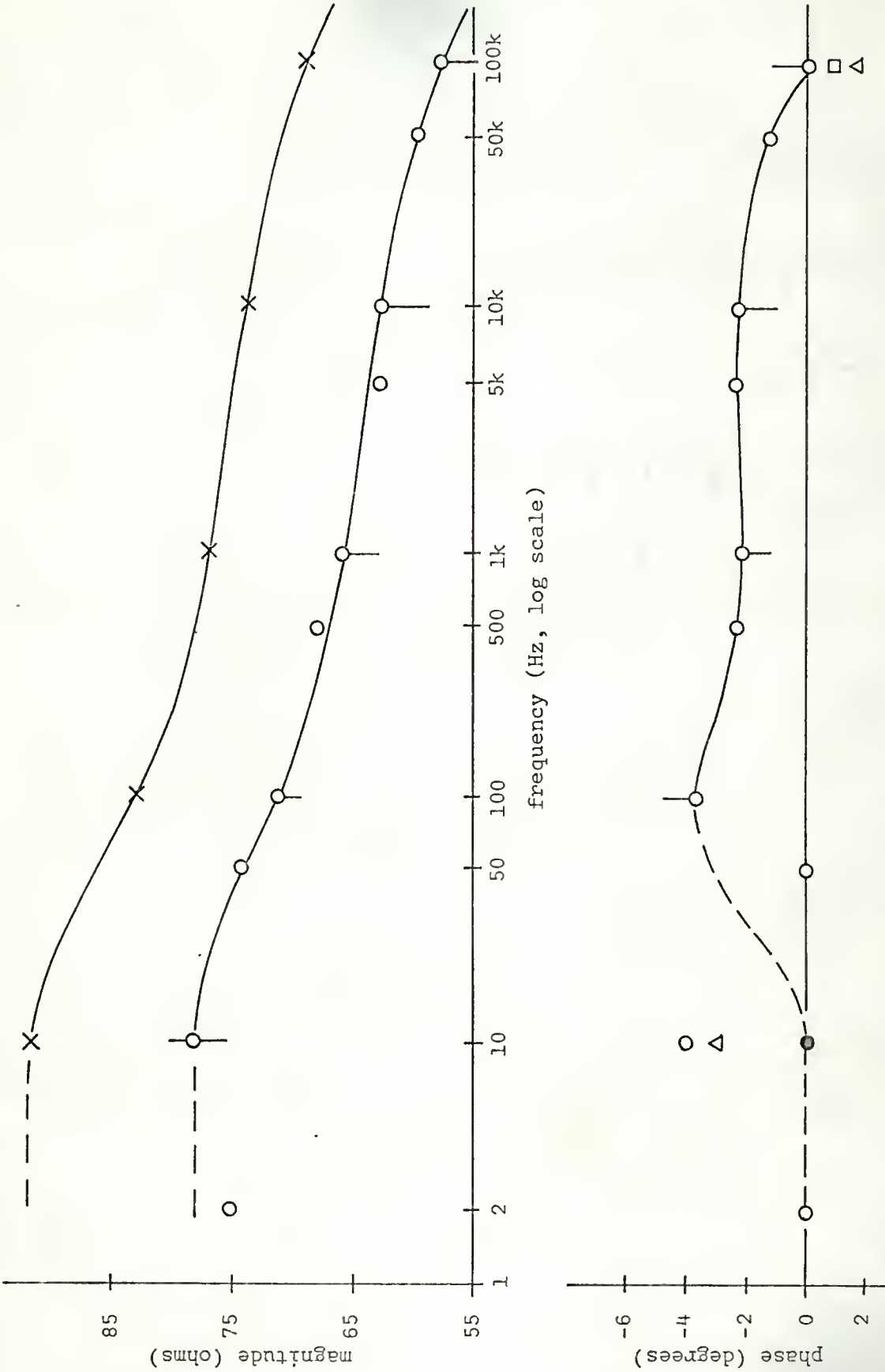


Figure 5.11. Impedance of Rat Cerebral Cortex In Situ

a 15-day interval. Only one of the frequency runs included a measurement at 2, 50, 500, 5k, and 50k Hz (shown by the small circles). The vertical lines at 10, 100, 1k, 10k, and 100k Hz indicate the spread of the majority of the seven experimental values obtained at each frequency. Individual values not within the lines are indicated by a symbol designating a particular frequency run (i.e., the cross, circle, triangle, and square).

The frequency run indicated by the crosses is a special case which was obtained after the other six runs and is discussed in a later paragraph. The six remaining spectra were measured within a thirteen-day interval. In the magnitude plot, the magnitude spread is 4 ohms or less, except at 10 Hz where it is 5 ohms. The largest percentage spread occurs at 100 kHz and is approximately 7 percent of the midsread impedance (which is about 57 ohms). In the original data, the individual magnitude changes at each frequency tended to be in the same direction so that the shape of the spectrum did not vary significantly. The total magnitude drop from 10 Hz to 100 kHz is approximately 20 ohms or 25 percent of the value at 10 Hz. The magnitude decrease at 2 Hz is contrary to previous experience and may be due to the increased uncertainty and difficulty of operating the JB-6 at very low frequencies in the presence of the electrocortigram.

In the phase plot, the phase spread is less than 1.5 degrees and all angles are zero or negative (capacitive), except at 100 kHz. The largest measured phase angle occurs at 100 Hz and lies between -3.6 and -4.8 degrees. The phase angles corresponding to the magnitude plot marked by the crosses consistently fell in the majority group for all

runs. At 10 Hz, five of the seven runs gave zero phase angle (and zero spread). The two anomalous points could conceivably be due to greater variability of the tissue impedance at 10 Hz. However, it is more probable that these points are due to errors in the procedure of operating the JB-6.

The positive phase angles at 100 kHz may be explained by the limited common mode rejection capability of the present virtual-ground system (see Table 5.2). The electrode system used had a common mode to differential signal ratio greater than 7 at 100 kHz. An experimental check of the voltage at P2 indicated a positive reactive component which could account for the anomalous phase angles. Errors of this type are influenced by the gain characteristics of the virtual-ground amplifier and certain other parameters which may vary from day to day.

It is apparent that more experimental points are necessary to fully evaluate the frequency spectrum, especially at the very low frequencies. Unfortunately, the very low frequency measurements are the most difficult to make due to the presence of strong electrocorticographic activity. They also involve lengthy calibration procedures because of the extended averaging time and large filter time constants which the JB-6 requires at these frequencies.

On each of the last nine days in the 15-day observation interval, the rat received an intraperitoneal injection of triethyl tin sulfate. This compound is known to be toxic and after a sufficient number of injections causes brain edema. The clinical symptoms include paralysis which begins in the hind limbs and continues to spread forward to the forelimbs and respiratory muscles until the animal dies.

The frequency run designated by the crosses was obtained two days after the last of the other six spectra were measured. The impedance rise was approximately correlated with the appearance of hind limb paralysis. As in the case of the day to day variations, the magnitude increase due to the injections was fairly uniform at all frequencies (approximately 11 ohms) and the shape of the spectrum was preserved. The phase angle values, as previously noted, were not affected by the injections.

It is interesting to note the magnitude of the specific impedance of the cortical tissue represented by the results in Figure 5.11. When tested in isotonic saline (approximately 60 ohm-cm. specific impedance), the electrode system indicated a transfer impedance of 12.5 ohms independent of frequency. The high and low frequency calculations for the specific impedance of the cortex are indicated in Table 5.5. The

TABLE 5.5

SPECIFIC IMPEDANCE OF RAT CEREBRAL CORTEX

Frequency Hz	Normal	Paralyzed
10	370	460
		ohm-cm
100k	280	330

normal values are not too different from those found by Ranck (1963a) in acute experiments on rabbit cortex.

The present data are insufficient to determine the exact location and the value of the maximum phase shift. However, it appears to be no greater than 5 degrees and to lie in the 50 to 100 Hz frequency range. Ranck (1963a) reported a maximum phase shift of 7 degrees which also occurred in the 50 to 100 Hz range in acute experiments on rabbit cortex. He also found that the phase angle went to zero at 5 kHz and increased again at frequencies above 20 kHz (a possible β dispersion). In the present case, the phase angle does not approach zero until frequencies beyond 50 kHz. Except for this order of magnitude difference in frequency of closure, the results found here in rat cortex in chronic experiments are in general agreement with the results found by Ranck in rabbit cortex in acute experiments.

In the complex impedance plane, the results of Figure 5.11 have the general form shown in Figure 5.12. The plot suggests that unlike

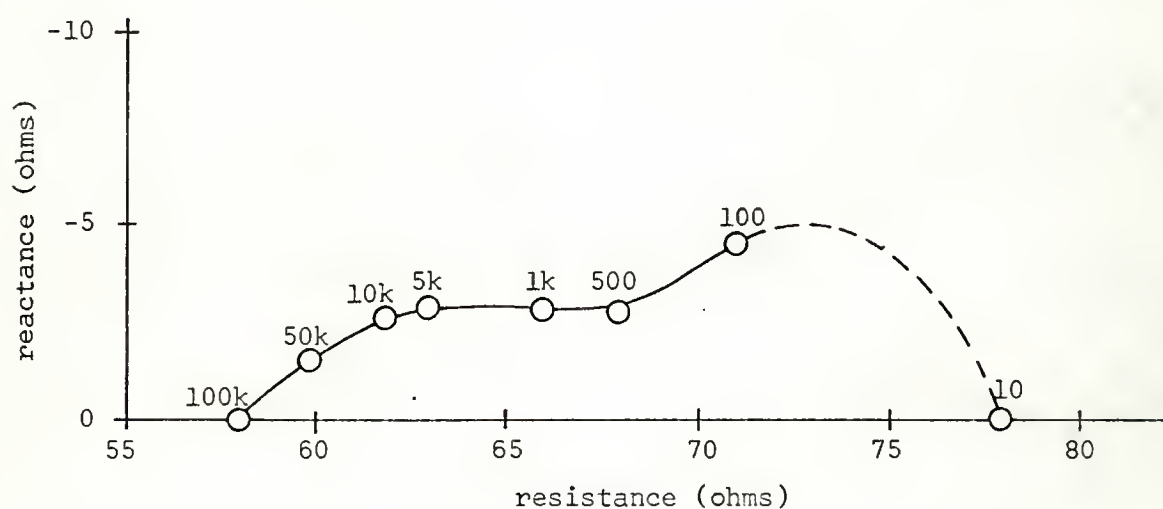


Figure 5.12. Polar Plot of the Impedance of Rat Cortex

that of muscle (Fatt, 1963), the impedance of cerebral cortex does not display distinctive circular arc behavior at frequencies below 100 kHz. Furthermore, it will be necessary to obtain measurements above 100 kHz in order to determine whether the β dispersion is distinct from the α dispersion.

The consistency and reproducibility of the results presented in Figure 5.11 demonstrate a clear advance in the field of in situ impedance measurements. The day to day magnitude spread (excluding the rise due to the injections) is well within bounds of normal physiological variations. For example, the author has monitored the impedance (at 1 kHz) of several normal rats who accidentally were not fed for one or two days. In a typical case, the impedance dropped from 94 to 85 ohms within the ten-minute interval after food was put in the cage. These results were correlated with visible symptoms of anxiety and oscillatory bursts in the electrocortigram.

The similarity of the seven impedance spectra implies that significant physiological variations did not occur during the frequency runs, even though it usually took from one-half to one hour to complete a run. Unfortunately, time invariance to this degree may not be possible in many important experiments to come. Hence, if spectral measurements are to be meaningful in such cases, it will be necessary to develop data-handling techniques with sufficient accuracy and speed to obtain "instantaneous" spectral information either on-line or from stored data. The virtual-ground system is one major link in the required instrumentation chain.

RECOMMENDATIONS FOR FUTURE STUDY

The foregoing work includes a body of general analytical results which express various aspects of the problem of four-electrode impedance measurements. It is hoped that many of these results will find application in the design and analysis of future electrode and instrumentation systems.

Potential developments in the field of biological impedance measurements appear to have practically unlimited scope. Topics suggested for immediate study are summarized in four groups below.

Electrode Systems

- a. Investigation of interfacial boundary effects in various electrode configurations using different electrode materials.
- b. Development of more definable current fields using guard electrode principles.
- c. Development of more appropriate media than saline for testing electrodes.

The Virtual-Ground System

- a. More precise compensation adjustments to flatten and extend frequency response.
- b. Connection for differential operation and/or the use of a wider band higher gain virtual-ground amplifier to extend common mode rejection capability.

- c. More precise adjustment of current control circuit to increase low frequency capability.
- d. More precise adjustment of +1 gain return to P1 cable to extend frequency response.
- e. Detailed evaluation and minimization of inherent loading admittances of the virtual-ground system and associated paraphernalia.
- f. Development of optimum filters for the feedback filter loop.
- g. Packaging of the virtual-ground system and feedback filter.

Information Retrieval

- a. Plotting of more points in the frequency spectrum, especially at very low and very high frequencies.
- b. Development of accurate techniques to store and/or process instantaneous spectral information.
- c. Development of optimum signal waveforms and sequences to maximize information retrieval in a given observation period.

Biological Studies

- a. Application of the principles presented in the foregoing work to studies of tissues in addition to brain and bone using suitably designed electrodes.
- b. Investigation of relationships between various physiological variables and tissue impedance properties.

APPENDICES

APPENDIX 1

RECIPROCITY RELATIONS OF THE IMPEDANCE PARAMETER MATRIX

The reciprocity relations of Equations (2.4), (2.5) and (2.6) may be derived with the aid of Figure A1. The currents at the terminals

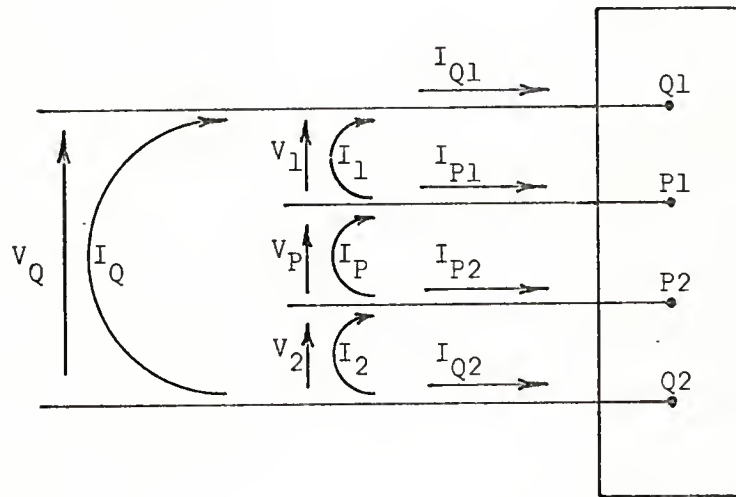


Figure A1. Voltage and Current Conventions for Reciprocity Relations of the electrode-tissue system are related to the loop currents as follows:

$$\begin{bmatrix} I_{Q1} \\ I_{P1} \\ I_{P2} \end{bmatrix} = \begin{bmatrix} (0 + I_Q + I_1) \\ (I_P + 0 - I_1) \\ (-I_P + 0 + 0) \end{bmatrix} \quad (A1.1)$$

If Equation (A1.1) is substituted into Equation (2.3), the result may be expanded and arranged in the following form:

$$\begin{bmatrix} V_P \\ V_Q \\ V_L \end{bmatrix} = \begin{bmatrix} m_{12} + m_{13} & m_{11} & m_{11} - m_{12} \\ m_{22} - m_{23} & m_{21} & m_{21} - m_{22} \\ -m_{32} + m_{33} & m_{31} & m_{31} + m_{32} \end{bmatrix} \begin{bmatrix} I_P \\ I_Q \\ I_L \end{bmatrix} \quad (\text{A1.2})$$

This type of matrix, which relates terminal voltages to loop currents, is a common form in network theory and is known to be symmetrical in a system obeying reciprocity.

Hence, setting the corresponding elements on either side of the diagonal equal yields

$$m_{22} = m_{23} + m_{11} \quad (\text{A1.3})$$

$$m_{32} = m_{12} + m_{33} - m_{11} \quad (\text{A1.4})$$

$$m_{21} = m_{31} + m_{22} \quad (\text{A1.5})$$

These expressions correspond in order to Equations (2.4), (2.5) and (2.6), if m_{22} is eliminated in Equation (A1.5) by means of Equation (A1.3).

APPENDIX 2

THE VOLTAGE FOLLOWER AMPLIFIER

The configuration of a common voltage follower amplifier is shown in Figure A2. The exact transfer function of this circuit may

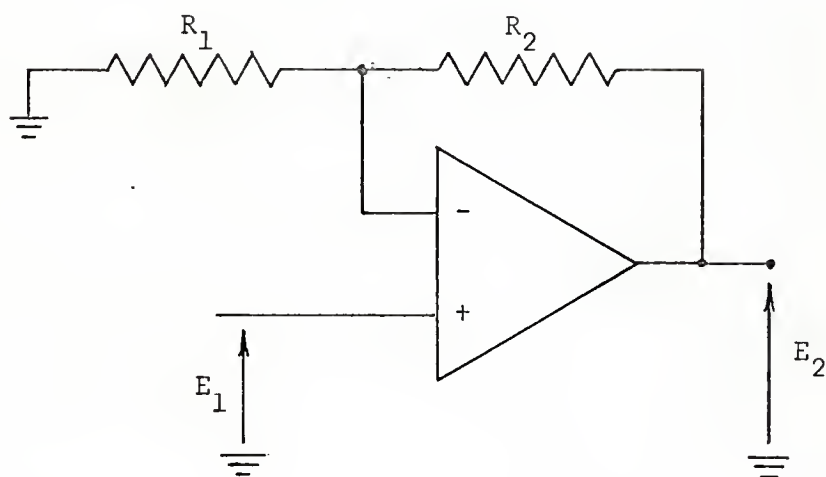


Figure A2. Voltage Follower Amplifier

be written

$$K_f \equiv \frac{E_2}{E_1} = \frac{(1 + 1/\rho)(1 + R_2/R_1)}{1 + \frac{1 + R_2/R_1}{K'}} \quad (\text{A2.1})$$

where ρ is the common mode rejection ratio and K' is the loaded open-loop gain of the operational amplifier. If Z' designates the total effective load at the output, then

$$K' = \frac{K}{1 + Z_o/Z'} \quad (A2.2)$$

where K is the open-loop unloaded gain and Z_o is the output impedance of the operational amplifier.

Ideally, ρ and K' are infinite and the transfer function is given by

$$K_f = 1 + R_2/R_1 \quad (A2.3)$$

which is independent of amplifier characteristics. To approach this ideal with an error of less than 1 percent, the following conditions are sufficient

$$|\rho| > 100 \quad (A2.4)$$

$$|K| > 100(1 + R_2/R_1)|1 + Z_o/Z'| \quad (A2.5)$$

APPENDIX 3

THE VOLTAGE INVERTER AMPLIFIER

The configuration of a common voltage inverter amplifier is shown in Figure A3. The exact transfer function of this circuit may be

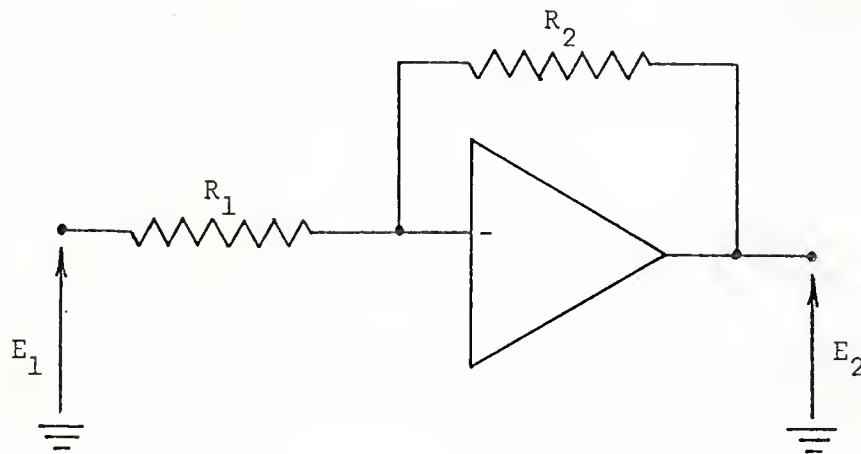


Figure A3. Voltage Inverter Amplifier

written

$$K_i \equiv \frac{E_2}{E_1} = \frac{-R_2/R_1}{1 + \frac{1 + R_2/R_1}{K'}} \quad (\text{A3.1})$$

where K' is as defined in Equation (A2.2).

APPENDIX 4

PRINCIPLES OF THE LOCK-IN AMPLIFIER

The main components of the lock-in amplifier are indicated in Figure A4. The signal of the tuned oscillator is applied to the variable phase shifter and via the reference channel output to the test system of interest. The output of the test system is fed via the signal channel input to the tuned amplifier.

The tuned amplifier filters out a significant part of the noise which may accompany the test signal. It also amplifies the signal and shifts it 90 degrees to provide an output in quadrature and an output in phase with the signal voltage.

The in-phase and quadrature signals are applied to the detection systems where they are multiplied by the output signal of the phase shifter and averaged to give the d.c. voltages, E_I and E_Q , as indicated. The detection systems comprise a phase sensitive detector followed by a d.c. amplifier-low pass filter combination, which provide additional noise rejection.

The usefulness of the lock-in amplifier is contained in its d.c. output voltages E_I and E_Q which may be conveniently displayed on separate meters. Hence, the amplitudes of E_I and E_Q are directly proportional to the signal amplitude while the phase of the signal with respect to the shifted reference signal is

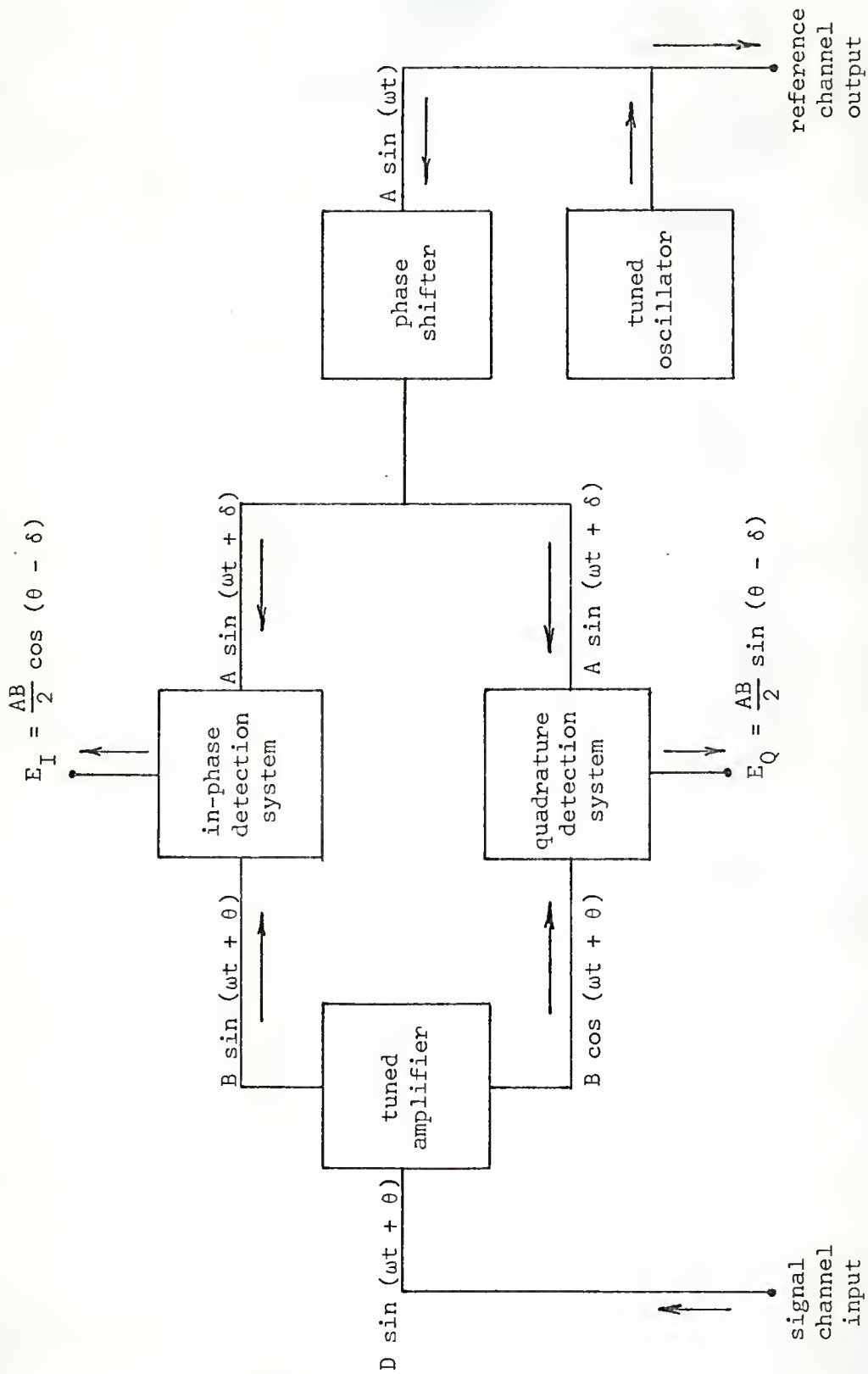


Figure A4. Block Diagram of the Lock-in Amplifier

$$\theta - \delta = \tan^{-1} \frac{E_Q}{E_I} \quad (A4.1)$$

To illustrate how the lock-in amplifier may be used, let a known resistive network be connected between the reference and signal channels. In this case, θ is zero and if the phase shifter is adjusted until E_Q is zero, δ will also be zero. If now, the resistive network is replaced by an unknown system, Equation (A4.1) would give the phase shift of the system transfer impedance. To find the magnitude of the transfer impedance, the resistive network would be reconnected and adjusted to give the same E_I as the unknown system. The value of the resistive network is then the resistive part of the transfer impedance which with the phase determines the magnitude and reactive part.

The foregoing procedure may also be used when δ is not known provided that it occurs as a common error factor in the calibrate system and in the unknown system. This assumption is the basis for the substitution method used in the transfer impedance measurements of Chapter 5.

REFERENCES

- Adey, W. R., Kado, R. T. and Didio, J. (1962) Impedance measurements in brain tissue of animals using microvolt signals. Exptl. Neurol., 5, 47-66.
- Aladjalova, N. A. (1964) Ionic processes in the cerebral cortex investigated by the method of conductivity. In Progress in Brain Research, 7, Ch VIII, 156-206.
- Benjamin, J. M., Jr., Schwan, H., Kay, C. F. and Hafkenschiel, J. H. (1950) The electrical conductivity of living tissue as it pertains to electrocardiography part I. Circulation, 2, 321-335.
- Bode, H. W. (1945) Network Analysis and Feedback Amplifier Design, D. Van Nostrand Co., Inc.
- Burger, H. C. and van Dongen, R. (1960-61) Specific electric resistance of body tissues. Physics Med. Biol., 5, 431-447.
- Burger, H. C. and van Milaan, J. B. (1943) Measurements of the specific resistance of the human body to direct current. Acta Medica Scand., 114, 584-607.
- Burr-Brown Research Corporation (1963) Handbook of Operational Amplifiers Applications.
- Cole, K. S. (1949) Dynamic electrical characteristics of the squid axon membrane. Arch. Sci. Physiol., 3, 253-258.
- Cole, K. S. (1955) Ions, potentials, and the nerve impulse. In Electrochemistry in Biology and Medicine, ed. T. Shedlovsky, Wiley, 133-135.
- Cole, K. S. (1962) The advance of electrical models for cells and axons. Biophys. J., 2, No. 2 Part 2, 101-119.
- Cole, K. S. and Curtis, H. J. (1937) Wheatstone bridge and electrolytic resistor for impedance measurements over a wide frequency range. Rev. Sci. Inst., 8, 333-339.
- Combs, J. S., Curtis, D. R. and Eccles, J. C. (1959) The electrical constants of the motoneurone membrane. J. Physiol. (London), 145, 505-528.

- Combs, J. S., Eccles, J. C. and Fatt, P. (1955) The electrical properties of the motoneurone membrane. J. Physiol. (London), 130, 291-325.
- Dern, H. and Walsh, J. B. (1963) Analysis of complex waveforms. In Physical Techniques in Biological Research, VI, Ch. 3, 109.
- Fatt, P. (1963) An analysis of the transverse electrical impedance of striated muscle. Proc. Roy. Soc., B. 159, 606-651.
- Fessard, A. and Tauc, L. (1956) Capacité, résistance et variations actives d'impédance d'un soma neuronique. J. Physiol. (Paris), 48, 541-544.
- Flasterstein, A. H. (1966a) Voltage fluctuations of metal-electrolyte interfaces in electrophysiology. Med. Biol. Engng., 4, 583-588.
- Flasterstein, A. H. (1966b) A general analysis of voltage fluctuations of metal-electrolyte interfaces. Med. Biol. Engng., 4, 589-594.
- Freygang, W. H. and Landau, W. M. (1955) Some relations between resistivity and electrical activity in the cerebral cortex of the cat. J. Cell. Comp. Physiol., 45, 377-392.
- Fricke, H. (1932) The theory of electrolytic polarization. Phil. Mag., 14, 310-318.
- Fricke, H. and Curtis, H. J. (1937) The dielectric properties of water-dielectric interphases. J. Phys. Chem., 41, 729-745.
- Fricke, H. and Morse, A. (1925) The electric resistance and capacity of blood for frequencies between 800 and 4 1/2 million cycles. J. Gen. Physiol., 9, 153-167.
- Geddes, L. A. and Baker, L. E. (1967) The specific resistance of biological material--a compendium of data for the biomedical engineer and physiologist. Med. Biol. Engng., 5, 271-293.
- Graham, M. (1965a) EEG preamplifier. IEEE Tr. Bio-Med. Engng., BME 12, 191-193.
- Graham, M. (1965b) Guard ring use in physiological measurements. IEEE Tr. Bio-Med. Engng., BME 12, 197-198.
- Ham, A. W. (1965) Histology, 5th ed., Lippincott Co., 165-166.
- Hodgkin, A. L., Huxley, A. F. and Katz, B. (1952) Measurement of current-voltage relations in the membrane of the giant axon of loligo. J. Gen. Physiol., 116, 424-448.

- Marmont, G. (1949) Studies on the axon membrane. J. Cell. Comp. Physiol., 34, 351-382.
- Moore, J. W. and Cole, K. S. (1963) Voltage clamp techniques. In Physical Techniques in Biological Research, VI, 263-321.
- Moore, R. D. (1962) Lock-in amplifiers for signals buried in noise. Electronics, June 8, 40-43.
- Nevis, A. H. and Collins, G. H. (1967) Electrical impedance and volume changes in brain during preparation for electron microscopy. Brain Research, 5, 57-85.
- Nicholson, P. W. (1965) Specific impedance of cerebral white matter. Exptl. Neurol., 13, 386-401.
- Philbrick Researches, Inc. (1966) Applications Manual for Computing Amplifiers for Modelling, Measuring, Manipulating, and Much Else.
- Raisbeck, G. (1954) A definition of passive linear networks in terms of time and energy. J. App. Phys., 25, 1510-1514.
- Rall, W. (1959) Branching dendritic trees and motoneuron membrane resistivity. Exptl. Neurol., 1, 491-527.
- Ranck, J. B., Jr. (1963a) Specific impedance of rabbit cerebral cortex. Exptl. Neurol., 7, 144-152.
- Ranck, J. B., Jr. (1963b) Analysis of specific impedance of rabbit cerebral cortex. Exptl. Neurol., 7, 153-174.
- Ranck, J. B., Jr. (1964) Specific impedance of cerebral cortex during spreading depression, and an analysis of neuronal, neuroglial, and interstitial contributions. Exptl. Neurol., 9, 1-16.
- Ranck, J. B., Jr. (1966) Electrical impedance in the subicular area of rats during paradoxical sleep. Exptl. Neurol., 16, 416-437.
- Ranck, J. B., Jr. and Be Ment, S. L. (1965) The specific impedance of the dorsal columns of cat: an anisotropic medium. Exptl. Neurol., 11, 451-463.
- Rush, S. Abildskov, J. A. and McFee, R. (1963) Resistivity of body tissues at low frequencies. Circulation Res., 12, 40-50.
- Schmitt, O. H. (1955) Dynamic negative admittance components in statically stable membranes. In Electrochemistry in Biology and Medicine, ed. T. Shedlovsky, Wiley, 91-120.
- Schwan, H. P. (1954) Electrical properties of muscle tissue at low frequency. Ztschr. Naturforschung, 9b, 245-251.

- Schwan, H. P. (1957) Electrical properties of tissue and cell suspensions. In Advances in Biological and Medical Physics, V, 147-209.
- Schwan, H. P. (1959) Alternating current spectroscopy of biological substances. Proc. IRE, 47, 1841-1855.
- Schwan, H. P. (1963) Determination of biological impedances. In Physical Techniques in Biological Research, VI, 323-407.
- Schwan, H. P. and Cole, K. S. (1960) Bioelectricity: alternating current admittance of cells and tissues. In Medical Physics, ed. O. Glasser, III, 52-56.
- Schwan, H. P. and Kay, C. F. (1956) Specific resistance of body tissues. Circulation Res., 4, 664-670.
- Schwan, H. P. and Kay, C. F. (1957) Capacitive properties of body tissues. Circulation Res., 5, 439-443.
- Schwan, H. P. and Sittel, K. (1953) Wheatstone bridge for admittance determinations of highly conducting materials at low frequencies. Tr. Am. Inst. Elec. Eng., 72, 114-121.
- Shalit, M. N. and Mahler, Y. (1966) Brain impedance measurements by the use of small bipolar needle electrodes. J. Appl. Physiol., 21, 1237-1242.
- Shedlovsky, T. (1930a) A screened bridge for the measurement of electrolytic conductance I. Theory of capacity errors II. Description of the bridge. J. Am. Chem. Soc., 52, 1793-1805.
- Shedlovsky, T. (1930b) A conductivity cell for eliminating electrode effects in measurements of electrolytic conductance. J. Am. Chem. Soc., 52, 1806-1811.
- Smith, J. R. (1967) Brain impedance spectroscopy under dynamic conditions. Digest of the 7th International Conf. on Medical and Biological Engng., 127.
- Smith, J. R., Nevis, A. H. and Collins, G. H. (1967) Polarization impedance of stainless steel bipolar electrodes in brain. Exptl. Neurol., 18, 287-299.
- Songster, G. F. (1967) A four-electrode bridge for biological-impedance measurements. Proc. Annual Conf. Engng. Medicine and Biol. 9, 13.5.
- Van Harreveld, A. (1966) Brain Tissue Electrolytes, Butterworth.

Van Harreveld, A., Murphy, T. and Nobel, K. W. (1963) Specific impedance of rabbit's cortical tissue. Am. J. Physiol., 205, 203-207.

Van Valkenburg, M. E. (1955) Network Analysis, Prentice Hall.

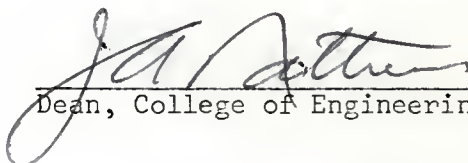
BIOGRAPHICAL SKETCH

Allen Harris Flasterstein was born January 5, 1937, in Long Island, New York. In June, 1954, he was graduated from Abraham Lincoln High School in Brooklyn, New York. In February, 1959, he received the degree of Bachelor of Electrical Engineering from The City College of New York. From February, 1959, through August, 1962, he was a member of the technical staff of RCA Laboratories at Princeton, New Jersey. In June, 1961, he received the degree of Master of Science in Engineering with a major in Electrical Engineering from Princeton University.

Since September, 1962, Allen Harris Flasterstein has been engaged in an original program of coursework and research at the University of Florida leading to the degree of Doctor of Philosophy with a major in Electrical Engineering and a minor in the biomedical sciences. He has been an NIH Predoctoral Fellow since September, 1964, and is a member of Sigma Xi, Phi Kappa Phi, and Eta Kappa Nu.

This dissertation was prepared under the direction of the chairman of the candidate's supervisory committee and has been approved by all members of that committee. It was submitted to the Dean of the College of Engineering and to the Graduate Council, and was approved as partial fulfillment of the requirements for the degree of Doctor of Philosophy.

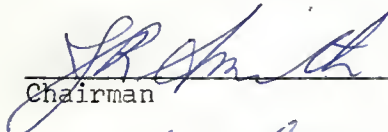
August, 1968



Dean, College of Engineering

Dean, Graduate School

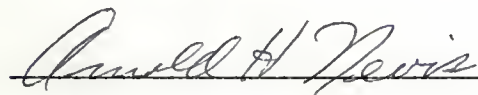
Supervisory Committee:



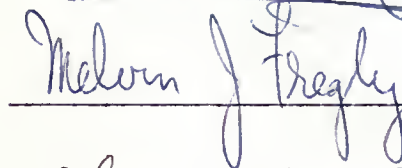
Chairman

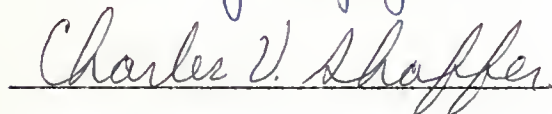


Co-Chairman











UNIVERSITY OF FLORIDA



3 1262 08554 5928